MODELING THE CHEMISTRY OF PLANETARY ATMOSPHERES: IMPLICATIONS FOR THE BULK COMPOSITIONS OF GIANT PLANETS

A Dissertation

Presented to the Faculty of the Graduate School

of Cornell University

in Partial Fulfillment of the Requirements for the Degree of

Doctor of Philosophy

by

Dong Wang

May 2017

MODELING THE CHEMISTRY OF PLANETARY ATMOSPHERES:
IMPLICATIONS FOR THE BULK COMPOSITIONS OF GIANT PLANETS

Dong Wang, Ph.D.
Cornell University 2017

The oxygen abundances of giant planets potentially constrain the conditions of the protoplanetary disk and formation models of planetary systems. In our solar system, the abundances of water, the primary carrier of oxygen in the atmospheres of giant planets, are still unknown for all four giant planets. Juno spacecraft, currently orbiting Jupiter, has the objective of constraining Jupiter's deep water abundance (at a few bars to a hundred bars level) through microwave radiometery. A Saturn entry probe is proposed as a candidate for the New Frontiers program, with the goal of making in-situ measurements of Saturn's atmospheric composition. However, it is not likely to reach deeply enough to directly measure the deep water abundance. There are no planned missions for the atmospheres of Uranus and Neptune. Disequilibrium species have long been used to constrain the deep water abundances for Jupiter and Saturn. In this dissertation, we aim to improve the chemical constraints on the deep water abundances. For Jupiter, we improved the chemical constraints on the deep water abundance by CO. We proposed a new formulation for the deep eddy diffusion coefficient by analyzing the experimental studies of turbulent rotating convection. We considered two updated CO kinetic models, one model constrains the water enrichment (relative to solar) to be between 0.1 and 0.75, while the other constrains the water enrichment to be between 3 and 11. Our study quantitatively accounted for the uncertainties on the constraints due to

different reaction rates. We also predicted that the abundances of disequilibrium species should have latitudinal variation due to the latitudinal dependence of the eddy diffusion coefficient. Such variations have been confirmed by VLA measurements [Giles et al., 2017], however, the measured dependences are different from our predictions, which merits further investigations. For Saturn, we proposed an approach to break the degeneracy between the deep water abundance and the deep eddy diffusion coefficient when interpreting the CO observations. We identified another disequilibrium species, C_2H_6, whose abundance only depends on the deep eddy diffusion coefficient, but not the deep water abundance. A shallow entry probe may have the ability to determine both the CO abundance and the C_2H_6 abundances through a mass spectrometer, therefore, constraining the deep water abundance and eddy diffusion coefficient simultaneously.

The transit spectroscopy provided an opportunity for constraining the composition of extrasolar giant planets. JWST should be able to collect the highest quality transit spectra in the future. For extrasolar giant planet atmospheres we expect to measure and retrieve the abundance of the most abundant molecules, such as H_2O, CO, and CH_4. Other molecules, such as H_2S and PH_3, have been observed in Jupiter and Saturn but their chemistry and detectability in strongly irradiated planets is highly unknown. Can JWST detect them? Are they important in the chemistry for these exoplanets atmospheres? To address these questions, we model the chemistry of phosphorus and sulfur in hydrogen-rich atmospheres including the effect of vertical transport. Using the abundance profiles computed for major C/N/O/S/P bearing species, we model the JWST primary and secondary transit spectra for systems with a Sun-like star at a distance of 50 pc and with different levels of insolation. We find PH_3 is detectable

in the transmission spectra for planets with $T_{\rm eq} < 500$ K using the NIRCam instrument with LW grism mode and F444W filter, and the H_2S is detectable in the transmission and emission spectra for planets with $T_{\rm eq} > 1500$ K using the NIRCam instrument with LW grism and F322W2 filter. Our results specially highlight the importance of including H_2S for future abundances retrieval with JWST.

BIOGRAPHICAL SKETCH

Dong Wang was born in Ningyang, a small town in the eastern part of China. He spent the first eighteen years living and studying in Ningyang. In 2007, he went to Beijing to study astronomy at Peking University. In 2011, he went to the US for the first time, to pursue a Ph.D. in astronomy at Cornell University. After six years graduate school life in Ithaca, he completed this dissertation. He will then move to New York City to start a new chapter of life.

This dissertation is dedicated to my parents, who gave me a mind to explore the universe.

ACKNOWLEDGEMENTS

I would like to thank my advisor, Jonathan Lunine. Jonathan helped me and influenced me in many ways. The first two years at Cornell was difficult, due to the cultural difference between China and US, and the transition from classwork to research. While I was quite good at course work and working out a well-defined problem, I had some difficulty tangling research problems, which may not have definitive answers. Jonathan was very patient and always encouraged me in the group meeting. With Jonathan's help, I slowly made progress on my research projects and published my first paper by the end of the third year. Jonathan introduced several excellent researchers to me, who became my collaborators later, and helped me a lot in developing this dissertation. Jonathan was also very fast in responding my emails, despite his tightly-packed schedule. During my Ph.D., I can feel Jonathan is standing by me, and ready to help me and support me. I am lucky to have Jonathan as my advisor.

I also would like to thank my collaborators, Peter Gierasch, Olivier Mousis, and Yamila Miguel. They all helped me a lot in my research. Peter pointed the right direction in my research on the eddy diffusivities of Jupiter. Olivier suggested the chemical softwares and chemical models that are the important tools for developing this dissertation. Yamila encouraged to me develop an idea that finally resulted in my third paper. They all have set up a good model for me in conducting research.

I would also like to thank many professors at Cornell who helped me in my research and classes. I would like to thank Olivier Desjardins, who introduced the software *cantera* to me, which is a very useful tool in my research. I would like to thank professors in my department who taught me classes, and helped me get into the filed of astronomy, including Gordon Stacey, Dong Lai, and so

on. I would like to thank Andrew Wilson, whose class triggered my interest in computer science.

I would like to thank my peers and colleagues in planetary science, especially Li Cheng and Zhang Xi from Caltech, Hu Renyu from JPL. It was quite a happy experience to discuss planetary science with them in Tucson and San Francisco.

I would like to thank my classmates, especially my office mate Tyler Pauly, for studying together, and keeping me motivated. I also would like to thank Monica Armstrong, who is enthusiastic to reply any questions I have about graduate life.

Last but not least, I would like to thank my parents, for supporting me and trusting me in my decisions. It was not easy to let their only son to study abroad. I would like to thank my girlfriend Summer Zhang, who is my closest person in the United States.

TABLE OF CONTENTS

Biographical Sketch . . . iii
Dedication . . . iv
Acknowledgements . . . v
Table of Contents . . . vii
List of Tables . . . ix
List of Figures . . . x

1 Introduction 1

2 One dimensional chemical models for planetary atmospheres 6
2.1 Introduction . . . 6
2.2 Equilibrium model . . . 7
2.3 Diffusion kinetics model . . . 8
2.3.1 Introduction of the diffusion kinetic code . . . 8
2.3.2 Validation of the diffusion kinetic code . . . 13
2.4 Timescale model . . . 16

3 New insights on Jupiter's deep water abundance from tropospheric carbon monoxide abundances 18
3.1 Introduction . . . 18
3.2 A New Formulation for the Deep Eddy Diffusion Coefficient . . . 20
3.2.1 Theory on Eddy Diffusion Coefficient . . . 21
3.2.2 Scalings from Rotating Tank Experiments . . . 23
3.2.3 Eddy Diffusion Coefficient in the Atmosphere of Jupiter and Saturn . . . 29
3.3 Deep Water Abundance Constrained by CO Thermochemistry Kinetics . . . 35
3.3.1 Constraints Using the Rate Limiting Step from Visscher and Moses [2011] . . . 36
3.3.2 Constraints Using Kinetic Model from Venot et al. [2012] . . . 42
3.4 Discussion . . . 47
3.5 Conclusion . . . 55

4 Modeling disequilibrium species for Jupiter and Saturn: implications for Juno and Saturn entry probe 57
4.1 Introduction . . . 57
4.2 Measurements of disequilibrium species: current status . . . 59
4.3 Model . . . 60
4.3.1 Introduction to the model . . . 60
4.4 Results . . . 62
4.4.1 Simulation results using the C/N/O/H reaction network 63
4.4.2 Simulation results using the H/P/O reaction network . . 67

4.4.3 Simulation results for SiH4 . . . 72
4.4.4 Simulation results for GeH4 . . . 77
4.4.5 Simulation results for AsH3 . . . 81
4.5 Discussion . . . 86
4.5.1 Further constraints by Juno . . . 86
4.5.2 Application to a Saturn entry probe . . . 88
4.5.3 Uncertainties in the kinetics . . . 91
4.6 Conclusions . . . 93

5 Modeling synthetic spectra for transiting extrasolar giant planets: Detectability of H2S and PH3 with JWST 96
5.1 Introduction . . . 96
5.2 Methodology . . . 98
5.2.1 Chemical model . . . 99
5.2.2 Synthetic spectra model . . . 101
5.2.3 JWST noise model . . . 102
5.3 Results for abundance profiles . . . 104
5.3.1 Results for phosphorus species . . . 106
5.3.2 Results for sulfur species . . . 108
5.3.3 Results for C/N/O/H species . . . 108
5.3.4 Influence of insolation . . . 113
5.4 Results for noiseless spectra modeling . . . 114
5.4.1 PH_3 . . . 115
5.4.2 H_2S . . . 116
5.4.3 HCN . . . 118
5.5 Results for JWST transit spectra modeling . . . 120
5.5.1 Results for JWST noise modeling . . . 120
5.5.2 PH_3 . . . 123
5.5.3 H_2S . . . 124
5.6 Discussion . . . 125
5.7 Conclusions . . . 129

6 Conclusions and remaining questions 131

A Chemical pathway for CO/CH_4 conversion 135

B Chemical pathway for PH_3/H_3PO_4 conversion 140

C Chemical pathway for SiH_4 destruction 142

LIST OF TABLES

1.1 Composition of Jupiter's troposphere 1
1.2 Composition of Saturn's troposphere 2

3.1 Calculated K_{eddy} ($\mathrm{cm}^2\ \mathrm{s}^{-1}$) at T = 1000 K (near the CO quench level)[a] 29
3.2 Comparison between timescale approach and full diffusion-kinetic modeling using the *Venot model*. 42

4.1 Observed mixing ratios of some disequilibrium species 59
4.2 Elemental abundances used in the simulation for Jupiter and Saturn. 60

5.1 Parameters for computing noise - extension of Table 4 in Greene et al. [2016] 102
5.2 Fiducial planetary system parameters in the model 113

A.1 Non-equilibrium parameter f_{noneq} for reactions on the CO/CH_4 chemical pathway. 135

B.1 Non-equilibrium parameter f_{noneq} for reactions on the PH_3/H_3PO_4 chemical pathway. 140

C.1 Non-equilibrium parameter f_{noneq} for reactions on the SiH_4 destruction chemical pathway. 142

LIST OF FIGURES

2.1 Time evolution of the chemical species H, OH, C_2H_6 and NNH under constant temperature and pressure. Solid lines are computed using our code, and dashed lines are from Fig. 1 in Venot et al. [2012]. The initial condition is a mixture of gas H_2, He, O_2, CH_4, and N_2 with solar elemental abundances. 13

2.2 Comparison between our model and Venot et al. [2012] model on mole fraction profiles along Saturn's adiabat. Solid lines are from Fig. 1 in Mousis et al. [2014], which is computed using the Venot et al. [2012]'s model. Dashed lines are computed using our model. The elemental abundances we used here are O/H = 21 times solar, C/H = 9 times solar, and $K_{\rm eddy}$ = 1×10^9 cm^2 s^{-1}, the same as those used in Fig. 1 of Mousis et al. [2014]. 14

3.1 Normalization of vertical r.m.s. velocity $\sqrt{\overline{w'^2}}$ by $w_{\rm rot}$ and $w_{\rm fg}$, respectively. Vertical axis represents the height z (relative to the bottom of the tank) where $\sqrt{\overline{w'^2}}$ is measured. The data colored in red are extracted from Fig 16 in Fernando et al. [1991] and the data colored in blue are extracted from Fig 6 in Coates and Ivey [1997]. Different marker types correspond to different sets of experiments, with different rotation rates and prescribed heat fluxes. We only plot data with $z/l_{\rm rot} > 30$ ($Ro^\star < 0.03$), because that is where we expect rotating scaling applies. The data points should fall along a vertical line if the scaling could represent $\sqrt{\overline{w'^2}}$ well. 24

3.2 Scatterplot of B as a function of $Ro^\star$. $B = (\alpha g d\bar{T}/dz)/(\Omega^2)$, and $Ro^\star = l_{\rm rot}/h$. This figure is based on Fig 8 in Levy and Fernando [2002]. Black filled circles represent experimental data extracted from Fig 8 in Levy and Fernando [2002]. Solid curve is the fit using $B_{\rm norot}$ defined by equation (3.20), dashed line is the fit using $B_{\rm rot}$ defined by equation (3.17), and dotted curve is the fit using $B_{\rm fg}$ given by equation (3.19). The vertical line is showing the transition from high $Ro^\star$ regime to low $Ro^\star$ regime, corresponding to $Ro^\star_t$ = 0.015. 25

3.3 Profile of $K_{\rm eddy}$ (cm^2 s^{-1}) as a function of temperature T (K) and latitude ϕ (degrees) for Jupiter. On the figure, we denote the location of CO quench level at 9° N where a measurement of its mixing ratio is available [Bézard et al., 2002]. Our estimation gives $K_{\rm eddy} = (1.2 \pm 0.2) \times 10^8$ cm^2 s^{-1} at this location. 30

3.4 Profile of $K_{\rm eddy}$ (cm^2 s^{-1}) as a function of temperature T (K) and latitude ϕ (degrees) for Saturn. 31

3.5 Chemical constraints on Jupiter's deep water abundance using rate limiting step from Visscher and Moses [2011]. The green area between two curves indicates the allowed $E_{\mathrm{H_2O}}$ considering a factor of five uncertainty in rate coefficient of rate limiting step [Jasper et al., 2007, Visscher and Moses, 2011] and $X_{\mathrm{CO}} = (1.0 \pm 0.2) \times 10^{-9}$ [Bézard et al., 2002]. Using $K_{\mathrm{eddy}} = (1.2 \pm 0.2) \times 10^8$ cm^2 s^{-1} constrained at the location of measurement, we find $E_{\mathrm{H_2O}} = 0.1 \sim 0.75$, corresponding to the blue area in the figure. Dashed line indicates $E_{\mathrm{H_2O}}$ measured by Galileo Entry Probe [Wong et al., 2004]. 37

3.6 Chemical constraints on Saturn's deep water abundance using the the rate limiting step from Visscher and Moses [2011]. We consider two hypothetical tropospheric CO mixing ratio, namely, q_{CO} = 1×10^{-9} and q_{CO} =1×10^{-10}. The uncertainty indicated by shaded area is due to the factor of five uncertainty in the rate coefficient of the rate limiting step [Jasper et al., 2007, Visscher and Moses, 2011]. We did not impose a constraint on K_{eddy} since it sensitively depends on the latitude where CO measurement is taken. 38

3.7 Chemical constraints on Jupiter's deep water abundance using the CO kinetic model from Venot et al. [2012]. The green area indicates allowed $E_{\mathrm{H_2O}}$ considering a factor of two uncertainty in the rate coefficient and $X_{\mathrm{CO}} = (1.0 \pm 0.2) \times 10^{-9}$ Bézard et al. [2002]. Using $K_{\mathrm{eddy}} = (1.2 \pm 0.2) \times 10^8$ near 9° N, we find $E_{\mathrm{H_2O}} = 3 \sim 11$, corresponding to the blue area in the figure. 43

3.8 Chemical constraints on Saturn's deep water abundance using CO kinetic model from Venot et al. [2012]. We consider two hypothetical tropospheric CO mixing ratio, namely, q_{CO} = 1×10^{-9} and q_{CO} =1×10^{-10}. The uncertainty indicated by shaded area is due to the uncertainty of the rate coefficients. We did not impose a constraint on K_{eddy} since it sensitively depends on the latitude where CO measurement is taken. 44

3.9 Prediction of tropospheric X_{CO} as a function of latitude for a given $E_{\mathrm{H_2O}}$. We consider two CO kinetic models, namely, the *VM model* [Visscher and Moses, 2011] and the *Venot model* [Venot et al., 2012]. The error bar indicates the measurement of X_{CO} at 9 degrees by Bézard et al. [2002] 48

3.10 Prediction of $X_{\mathrm{PH_3}}$ as a function of latitudes for given values of $E_{\mathrm{H_2O}}$. The bulk phosphorus abundance is taken as X_{P} = 2.3×10^{-6} [Mousis et al., 2012]. The rate limiting step for PH_3 - P_4O_6 conversion is taken as equation (3.40) [Visscher and Fegley, 2005]. . . 49

4.1 Adiabatic profiles of Jupiter and Saturn computed following the method described in Fegley and Prinn [1985]. 61

4.2 Simulation results for Jupiter using the C/N/O/H reaction network. Upper left plot is the mixing ratio of species along Jupiter's adiabatic profile for parameters: $E_{\mathrm{H_2O}}$ = 10 and K_{eddy}=1×10^8 cm^{2}s^{-1} using the network A. Only species with mixing ratios $q > 1 \times 10^{-15}$ at 450 K are plotted. Upper right plot is the predicted mixing ratio of C_2H_6 as a function of K_{eddy} for a range of assumed water abundances. Solid lines are calculated using network A, and dashed lines are calculated using network B. Lower plots are the predicted mixing ratio of CO and CO_2 as a function of the water enrichment $E_{\mathrm{H_2O}}$ for different vertical eddy diffusion coefficient K_{eddy}. Solid lines are calculated using network A, and dashed lines are calculated using network B. . . 64

4.3 Simulation results for Saturn using the C/N/O/H reaction network. Upper left plot is the mixing ratio of species along Saturn's adiabatic profile for parameters: $E_{\mathrm{H_2O}}$ = 10 and K_{eddy}=1×10^8 cm^{2}s^{-1} using the network A. Only species with mixing ratios $q > 1 \times 10^{-15}$ at 400 K are plotted. Upper right plot is the predicted mixing ratio of C_2H_6 as a function of K_{eddy} for a range of assumed water abundances. Solid lines are calculated using network A, and dashed lines are calculated using network B. Lower plots are the predicted mixing ratio of CO and CO_2 as a function of the water enrichment $E_{\mathrm{H_2O}}$ for different vertical eddy diffusion coefficient K_{eddy}. Solid lines are calculated using network A, and dashed lines are calculated using network B. 65

4.4 Equilibrium mole fractions of phosphorus containing species along Saturn's adiabat computed using the NASA Chemical Equilibrium Application (CEA) software. The elemental input we used are P/H = 7.8 times solar, O/H = 10 times solar, and other elemental abundances are solar except He, C, N, S, Si, Ge, and As, which are listed in table 4.2. 67

4.5 The predicted mixing ratio of PH_3 as a function of the vertical eddy diffusion coefficient K_{eddy} in Jupiter's atmosphere at a few bars level. The horizontal dashed lines show the range of observed PH_3 mixing ratio $q_{\mathrm{PH_3}} = 7.0 \pm 1.0 \times 10^{-7}$ [e.g., Irwin et al., 1998]. The vertical dashed lines show the range of plausible eddy diffusion coefficient. 68

4.6 The predicted mixing ratio of PH_3 as a function of the vertical eddy diffusion coefficient K_{eddy} in Saturn's atmosphere at a few bars level.The horizontal dashed lines show the range of observed PH_3 mixing ratio $q_{\mathrm{PH_3}} = 4.0 \pm 1.0 \times 10^{-6}$ [e.g., Fletcher et al., 2011]. The vertical dashed lines show the range of plausible eddy diffusion coefficient. 69

4.7 Equilibrium mole fractions of some Si-bearing species along Saturn's adiabat computed using the NASA CEA code. The elemental input we used are Si/H = 10 time solar, O/H = 10 times solar, and other elemental abundances are solar except He, C, N, S, P, Ge, and As, which are listed in table 4.2. 73
4.8 Predicted mixing ratio of SiH4 as a function of the vertical eddy diffusion coefficient $K_{\rm eddy}$ for Saturn. Different oxygen abundances are explored. Si/H = 10 times solar in the calculation. . . 74
4.9 Equilibrium abundances of germanium containing species along Saturn's adiabat computed using NASA CEA code. We use Ge/H = 10 times solar, and O/H = 10 times solar. Other elemental abundances are also assumed to be solar except He, C, N, S, P, Si, and As, which are listed in table 4.2. 77
4.10 Predicted mole fraction of GeH_4 as a function of $K_{\rm eddy}$, the vertical eddy diffusion coefficient. The horizontal dashed lines show the range of observed mole fractions of GeH_4 [Bjoraker et al., 1986]. The vertical dashed lines show the plausible range of $K_{\rm eddy}$ for Jupiter. The blue dashed curves correspond to a factor of 5 uncertainty on both sides of the rate coefficient (total factor of 25). 78
4.11 Predicted mole fraction of GeH_4 as a function of $K_{\rm eddy}$, the vertical eddy diffusion coefficient. The horizontal dashed line shows the observed range for $X_{\rm GeH_4}$, which is $4 \pm 2 \times 10^{-10}$ [Noll et al., 1988]. The vertical dashed lines show the plausible range of $K_{\rm eddy}$ for Saturn. The blue dashed curves correspond to a factor of 5 uncertainty on both sides of the rate coefficient (total factor of 25). 79
4.12 The predicted mixing ratio of AsH_3 as a function of $K_{\rm eddy}$, the vertical eddy diffusion coefficient. The horizontal dashed lines show the observed AsH_3 mixing ratio, $q_{\rm AsH_3}$ = 2.2$\pm$1.1$\times10^{-10}$ [Noll et al., 1990]. The vertical dashed lines show the plausible range of $K_{\rm eddy}$ [Wang et al., 2015]. The observed abundance of AsH_3 corresponds to 0.3$\sim$0.8 times solar As/H ratio. 82
4.13 The predicted mixing ratio of AsH_3 as a function of $K_{\rm eddy}$, the vertical eddy diffusion coefficient. The horizontal dashed lines show the observed AsH_3 mixing ratio, $q_{\rm AsH_3}$ = 3$\pm$1$\times10^{-9}$ [Bézard et al., 1989, Noll et al., 1989, Noll and Larson, 1991]. The vertical dashed lines show the plausible range of $K_{\rm eddy}$ [Wang et al., 2015]. The observed abundance of AsH_3 corresponds to 5$\sim$10 times enrichment relative to solar. 83

4.14 Mole fraction of GeH_4 as a function of the latitude for Jupiter computed using the germanium chemical model. The horizontal profile of the vertical eddy diffusion coefficient used in the calculation is from Wang et al. [2015]. The horizontal dashed lines show the average mole fractions of GeH_4 over longitude and over latitude between -40° and 40°, corresponding to a value of $7\pm2\times10^{-10}$ [Bjoraker et al., 1986]. 87
4.15 Comparisons on the the predicted mixing ratios of CO among various reaction networks from the combustion community. All the reaction networks shown here have been validated against many combustion experiments. 89

5.1 Horizontally-averaged temperature-pressure profile for extrasolar giant planets computed using the approach in Parmentier and Guillot [2014], Parmentier et al. [2015]. Different lines correspond to different equilibrium temperatures, caused by the irradiation from the star. 105
5.2 Computed mole fractions of major phosphorus-bearing species (PH_3, PH_2, PH, HOPO, H_3PO_4, and P_2) in the atmospheres of extrasolar giant planets. Solid lines show the disequilibrium abundances computed using the diffusion-kinetic model, and the dashed lines show the abundances assuming local chemical equilibrium. The four plots correspond to different equilibrium temperatures: (a) $T_{\rm eq}$ = 500 K, (b) $T_{\rm eq}$ = 1000 K, (c) $T_{\rm eq}$ = 1500 K, (d) $T_{\rm eq}$ = 2000 K. The elemental abundances are summed to be one solar. The eddy diffusion coefficient $K_{\rm eddy}$ is set at 1×10^9 cm^2s^{-1}. 107
5.3 Computed equilibrium mole fractions of major sulfur-bearing species in the atmosphere of extrasolar giant planets. The disequilibrium calculations including vertical mixing are not done since the vertical mixing is not expected to change the profiles of H_2S. The four plots correspond to models with different equilibrium temperatures: (a) $T_{\rm eq} = 500K$, (b) $T_{\rm eq} = 1000K$, (c) $T_{\rm eq} = 1500K$, (d) $T_{\rm eq} = 2000K$. The elemental abundances used here is one solar. 109
5.4 Computed mole fractions of major C/N/O/S/P bearing species in the atmosphere of extrasolar giant planets. The four plots correspond to models with different equilibrium temperatures: (a) $T_{\rm eq}$ = 500 K, (b) $T_{\rm eq}$ = 1000 K, (c) $T_{\rm eq}$ = 1500 K, (d) $T_{\rm eq}$ = 2000 K. The elemental abundances used here is one solar. The vertical eddy diffusion coefficient used here is $K_{\rm eddy}$ = 1×10^9 cm^2 s^{-1}. . 110
5.5 Mole fractions at 1 bar as a function of the equilibrium temperatures of atmospheres. The species plotted are H_2O, CO, CH_4, CO_2, NH_3, N_2, HCN, H_2S, and PH_3. 112

5.6 Simulated transmission and emission spectra for *all species* (including H_2O, CO, CH_4, CO_2, NH_3, N_2, HCN, H_2S, and PH_3) compared with *all species except* PH_3. The difference between the blue curve and the green curve indicates the absorption from PH_3. The spectra are smoothed to a resolution of 100. 115
5.7 Simulated transmission and emission spectra for *all species* (including H_2O, CO, CH_4, CO_2, NH_3, N_2, HCN, H_2S, and PH_3) and *all species except* H_2S. The difference between the green curve and the blue curve indicates the absorption by H_2S. The spectra are smoothed to a resolution of 100. 117
5.8 Simulated transmission and emission spectra for *all species* (H_2O, CO, CH_4, CO_2, NH_3, N_2, HCN, H_2S, and PH_3) and *all species except* HCN. The difference between the green curve and the blue curve indicates the absorption by HCN. The spectra are smoothed to a resolution of 100. 119
5.9 Different noise components as a function of wavelength for selected JWST instruments and modes in Table 5.1. The target of the transit observation is a Sun-like at a distance of 50 pc with K-band magnitude of 6.8. The integration time is three hours in this calculation. 121
5.10 Total noise as a function of integration time for selected JWST instruments and modes in Table 5.1. The target of the transit observation is a Sun-like star at a distance of 50 pc with K-band magnitude of 6.8. The selected wavelength bins are at 2 μm, 5 μm, and 10 μm,respectively. 122
5.11 Synthetic transmission and emission spectra with simulated JWST noise for the planets presented in Table 5.2 with $T_{\rm eq}$ = 500 K. The blue curve is the spectra simulated including all nine species in Fig. 5.4, and the red curve is simulated including all nine species except PH_3. The simulated JWST instruments and modes are summarized in Table 5.1. 124
5.12 Synthetic transmission and emission spectra with simulated JWST noise for planets presented in Table 5.2 with $T_{\rm eq}$ = 1500 K. The blue curve is the spectra simulated including all nine species in Fig. 5.4, and the red curve is simulated including all nine species except H_2S. The simulated JWST instruments are summarized in Table 5.1. 125

A.1 Reaction path diagram for carbon bearing species generated by *Cantera*. The left figure is generated using the C/N/O/H reaction network A, and the right figure is generated using the network B. The composition and temperature-pressure condition resemble the CO quench level of Saturn ($\sim$ 900 K, 550 bars). The arrows show the flow directions of element carbon, and the labels show the net flux (in the unit of mole cm^{-3} s^{-1}) of element carbon as well as the forward flux and backward flux. The reactions responsible for the forward and backward flux are also labeled. All the carbon bearing species are considered, but only fluxes above a threshold are shown in the diagram. 136

B.1 Reaction path diagram for phosphorus bearing species generated by *Cantera*. The input reaction network here is the H/P/O network described in Chapter 2. The arrows in the diagram show the flow directions of element phosphorus. The labels show the net element flux (in the unit of mole cm^{-3} s^{-1}) as well as the forward flux and the backward flux. The reactions responsible for the forward and backward flux are also labeled. All species in the network are considered, but only species that have net flux above a threshold are shown in this figure. 141

C.1 Chemical pathway for silicon bearing species generated by *Cantera*. The input reaction network here is the H/Si/O network described in chapter 2. The arrows show the flow directions of element silicon. The labels show the net flux (mole cm^{-3} s^{-1}) of element silicon as well the forward flux and the backward flux. Also labeled are the reactions responsible for the forward and backward flux. All species in the network are considered, but only species that have net flux above a threshold are shown in the diagram. 143

CHAPTER 1

INTRODUCTION

Jupiter's atmosphere is primarily composed of hydrogen, helium, and a small fraction of heavy elements. These heavy elements are crucial for understanding the formation of Jupiter and planetary systems in general. Any plausible formation models should produce a heavy element enrichment that is consistent with current observations. How do we determine the amount of heavy elements in Jupiter? Assuming the envelope of Jupiter is well mixed, the total amount of heavy elements can be derived by measuring the abundances of major heavy-element bearing molecules, such as H_2O, CH_4, and NH_3, in the atmospheres. The most accurate measurements of Jupiter's atmospheric composition comes from the Galileo entry probe. In Table 1.1, we summarized the measurements from Galileo entry probe. The abundances of CH_4, NH_3, H_2S, and PH_3 have been measured, indicating a $2 \sim 4$ enrichment for heavy elements. One missing part is the water abundance. The water abundance measured by Galileo entry probe, which is about 0.5 time solar, only represents a lower limit because the measurements are affected by dynamic effects that depleted the water vapor in the sampled region. However, the water abundance is necessary to

Table 1.1 Composition of Jupiter's troposphere

	q	E	references
He	0.157 ± 0.030	0.920 ± 0.176	Niemann et al. [1998]
CH_4	$(2.37 \pm 0.57) \times 10^{-3}$	4.4 ± 1.0	Wong et al. [2004]
NH_3	$(6.64 \pm 2.54) \times 10^{-4}$	4.9 ± 1.9	Wong et al. [2004]
H_2O	$\geq (4.9 \pm 1.6) \times 10^{-4}$	$\geq 0.50 \pm 0.16$	Wong et al. [2004]
H_2S	$(8.9 \pm 2.1) \times 10^{-5}$	3.4 ± 0.8	Wong et al. [2004]
PH_3	$(7.7 \pm 0.2) \times 10^{-7}$	1.50 ± 0.04	Irwin et al. [1998]
Ar	1.82×10^{-5}	3.6 ± 0.5	Mahaffy et al. [2000]
Kr	9.3×10^{-9}	2.4 ± 0.5	Mahaffy et al. [2000]
Xe	8.9×10^{-10}	2.3 ± 0.5	Mahaffy et al. [2000]

place constraints on the conditions of the protoplanetary disk, as well as the total amount of heavy elements in Jupiter. One of the primary scientific goal of the ongoing Juno mission is to measure the deep water abundance of Jupiter. Juno carries a microwave radiometer that is expected to measure the deep water abundance down to 100 bars. However, the measurement is difficult, since the primary absorber of microwave radiation is from ammonia instead of water.

Similar to Jupiter, Saturn's atmosphere is also primarily composed of hydrogen, helium, and small fraction of heavy elements. The determination of heavy element abundances in Saturn is important for constraining the condition of protoplanetary disk where Saturn was formed. In addition, the elemental composition of both Jupiter and Saturn can place strong constraints on the general theory of planet formation. Saturn's atmospheric composition are less

Table 1.2 Composition of Saturn's troposphere

	q	E	references
He	0.135 ± 0.025	0.794 ± 0.147	Conrath and Gautier [2000]
CH_4	$(5.3 \pm 0.2) \times 10^{-3}$	9.9 ± 0.8	Fletcher et al. [2009b]
NH_3	$(3.40 \pm 2.27) \times 10^{-4}$	2.5 ± 1.7	Fletcher et al. [2011]
H_2O	$\geq 2 \times 10^{-7}$	$\geq 2\times 10^{-4}$	de Graauw et al. [1997]
H_2S	3.76×10^{-4}	14.3	Briggs and Sackett [1989]
PH_3	$(4.4 \pm 1.2) \times 10^{-6}$	8.5 ± 2.3	Fletcher et al. [2011]

constrained than Jupiter and the measurements are mostly from remote sensing. In table 1.2, we summarized the composition of Saturn troposphere as measured through Cassini, Voyager, and ground-based telescopes. Similar to Jupiter, the elemental compositions for C, N, S, and P are enriched relative to solar. The deep abundance of water is also unknown due to the deep condensation level of water. A Saturn entry probe has been proposed a candidate for the new frontiers program, which has the goal of making in-situ measurements of

the atmospheric composition. However, this probe may not be able to descent deep enough to directly measure the deep water abundance.

An alternative way of constraining Jupiter and Saturn's deep water abundance is through the disequilibrium species. Disequilibrium species, such as CO, were observed in the atmospheres of Jupiter and Saturn, with abundances order-of-magnitude higher than that predicted by local chemical equilibrium. The chemistry of these species is driven out of equilibrium due to the fast vertical convection. Chemically, CO is related to H_2O. The more H_2O, the more CO. Therefore, CO abundance is indicative of the H_2O abundance. In principal, if we parameterize the vertical mixing process using an eddy diffusion coefficient, the observed CO abundance should be a function of the deep eddy diffusion coefficient and the deep water abundance. This approach has long been developed to constrain the deep water abundance for both Jupiter and Saturn. However, several big uncertainties remain. First, the eddy diffusion coefficient, which is used to parameterize the efficiency of vertical mixing of chemical species, suffers from orders of magnitude uncertainties. Such large uncertainty usually renders a large uncertainty on the constrained deep water abundance. Second, chemical networks used in the modeling were not tested against any experiments, which therefore have additional difficult to quantify uncertainties. Can we address these uncertainties and improve the chemical constraints on the deep water abundances for Jupiter and Saturn? This is the question we aimed to address in this dissertation.

In addition, since CO is dependent on both eddy diffusion coefficient and the deep water abundance, knowing CO alone cannot effectively constrain the deep water abundance. In order to waive the degeneracy between water abundance

and eddy diffusion coefficient, another disequilibrium species may be needed other than CO. Are there other chemical species that have a different dependence on the eddy diffusion coefficient and deep water abundance, so that the degeneracy can be broken? This is another question we aimed to address in this dissertation. This question is especially important for a shallow Saturn entry probe, since the probe may have the capability to measure the abundances of several different disequilibrium species including CO, but does not have the capability to make in-situ measurements of the deep water abundance.

Outside our solar system, nowadays thousands of planets have been discovered. The detection and characterization of extrasolar planets will provide many more samples for constraining planet formation models. The atmospheres of several extrasolar giant planets have been characterized through transit spectroscopy. Water has been detected in several hot extrasolar giant planets using the Hubble space telescope. James Webb Space Telescope (JWST), the next generation space telescope to launched in 2018, s expected to acquire the best quality transit spectra for extrasolar giant planets, allowing detection and measurement of several abundant molecules such as H_2O, CO, CH_4, or NH_3. Less abundant molecules such as H_2S and PH_3 have been detected in the atmospheres of Jupiter and Saturn, but their presence and detectability is unknown for extrasolar giant planets. Are H_2S and PH_3 important for the transit spectra? Can we detect these molecules with JWST? These questions are important in two ways. First, current retrieval techniques only considers H_2O, CO, CH_4, or NH_3 as the main contributors to the transit spectra. However, the influence of H_2S and PH_3 on the spectra was not accounted. It is necessary to evaluate how H_2S and PH_3 can affect the transit spectra and the robustness of the retrieved abundances. Second, H_2S and PH_3 have never been detected in the atmospheres of extraso-

lar giant planets. Our study here will identify the parameter space of planets that are likely to have detectable spectra features of H_2S or PH_3.

My dissertation is organize as the follows. In Chapter 2, we described the chemical models we developed in this dissertation. including the equilibrium model, the diffusion-kinetic model, and the timescale model. The suite of models are publicly available and can be used to reproduce the work presented in this dissertation. In Chapter 3, we revisited the approach of constraining the deep water abundance using the tropospheric CO abundance. We improved two key components in this approach: the deep eddy diffusion coefficient and the chemical kinetic networks. We derived new chemical constraints on the deep water abundance in both Jupiter and Saturn. In Chapter 4, we model the chemistry of H/C/O/N/P/Si/Ge/As in the deep atmospheres of Jupiter and Saturn, and identified C_2H_6 as the tracer for the deep eddy diffusion coefficient, while CO is dependent both on the deep eddy diffusion coefficient and water abundance. Based on this result, we devised an approach for constraining both the deep water abundance and the deep eddy diffusion coefficient with a shallow entry probe. In Chapter 5, we model the chemistry of extrasolar giant planets with different levels of insolation, and model the synthetic transit spectra with JWST instrumental noise for each type of planets. The synthetic spectra were used to evaluate the detectability of molecules, particularly H_2S and PH_3 with JWST observations. In Chapter 6, we summarize the results of this dissertation, and highlight several remaining questions that merit future exploration.

CHAPTER 2

ONE DIMENSIONAL CHEMICAL MODELS FOR PLANETARY ATMOSPHERES

2.1 Introduction

The composition of planetary atmosphere is important for understanding the formation and history of the planet, the dynamics of the planet, as well as the habitability of the planet. The composition of planets can be determined either by remote spectroscopy or in-situ measurements. A chemical model is used to interpret the measurements to understand the elemental composition of the planet and the dynamics of the planet. For giant planets in our solar system, one-dimensional chemical models are used to predict the vertical distribution of chemical species since the temperature and pressure gradients are primarily along the vertical direction. The horizontal temperature and pressure gradients are small compared with the vertical gradients. For extrasolar giant planets, the horizontal temperature and pressure gradients can be large if the planet is tidally locked and irradiated on one side. In this case, the compositions can be different between the dayside and the night side of the planet, so at least a two dimensional model should be used. However, the heat redistribution between the dayside and nightside is not clear for exoplanets. Traditionally, one dimensional model are still be used, but the results should be interpreted as some sort of average between the dayside and the night.

In this chapter, we present the chemical models developed in my dissertation. The links to the codes are also provided. The suite of codes can be used to model equilibrium chemistry, as well as the transport-induced disequilib-

rium chemistry for carbon (C), oxygen (O), nitrogen (N), phosphorus (P), silicon (Si), germane (Ge), and arsenic (As). In section 2.2, we describe the equilibrium models used in this dissertation. The equilibrium model only accounts for the chemical conversions that determine the composition of the atmosphere. In section 2.3, we describe the diffusion kinetics model that adds the effect of atmospheric motions on the compositions. In section 2.4, we describe a simplification of the diffusion kinetics model, which is useful when the full reaction network is not available. We did not consider the effect of photochemistry, and the influx/outflux at the boundaries. Therefore, our models here are applicable to the deep part of the atmospheres where photochemistry and outflow are unimportant.

2.2 Equilibrium model

Equilibrium models assume chemical equilibrium among chemical species in a localized region of the atmospheres. The concentrations of molecular species are only a function of local temperature and pressure. This model seems unrealistic since the atmosphere is not static and the vertical motions can break the local chemical equilibrium. However, it is still a good approximation for atmospheres where the temperature and pressure are high enough that the chemical conversion timescale is much smaller than the dynamic timescale. This happens in the very deep part of giant planets. Therefore, the equilibrium model can provide a good lower boundary condition for the atmospheres of giant planets. For extrasolar giant planets that are high irradiated, the temperature is very high, and chemical equilibrium is a good approximation for up to the troposphere.

The chemical equilibrium state is usually computed via the minimization of Gibbs free energy of the system. The inputs are the molecules and their Gibbs free energy of formation, the elemental composition, and the pressure and temperature. The model should minimize the total Gibbs free energy with respect to the mole fractions of molecules, while maintaining the constraint that the elemental mass is conserved. We use two implementations of this approach in this dissertation. One is the NASA Chemical Equilibrium Application (CEA) [Gordon and McBride, 1994, McBride and Gordon, 1996]. This code includes about 2000 chemical species. The other code is *cantera*, a software toolkit developed for chemical kinetics [Goodwin et al., 2015], but it also has an equilibrium solver. Both codes can return the mass fractions of chemical species for an input pair of pressure and temperature, and the elemental composition.

2.3 Diffusion kinetics model

2.3.1 Introduction of the diffusion kinetic code

The equilibrium model is not sufficient for modeling the tropospheres of giant planets since the motions of atmospheres tend to drive the composition out of equilibrium state. The detections of disequilibrium species in the upper atmospheres of Jupiter and Saturn indicate that vertical mixing is important between a few bars and a few hundred bars region in both planets. The diffusion kinetic model has been used to model the atmospheric composition when vertical mixing is important. In this dissertation, we develop a code to solve the one

dimensional diffusion kinetic equation:

$$\frac{\partial Y_i}{\partial t} = \frac{1}{\rho}\frac{\partial}{\partial z}(\rho K_{\rm eddy}\frac{\partial Y_i}{\partial z}) + P_i - L_i, \tag{2.1}$$

where Y_i is the mass fraction of species i, ρ is the density of the atmosphere, z is the vertical coordinate relative to a reference point in the atmosphere (we choose the 1 bar level in the code), $K_{\rm eddy}$ is the vertical eddy diffusion coefficient, P_i is the chemical production rate of species i, and L_i is the chemical loss rate of species i. Both P_i and L_i have a unit of g cm^{-3} s^{-1}. Strictly speaking, the mass fraction Y_i being modeled here is an averaged quantity in the spacial dimension, but the chemical reaction rates are nonlinear on the mass fractions, so the average of the reaction rate within the grid is not necessarily equal to the reaction rates that computed using the averaged mass fractions. The underlying assumption for this equation to hold is that the temperature fluctuation within the grid is very small. This is a good assumption for Jupiter and Saturn's atmosphere at a few hundred bars level, where the temperature fluctuation is indeed very small. The time evolution of Y_i is controlled by two physical processes: one is the chemical production and destruction of species i, and the other is its corresponding vertical transport. In the convective envelope of Jupiter and Saturn, the transport of mass is mainly by turbulent convection. Here in equation (2.1), the convective transport of species is approximated by diffusion transport with an coefficient $K_{\rm eddy}$, which is a good approximation justified by the success of mixing length theory in explaining stellar convection [Stone, 1976]. The mass fractions Y_i are initialized using their local chemical equilibrium values along the adiabat. The chemical net production rate ($P_i - L_i$) is integrated using *Cantera*, a software toolkit developed for problems involving chemical kinetics and thermodynamics [Goodwin et al., 2015]. At each time step, we call *Cantera* to do the integration and include the result in the resolution of the continuity

equation. *Cantera* has been used and tested for many applications including combustion, detonation, fuel cells, batteries, etc. The integration is terminated when the mass fractions Y_i reach steady state. The code requires three kinds of input. One is the temperature pressure profile ($T - P$ profile), the second is a list of thermodynamic properties in the format of NASA polynomials [McBride et al., 1993] for each species, and a list of reactions between these species, the third is the elemental composition and the vertical eddy diffusion coefficient $K_{\rm eddy}$.

We have compiled several updated reaction networks for modeling the chemistry of C/N/O/H/P/Si bearing species. We describe these reaction networks here.

- *C/N/O/H reaction network*

  Our C/N/O/H reaction network used in this paper is developed based on the network from Venot et al. [2012] downloaded from the KIDA database [Wakelam et al., 2012, `http://kida.obs.u-bordeaux1.fr`]. The network consists of 105 neutral species and 963 reactions. Among the reactions, 957 of them are reversible reactions and 6 of them are irreversible reactions. A complete list of the species can be found in Venot et al. [2012]. The network has been validated against various combustion experiments in the temperature range between 300 K and 2000 K and in the pressure range between 0.01 bar and several hundred bars.

  An alternative network applied to the hydrogen-rich atmospheres is that of Moses et al. [2011] and Visscher and Moses [2011]. Moses [2014] compared their model with the Venot et al. [2012] model and found that the major difference in CO/CH_4 chemistry comes from the rate coefficient of

the reaction H + $CH_3OH \leftrightarrow CH_3$ + H_2O. The Venot et al. [2012] model used the rate coefficient obtained by Hidaka et al. [1989] from laboratory experiments. However, Moses [2014] argued that this reaction likely is prohibited by a very large energy barrier and is much slower than was estimated by Hidaka et al. [1989] based on quantum chemical calculations in Moses et al. [2011]. It remains to be seen whether changing the rate coefficient following the suggestions by Moses et al. [2011] would reproduce the experimental results in Hidaka et al. [1989]. Therefore, because the discrepancy remains unresolved, we have considered two reaction networks in our model, which are:

- *network A*: it is based on the Venot et al. [2012] network with some modifications. Among the species in the list, we remove HNC because it does not participate in any reactions in the reaction network. We include CH_3HN_2, CH_3HN, CH_2NH2, and CH_2NH into the network since these species are expected to be important in a hydrogen rich environment [Moses et al., 2010]. The final network A consists of 108 species and 1000 reactions. Added reactions and their rate coefficients are from Dean and Bozzelli [2000]. The thermodynamic properties are mainly compiled from Burcat and Ruscic [2005], McBride et al. [1993], Dean and Bozzelli [2000] and Venot et al. [2012]. An online updated version of the Burcat and Ruscic [2005] database can be found at `http://garfield.chem.elte.hu/Burcat/burcat.html`. The whole reaction list along with thermodynamic data and rate coefficient data are available in the KIDA database (`http://kida.obs.u-bordeaux1.fr/networks.html`).
- *network B*: it is the same as the network A except the rate coefficient

for the reaction H + $CH_3OH \leftrightarrow CH_3$ + H_2O is revised to be much slower following the recommended rate in Moses et al. [2011]. The slower rate leads to nearly two orders of magnitude increase in the CO/CH_4 conversion timescale near the quench level.

- *H/P/O reaction network*

  The H/P/O reaction network is based on Twarowski [1995]. The reaction network consists of 24 species and 175 reactions. The phosphorus containing species included are: PH_3, PH_2, PH, HOPO, HPO, PO, PO_2, PO_3, $HOPO_2$, P_2O_3, P, P_2, P_4, P_2O, P_2O_2, HPOH, H_2POH. The network has been used to explain the faster recombination rate of H and OH in the presence of phosphine combustion products [Twarowski, 1996]. To make sure all important species under Jupiter/Saturn's atmospheric conditions are included, we performed an equilibrium calculation using the NASA Chemical Equilibrium Application (CEA) [Gordon and McBride, 1994, McBride and Gordon, 1996] for temperature and pressure conditions along the adiabats of Jupiter and Saturn. We find H_3PO_4 is important but missing from this reaction network, so we added it and associated reactions into the reaction network. The thermodynamic data are primarily from Burcat and Ruscic [2005], McBride et al. [1993]. The thermodynamic data for P_2O and P_2O_2 are from Twarowski [1993]. The whole reaction network is available in the KIDA database.

- *Si/O/H reaction network*

  The Si/O/H reaction network is from Miller et al. [2004]. The network consists of 69 species and 198 reactions. The silicon bearing species included in the network are: Si, Si_2, Si_3, SiH, SiH_2, cis-$OSiH_2O$, Si_2H_2, SiH_4, SiH_3, H_3SiSiH_3, H_3SiSiH, H_2SiSiH_2, Si_2H_5, Si_2H_3, Si_2O_2, Si_3O_3, Si_4O_4,

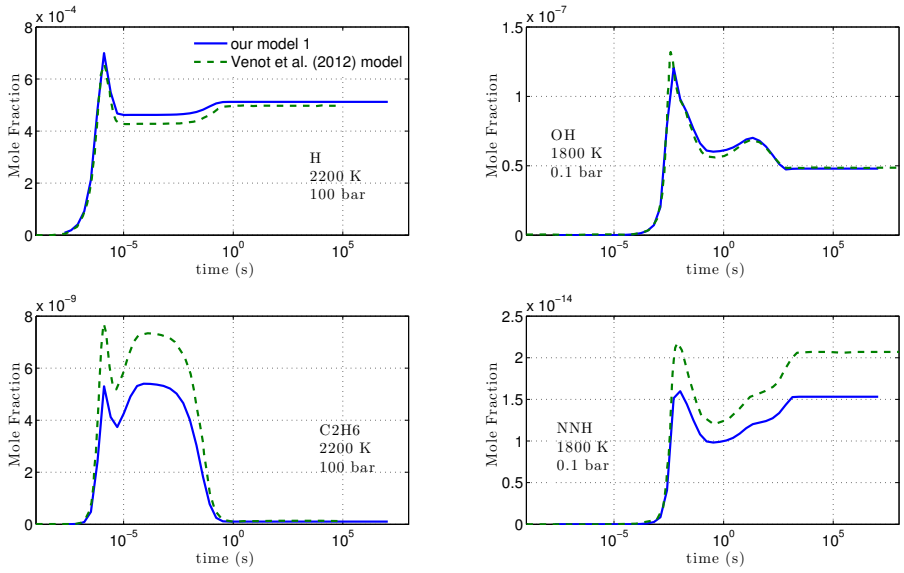

Figure 2.1 Time evolution of the chemical species H, OH, C_2H_6 and NNH under constant temperature and pressure. Solid lines are computed using our code, and dashed lines are from Fig. 1 in Venot et al. [2012]. The initial condition is a mixture of gas H_2, He, O_2, CH_4, and N_2 with solar elemental abundances.

Si_5O_5, Si_6O_6, Si_7O_7, Si_8O_8, Si_9O_9, $Si_{10}O_{10}$, $(SiH_2O)_2$, SiO_2, $H_3SiOSiH_3$, H_3SiOOH, H_3SiOO, $SiOOH$, H_2SiOH, H_3SiO, $HOSiO_2$, SiO, $Si(OH)_2$, $SiOH$, $H_2Si(OH)O$, H_3SiOH, $HSiOH$, $HSiO$, H_2SiO, $HSiO(OH)$, $HSiO_2$, $HOSiO$, $HSiOOH$, $SiO_2(c)$, $SiO_2(l)$, $SiO_2(g)$, H_2SiOOH, $(HSiOOH)_2$, Si_2O_4, Si_3O_6, Si_4O_8, Si_5O_{10}, Si_6O_{12}, Si_7O_{14}, Si_8O_{16}, Si_9O_{18}, $Si_{10}O_{20}$. This network has been used to model the combustion of silane (SiH_4). The whole reaction network is available in the KIDA database.

2.3.2 Validation of the diffusion kinetic code

We first test our code without diffusion using the C/N/O/H reaction network computing the time evolution of the abundances of different species at constant

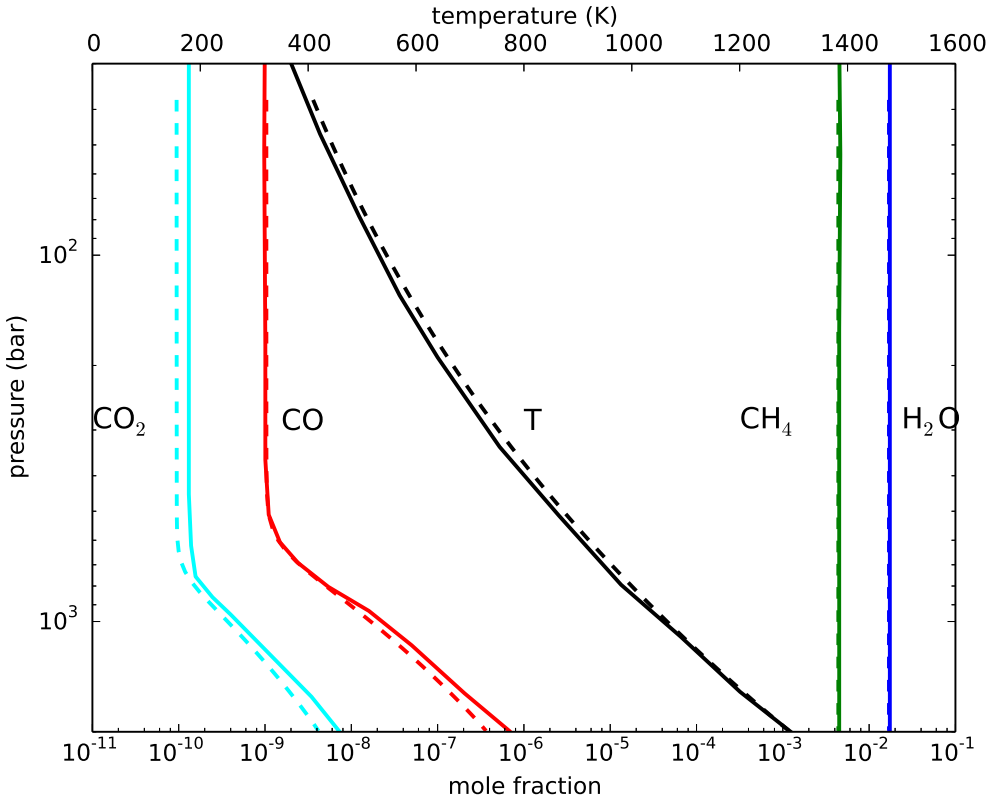

Figure 2.2 Comparison between our model and Venot et al. [2012] model on mole fraction profiles along Saturn's adiabat. Solid lines are from Fig. 1 in Mousis et al. [2014], which is computed using the Venot et al. [2012]'s model. Dashed lines are computed using our model. The elemental abundances we used here are O/H = 21 times solar, C/H = 9 times solar, and $K_{\rm eddy} = 1\times10^9$ cm^2 s^{-1}, the same as those used in Fig. 1 of Mousis et al. [2014].

temperature and pressure. The integration is done using *Cantera*. A comparison between our results and those from the nominal model of Venot et al. [2012] is shown in Fig. 2.1. The evolution is very similar for H and OH, but not exactly the same for C_2H_6 and NNH. The difference is due to the thermodynamic properties utilized. Indeed, we have changed the thermodynamic data to those provided in Venot et al. [2012] and exactly obtained the same evolution of the abundance profiles for all four species. This prompts us to compare the thermodynamic data we used with those in Venot [2012]. Our thermodynamic data are gathered from widely used compilations, for example, McBride et al. [1993] and Burcat and Ruscic [2005]. The species that are not available from literature are estimated using the software THERM [Ritter, 1991]. Venot et al. [2012] also gathered thermodynamic data in a similar manner. However, we do not know the source of thermodynamic data for each species in Venot et al. [2012], therefore, comparisons for individual species are not possible. This is not expected to be a major source of uncertainty since the uncertainties in the kinetic data are much larger than those in the thermodynamic data.

The test with both kinetics and diffusion is done by simulating the Saturn's atmosphere thermochemistry using the C/N/O/H reaction network, and comparing against the results in Fig. 1 of Mousis et al. [2014]. The reference result in Mousis et al. [2014] for Saturn is computed using the same code as in Venot et al. [2012]. The comparison, represented in Fig. 2.2, shows that the differences in the mixing ratios are within 10%. There might be three sources of error that contribute to the differences of the mixing ratios shown in Fig. 2.2: (1) the temperature-pressure profile; (2) the thermodynamic data; (3) the elemental abundances, which are all inputs to our code. These difference are small and the comparison shows our code can correctly solve the diffusion-kinetics Equation

(2.1).

2.4 Timescale model

The timescale model has long been used to model the chemistry of disequilibrium species [Prinn and Barshay, 1977, Bézard et al., 2002]. It only requires a rate limiting reaction instead of the full reaction network to approximate the abundance of disequilibrium species. Therefore, it is useful when the full reaction network is not available due to the lack of reaction rates data. The idea of this approach is the following. There are two physical process that determine the abundance of chemical species. The overturning of convective eddies tend to homogenize the abundances of chemical species, while the chemical reactions tend to relax the gas to local chemical equilibrium state, which creates a gradient on the abundances. In the deep and hot part of the atmosphere, the chemical reaction proceeds fast, so the system can relax to local chemical equilibrium in a short timescale. When this chemical timescale is smaller than the overturning timescale, the system is approximately in local chemical equilibrium state. On the other hand, in the cold and upper part of the atmosphere, the chemical reactions are slow, and the corresponding chemical timescale is longer than the overturning timescale. We say the chemical reaction is quenched, and the overturning of eddies homogenize the abundances of chemical species. The level where the chemical timescale is equal to the overturning timescale is define as the *quench level*. The timescale approach computes the chemical timescale and overturning timescale along the vertical $T - P$ profile, then finds the *quench level*. The abundance of disequilibrium species is then homogeneous above the *quench level*, and in local chemical equilibrium below the *quench level*. This is

a good approximation to solving the full diffusion kinetic equation under two assumptions: first, the correct rate limiting step is used; second, the overturning timescale is computed following the recipe described in Smith [1998].

CHAPTER 3

NEW INSIGHTS ON JUPITER'S DEEP WATER ABUNDANCE FROM TROPOSPHERIC CARBON MONOXIDE ABUNDANCES

3.1 Introduction

The bulk abundances of oxygen in Jupiter and Saturn potentially constrain conditions in the Sun's protoplanetary disk. However, determining these abundances through the direct measurement of water, the dominant carrier of oxygen in the envelopes of these objects, is very difficult. Galileo probe measurements show the effect of dynamical processes on the water abundance down to 22 bars [Wong et al., 2004], while ground-based microwave observations are not sufficiently sensitive to provide a deep water abundance (that is, below the meteorological layer) for either body [de Pater and Massie, 1985]. A determination of the deep ($>$ 50 bar) water abundance on Jupiter should be obtained by the microwave radiometer aboard the Juno spacecraft [Janssen et al., 2005, Helled and Lunine, 2014]. There is no similar possibility for Saturn in the near future because, even though the Cassini spacecraft will be put in a Juno-like orbit in 2017, it does not carry a microwave radiometer.

An alternative way to determine water abundance, through disequilibrium species observed in Jupiter and Saturn's troposphere, is a long-standing approach that goes back to Prinn and Barshay [1977] (see Visscher and Moses [2011] for an extensive list of published papers on this subject). The abundance of disequilibrium species depends on the relevant chemical kinetics, which determines the chemical loss rate, and the eddy diffusion coefficient, which determines the efficiency of vertical mixing. Our study is timely, in spite of the long

history of published papers, for three reasons. First, we derived a new formulation of the eddy diffusion coefficient based on laboratory studies of turbulent rotating convection. The new formulation systematically describes the transition from slow-rotation convection to rapid-rotation convection with significantly less uncertainty than previously. Secondly, we used the two most updated CO kinetic models to place constraints on Jupiter's deep water abundance. Third, a possible future mission to deploy a descent probe into Saturn's atmosphere, if conducted, will almost certainly be a "New Frontiers" medium-class mission [Board et al., 2012], or an ESA M-class mission [Mousis et al., 2015]. Such a probe will probably not be able to get to the base of the water cloud which is essential to determining directly the deep oxygen abundance on Saturn. Indirect methods including using disequilibrium species as described here may be the only way to determine oxygen abundance even through probe measurements, and therefore a study is warranted using the most recent kinetics to assess whether such an approach provides a well-constrained oxygen value. Our results identify and quantify significant ambiguities inherent in such an approach.

The paper is organized as follows. In section 3.2, we analyze the results from rotating tank experiments and propose a new formulation of eddy diffusion coefficient. In section 3.3, we derive constraints on the deep water abundance from CO measurements with the kinetic information from two different models. In section 3.4, we discuss the implication on Jupiter's formation and potential improvements relative to the current model.

3.2 A New Formulation for the Deep Eddy Diffusion Coefficient

In the atmosphere of Jupiter, heat is assumed to be transported by vertical eddy diffusion. The eddy diffusion coefficient $K_{\rm eddy}$ is introduced to measure the efficiency of vertical diffusion. In the convective part of the atmosphere, the heat flux and superadiabatic temperature gradient can be related to $K_{\rm eddy}$ by the following equation:

$$F = -\rho c_p K_{\rm eddy}(\frac{dT}{dr} - \frac{dT}{dr}|_{ad}), \tag{3.1}$$

where F is the internal heat flux, ρ is the mass density, c_p is the specific heat per unit mass, and $dT/dr - dT/dr|_{ad}$ is the superadiabatic temperature gradient. Formulations of $K_{\rm eddy}$ in terms of heat flux F, rotation rate Ω and fluid thermal properties are derived based on mixing length theory or perturbation of linearized equations [Stone, 1976, Flasar and Gierasch, 1978, Stevenson, 1979], predicting $K_{\rm eddy}$ near CO quench level ($\sim$ 1000 K, 300 bars) for Jupiter to be between 1×10^7 cm^2 s^{-1} and 1×10^9 cm^2 s^{-1} [e.g., Bézard et al., 2002, Visscher et al., 2010], and this value is widely used in theoretical modeling of disequilibrium chemistry. One difficulty in improving the estimation is the lack of observation. No natural convective system under rapid rotation, like the interior of giant planets or the Earth core, can be easily observed. However, the estimation of $K_{\rm eddy}$ could be improved by utilizing results from laboratory studies on turbulent rotating convection. Laboratory studies on turbulent rotating convection have been done since 1980s, however, application to giant planet convection has hitherto been limited. Here, we summarize relevant results of these laboratory studies, and propose a new formulation of $K_{\rm eddy}$.

In section 2.1, we review theoretical investigations on $K_{\rm eddy}$. In section 2.2, we summarize results from rotating tank experiments, and present the new formulation for $K_{\rm eddy}$. In section 2.3, we apply the new formulations to Jupiter and Saturn, and predict $K_{\rm eddy}$ profiles for these two planets.

3.2.1 Theory on Eddy Diffusion Coefficient

By analogy to molecular diffusion coefficient, $K_{\rm eddy}$ can be approximated as the product of vertical convective velocity w and a mixing length l, representing a typical distance a parcel could travel before it lost its identity. Therefore, equation (3.1) can be rearranged as

$$F \sim -\rho c_p w \delta T, \tag{3.2}$$

where $\delta T = (dT/dr - dT/dr|_{ad})l$ is the temperature fluctuation. A parcel's kinetic energy is obtained from the work done by buoyancy force over a mixing length l, thus

$$w^2 \sim -\alpha g \delta T l, \tag{3.3}$$

where α is the thermal expansion coefficient and g is the acceleration of gravity. With equation (3.2) and (3.3), we find the convective velocity

$$w \sim (\frac{\alpha g F}{\rho c_p} l)^{1/3}. \tag{3.4}$$

The mixing length is usually assumed to be a pressure scale height H, thus eddy diffusion coefficient can be estimated as [Stone, 1976]

$$K_{\rm eddy} \sim wl \sim (\frac{\alpha g F}{\rho c_p} H)^{1/3} H, \tag{3.5}$$

Stone [1976]'s estimation ignored the effect of rotation on $K_{\rm eddy}$, however, rotation could have an important effect on convection in suppressing vertical mix-

ing [Bagenal et al., 2004]. The importance of rotation can be measured by a Rossby number

$$Ro = \frac{v}{fl}, \tag{3.6}$$

where $f = 2\Omega sin\phi$ is the Coriolis parameter, and ϕ is the latitude. The Rossby number is defined as the ratio of inertial to Coriolis force, therefore, lower Ro means Coriolis acceleration is more important. Near the CO quench level, we find $Ro \approx 0.01/(sin\phi)$. Therefore, near the equator, rotation has little effect, while at extra-equatorial latitudes, rotation is important in suppressing turbulent convection.

The trend is consistent with Flasar and Gierasch [1978]'s results. In the limit of rapid rotation, Flasar and Gierasch [1978] analyzed the linear modes generated by the perturbation of a superadiabatic and inviscid fluid in plane geometry, and identified the most unstable modes that transport the most heat. Assuming shear instability limits the growth rate, they found

$$K_{\rm eddy} \sim (\frac{\alpha g F}{\rho c_p})^{3/5} (\frac{H}{2\Omega sin\phi})^{4/5}, \tag{3.7}$$

and

$$w \sim (\frac{\alpha g F}{\rho c_p})^{2/5} (\frac{H}{2\Omega sin\phi})^{1/5} \tag{3.8}$$

at extra-equatorial regions, while near the equator, the formulation is the same as equations (3.4) & (3.5). (Equations (3.7) and (3.8) are rearranged from equation (5.3) in Flasar and Gierasch [1978])

Equations (3.5) and (3.7) are widely used in estimating $K_{\rm eddy}$ [e.g., Bézard et al., 2002, Visscher et al., 2010]. In comparison to equations (3.5) and (3.7), laboratory experiments on turbulent rotating convection indicate the same scaling as equation (3.5) for slow rotation, but a different scaling from equation (3.7) for

rapid rotation. We will discuss the new scalings from rotating tank experiments in section 2.2, but here we will show that the new scalings can be easily derived based on the assumption that overturning timescale is limited by the rotational timescale Ω^{-1}, instead of H/w. With this assumption, the relevant length scale would be $l = w/\Omega$, and the velocity scale would be

$$w \sim (\frac{\alpha g F}{\rho c_p \Omega})^{1/2}, \tag{3.9}$$

according to equations (3.2) and (3.3). This velocity scale was found to be consistent with the convective velocity data from a three dimensional anelastic simulation of the convective envelope of Jupiter [Showman et al., 2011]. The relevant length scale would be

$$l \sim w/\Omega \sim (\frac{\alpha g F}{\rho c_p \Omega^3})^{1/2} \tag{3.10}$$

instead of a pressure scale height. Therefore, we can formulate a new scaling for the eddy diffusion coefficient using the velocity and length scale described here. The eddy diffusion coefficient would be

$$K_{\mathrm{eddy}} \sim wl \sim \frac{\alpha g F}{\rho c_p \Omega^2}. \tag{3.11}$$

Here we neglected all the prefactors in the scalings, however, these prefactors can be determined from laboratory measurements.

3.2.2 Scalings from Rotating Tank Experiments

A set of scalings for integral length scale and convective (r.m.s.) velocity was proposed and validated by rotating tank experiments. The laboratory experiments [e.g., Boubnov and Golitsyn, 1986, 1990, Fernando et al., 1991, Maxworthy and Narimousa, 1994, Coates and Ivey, 1997] are done in a rotating tank filled

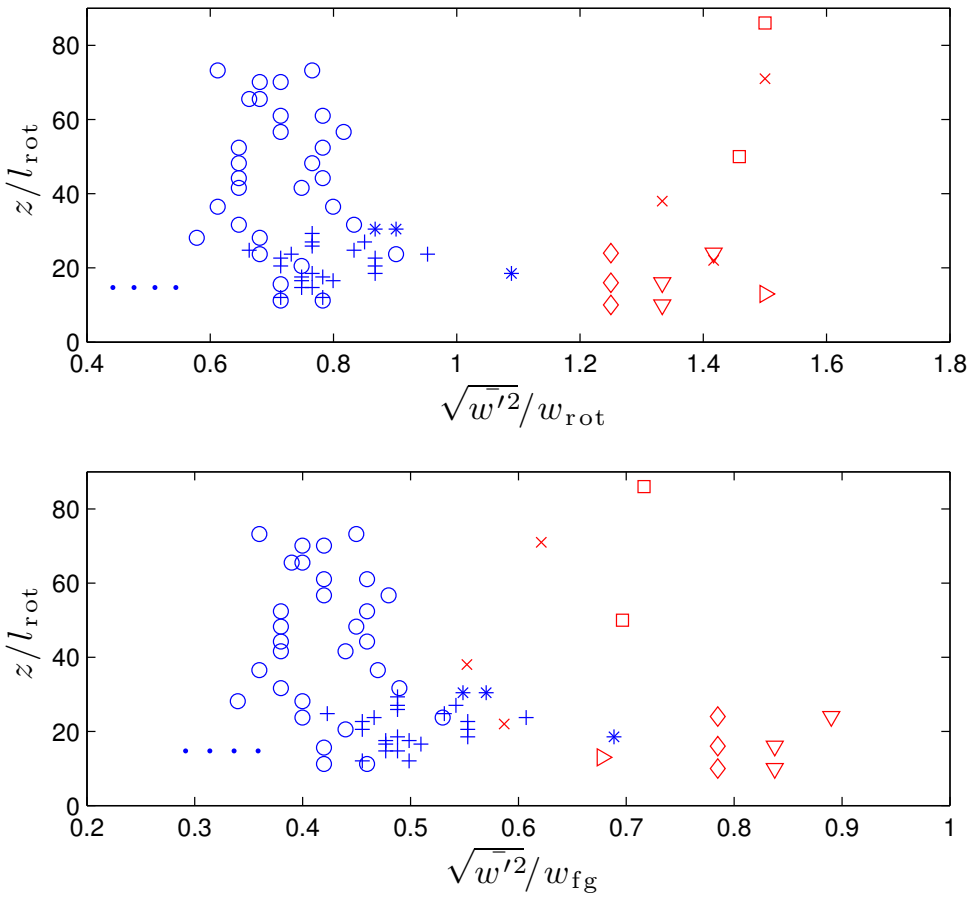

Figure 3.1 Normalization of vertical r.m.s. velocity $\sqrt{\overline{w'^2}}$ by $w_{\rm rot}$ and $w_{\rm fg}$, respectively. Vertical axis represents the height z (relative to the bottom of the tank) where $\sqrt{\overline{w'^2}}$ is measured. The data colored in red are extracted from Fig 16 in Fernando et al. [1991] and the data colored in blue are extracted from Fig 6 in Coates and Ivey [1997]. Different marker types correspond to different sets of experiments, with different rotation rates and prescribed heat fluxes. We only plot data with $z/l_{\rm rot} > 30$ ($Ro^\star < 0.03$), because that is where we expect rotating scaling applies. The data points should fall along a vertical line if the scaling could represent $\sqrt{\overline{w'^2}}$ well.

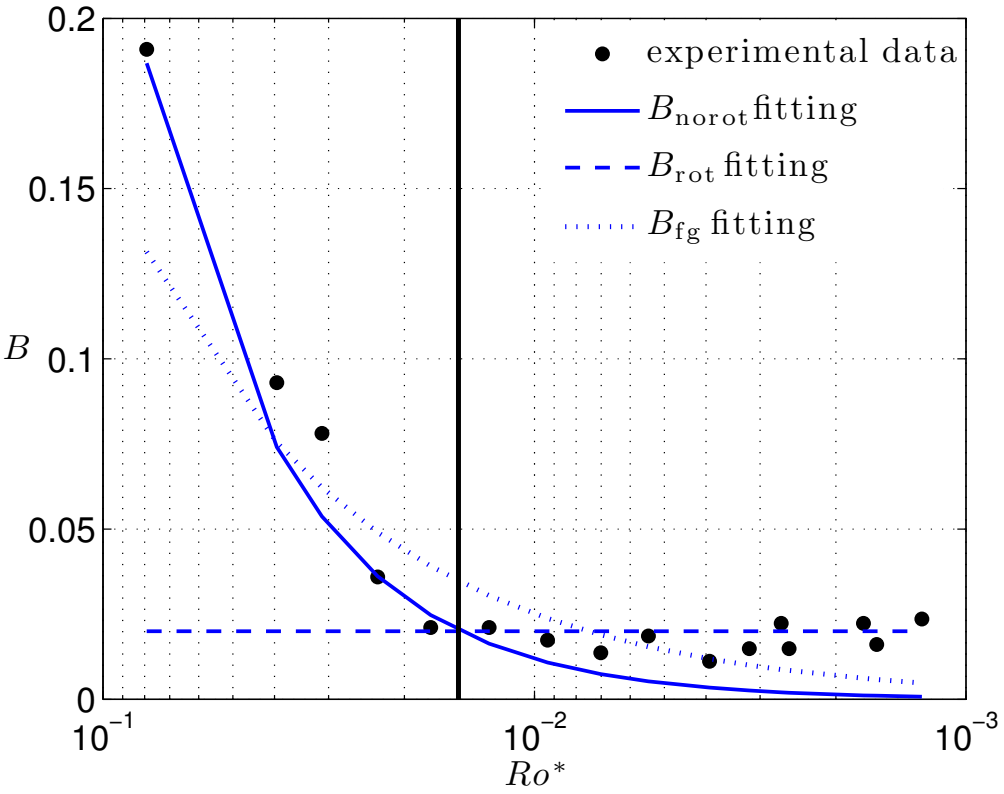

Figure 3.2 Scatterplot of B as a function of $Ro^\star$. $B = (\alpha g d\bar{T}/dz)/(\Omega^2)$, and $Ro^\star = l_{\rm rot}/h$. This figure is based on Fig 8 in Levy and Fernando [2002]. Black filled circles represent experimental data extracted from Fig 8 in Levy and Fernando [2002]. Solid curve is the fit using $B_{\rm norot}$ defined by equation (3.20), dashed line is the fit using $B_{\rm rot}$ defined by equation (3.17), and dotted curve is the fit using $B_{\rm fg}$ given by equation (3.19). The vertical line is showing the transition from high $Ro^\star$ regime to low $Ro^\star$ regime, corresponding to $Ro^\star_t$ = 0.015.

with water while the tank can have rotation with respect to its vertical axis. The bottom of the tank is heated in order to generate thermal convection, while the upper surface is open. Flow speed and temperature are directly measured. It is observed that two physically distinct regimes are identified, depending on rotation rate: (1) fully developed turbulence when the rotation rate is small, and (2) geostrophic turbulence when the rotation rate is large. Two sets of scalings for convective velocity w and integral length scale l are also proposed for these two regimes, respectively. For fully developed turbulence, the convective velocity and integral length scale are [e.g. Adrian et al., 1986, Deardorff, 1972, Fernando et al., 1991]

$$w_{\mathrm{norot}} = \alpha(\frac{\alpha g F}{\rho c_p} l)^{1/3}, l_{\mathrm{norot}} = h, \tag{3.12}$$

where h is the height of the fluid in the tank. This expression offers experimental support for the estimation by Stone [1976], but only applies to fully developed turbulence with weak rotational effects. The coefficient $\alpha \approx 0.6$ is determined from experimental measurements [Adrian et al., 1986, Fernando et al., 1991]. A different scaling, for geostrophic turbulence [Fernando et al., 1991, Maxworthy and Narimousa, 1994, Coates and Ivey, 1997, Fernando and Smith Iv, 2001, Levy and Fernando, 2002], is given by

$$w_{\mathrm{rot}} = \beta_1(\frac{\alpha g F}{\rho c_p \Omega})^{1/2}, l_{\mathrm{rot}} = \beta_2(\frac{\alpha g F}{\rho c_p \Omega^3})^{1/2}, \tag{3.13}$$

where $\beta_1 = 1.2 \pm 0.6$ [Fernando et al., 1991, Maxworthy and Narimousa, 1994, Coates and Ivey, 1997], and $\beta_2 \approx 1.1$ [Fernando et al., 1991].

The transition between fully developed turbulence and geostrophic turbulence is governed by a natural Rossby number [e.g. Maxworthy and Narimousa, 1994, Jones and Marshall, 1993], defined as

$$Ro^\star = l_{\mathrm{rot}}/h = (\frac{\alpha g F}{\rho c_p \Omega^3})^{1/2} \frac{1}{h}. \tag{3.14}$$

There exists a transitional natural Rossby number $Ro_t^\star$. When $Ro^\star < Ro_t^\star$, turbulent convection is strongly inhibited by rotation, integral length scale is smaller than mixed layer height, and rotating scaling (equation 3.13) applies; when $Ro^\star > Ro_t^\star$, turbulent convection is weakly affected by rotation, thus non-rotating scaling applies (equation 3.12). Based on velocity data, Coates and Ivey [1997] found $0.057 \leq Ro_t^\star \leq 0.14$, and Cui and Street [2001] found $0.042 \leq Ro_t^\star \leq 0.12$.

One directly measurable quantity from these rotating tank experiments is the flow velocity. In Fig. 3.1, we normalize the measured r.m.s. vertical velocity $\sqrt{\overline{w'^2}}$ using $w_{\rm rot}$ and another velocity scaling

$$w_{\rm fg} \sim (\frac{\alpha g F}{\rho c_p})^{2/5} (\frac{h}{2\Omega})^{1/5}, \tag{3.15}$$

which is that derived by Flasar and Gierasch [1978]. If the scalings $w_{\rm rot}$ or $w_{\rm fg}$ can represent the vertical r.m.s. velocity $\sqrt{\overline{w'^2}}$, we would expect $\sqrt{\overline{w'^2}}/w_{\rm rot}$ or $\sqrt{\overline{w'^2}}/w_{\rm fg}$ to be a constant. We use two experimental datasets for $\sqrt{\overline{w'^2}}$. One is from Fernando et al. [1991], and the other is from Coates and Ivey [1997]. In the figure, the dataset from Fernando et al. [1991] is indicated by blue markers, and the dataset from Coates and Ivey [1997] us indicated by red markers. In the upper plot of Fig. 3.1, data points are normalized by $w_{\rm rot}$. Both datasets are aligned at values that are similar but not identical. This indicates slightly different prefactors before the scaling. We believe the difference is due to systematic error in measuring flow speed. In the lower plot, blue markers are well clustered, but red markers are subject to large scatter. Therefore, data from Fernando et al. [1991] are not well fitted by $w_{\rm fg}$. Overall, $w_{\rm rot}$ looks better in fitting experimental datasets than $w_{\rm fg}$, but the difference is not very significant.

Another measurable quantity is the vertical temperature gradient (e.g. $d\bar{T}/dz$). Vertical temperature gradient in non-rotating turbulent convection is

almost negligible because vertical mixing is very strong and the fluid is very well mixed. However, in rotating fluid, because of the inhibition of vertical mixing by rotation, there are much larger temperature gradients. Now we define a dimensionless quantity B to normalize $d\bar{T}/dz$, and its definition is

$$B = -\frac{\alpha g d\bar{T}/dz}{\Omega^2}. \tag{3.16}$$

We derive the scalings for B based on scalings for w and l. For rapid rotation, $K_{\mathrm{eddy,rot}} = C_{\mathrm{rot}}^{-1} w_{\mathrm{rot}} l_{\mathrm{rot}}$, where C_{rot} is a constant, and C_{rot}^{-1} represents the correlation between w_{rot} and l_{rot}. Using equation (3.13) and (3.16), we find B_{rot} can be expressed as

$$B_{\mathrm{rot}} = \frac{\alpha g F}{\rho c_p K_{\mathrm{eddy,rot}} \Omega^2} = C_{\mathrm{rot}}. \tag{3.17}$$

Another set of scalings (e.g., equation 3.7 & 3.8) for rapid rotating convection is from Flasar and Gierasch [1978]. The corresponding scaling for the eddy diffusion coefficient is

$$K_{\mathrm{eddy,fg}} = C_{\mathrm{fg}}^{-1} (\frac{\alpha g F}{\rho c_p})^{3/5} (\frac{h}{\Omega})^{4/5}, \tag{3.18}$$

where C_{fg} is a constant. Therefore, B_{fg} can be expressed as

$$B_{\mathrm{fg}} = \frac{\alpha g F}{\rho c_p K_{\mathrm{eddy,fg}} \Omega^2} = C_{\mathrm{fg}} Ro^{\star 4/5}. \tag{3.19}$$

Recall that $Ro^\star$ is the natural Rossby number defined by equation (3.14). For slow rotation, using scalings from equation (3.12), we find

$$B_{\mathrm{norot}} = C_{\mathrm{norot}} Ro^{\star 4/3}. \tag{3.20}$$

Both B & $Ro^\star$ are measurable quantities in the experiments, therefore, datasets of ($Ro^\star$, B) are able to provide a test to the scalings derived above. In Fig 3.2, we made a scatterplot of ($Ro^\star$, B) measured from experiments [Levy and Fernando, 2002]. The scalings B_{rot}, B_{norot} and B_{fg} as a function of $Ro^\star$ are overplotted on the same figure. Inspection of the fitting in Fig. 3.2 reveals that B_{rot} is clearly better

Table 3.1 Calculated $K_{\rm eddy}$ (cm^2 s^{-1}) at T = 1000 K (near the CO quench level)[a]

ϕ	0°	9°[b]	30°	60°	90°
$K_{\rm eddy}$ (Jupiter)	(1.2±0.2)×10^8	(1.2±0.2)×10^8	(5.0±1.1)×10^7	(1.7±0.4)×10^7	(1.3±0.3)×10^7
$K_{\rm eddy}$ (Saturn)	(1.9±0.2)×10^8	(5.6±1.1)×10^7	(5.5±1.1)×10^6	(1.8±0.4)×10^6	(1.4±0.3)×10^6

[a]The uncertainty includes uncertainties on the formulation itself and on the internal heat flux F.
[b]This is the latitude where tropospheric CO is measured on Jupiter [Bézard et al., 2002].

in fitting data than $B_{\rm fg}$ for small $Ro^\star$ values, and $B_{\rm norot}$ can fit data well at large $Ro^\star$ values. In summary, the experimental data supported the scalings (3.12), (3.13), (3.17), & (3.20). The pre-factors are determined to be $C_{\rm norot} = 5.5 \pm 0.5$ and $C_{\rm rot} = 0.020 \pm 0.005$ [Levy and Fernando, 2002].

Now that we have experimentally validated formulations for B or equivalently, $d\bar{T}/dz$, we determine the pre-factors in the scalings for $K_{\rm eddy}$:

$$K_{\rm eddy} = \frac{\alpha g F}{\rho c_p B_{\rm norot} \Omega^2} = (0.18 \pm 0.02)(\frac{\alpha g F}{\rho c_p})^{1/3} h^{4/3}, \text{ for } Ro^\star > Ro_t^\star; \qquad (3.21)$$

$$K_{\rm eddy} = \frac{\alpha g F}{\rho c_p B_{\rm rot} \Omega^2} = (50 \pm 10)\frac{\alpha g F}{\rho c_p \Omega^2}, \text{ for } Ro^\star < Ro_t^\star. \qquad (3.22)$$

$Ro_t^\star$ is identified in Fig 3.2 by locating the transition from $B_{\rm norot}$ scaling to $B_{\rm rot}$ scaling. $Ro_t^\star$ is found to be 0.015 with an uncertainty of 20% [Levy and Fernando, 2002]. This value is consistent with estimations by Coates and Ivey [1997] and Cui and Street [2001] using velocity data. In the following sections, we will use $Ro_t^\star$ = 0.015.

3.2.3 Eddy Diffusion Coefficient in the Atmosphere of Jupiter and Saturn

Now we have the scalings for $K_{\rm eddy}$ given by equation (3.21) & (3.22). An extrapolation is needed to apply this scaling to the atmospheres of giant planets

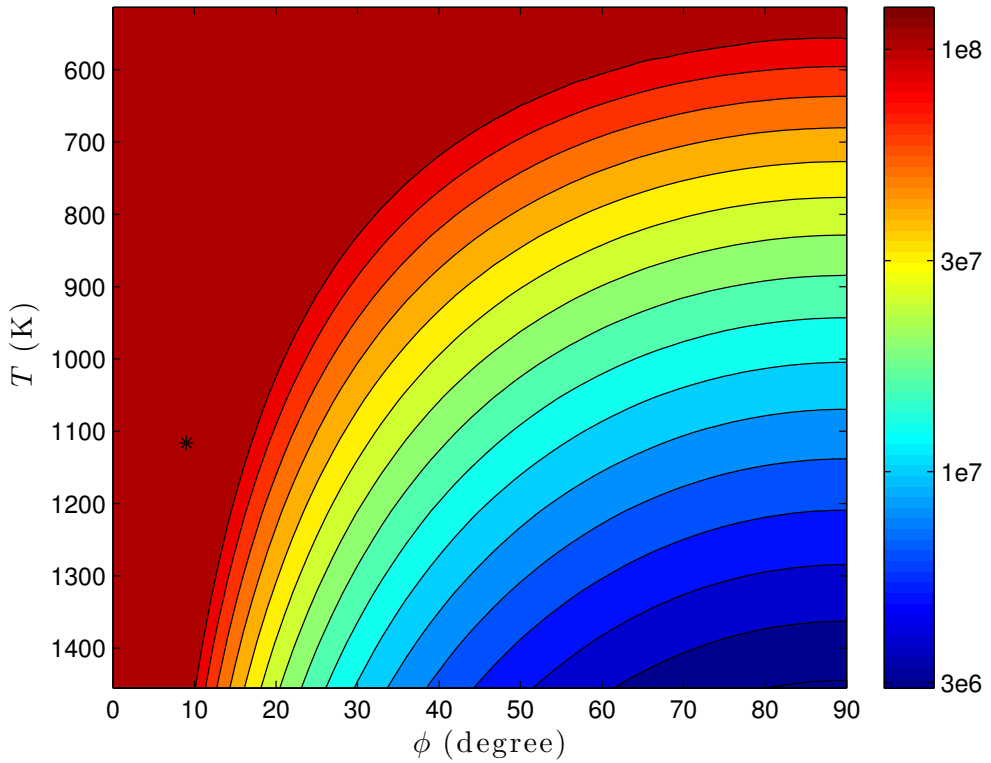

Figure 3.3 Profile of $K_{\rm eddy}$ (cm^2 s^{-1}) as a function of temperature T (K) and latitude ϕ (degrees) for Jupiter. On the figure, we denote the location of CO quench level at 9° N where a measurement of its mixing ratio is available [Bézard et al., 2002]. Our estimation gives $K_{\rm eddy} = (1.2 \pm 0.2) \times 10^8$ cm^2 s^{-1} at this location.

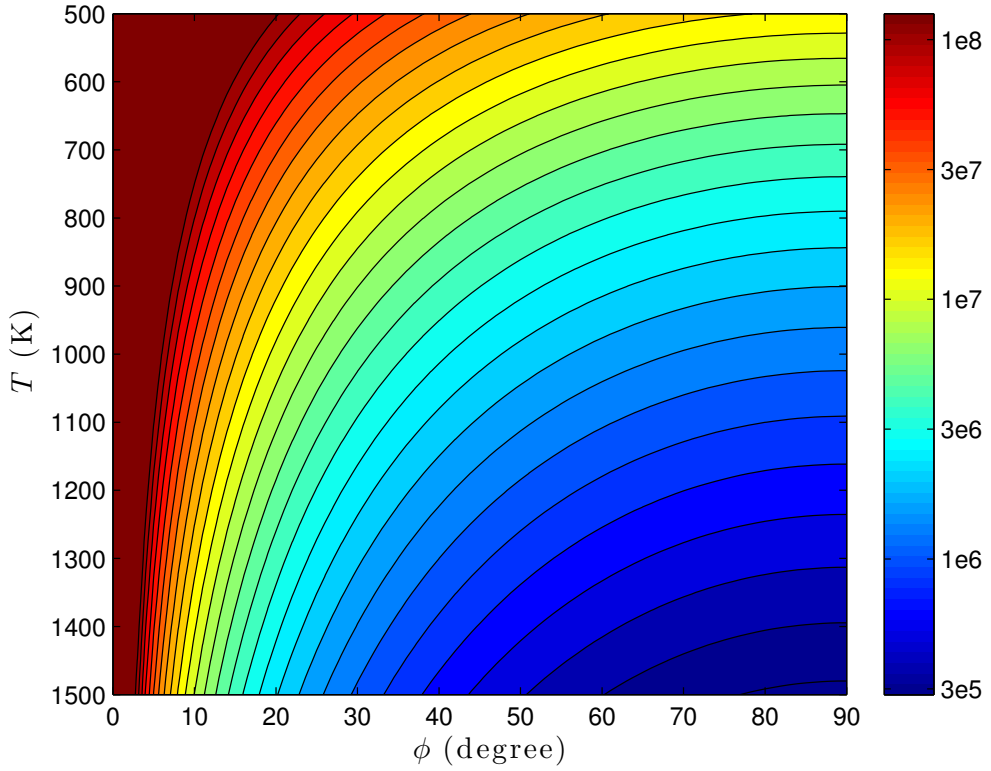

Figure 3.4 Profile of $K_{\rm eddy}$ (cm^2 s^{-1}) as a function of temperature T (K) and latitude ϕ (degrees) for Saturn.

because the flux Rayleigh number Ra_f in the experiments cannot reach as high as that in giant planets. The flux Rayleigh number is defined as $Ra_f = \frac{\alpha g F H^4}{\rho c_p \kappa^2 \nu}$, where κ is the thermal diffusivity and ν is molecular viscosity. It is defined as equivalent to the Rayleigh number $Ra = \frac{\alpha g dT/dz H^4}{\kappa\nu}$, but more straightforward than Ra because the quantity F is usually available rather than dT/dz in astrophysical bodies. For Jupiter, Ra_f is estimated to be about 10^{30} near $T = 1000K$ using the thermal properties calculated in French et al. [2012]. In the experiments, $Ra_f = 10^{12} \sim 10^{13}$. Therefore, applying the experimentally derived scaling to Jupiter's atmosphere is an extrapolation, but it is likely that the extrapolation is reasonable for the following reasons. (1) It is generally believed that at very high Ra_f, molecular viscosity and diffusivity will not affect the property of turbulent transport. This happens when Ra_f is much larger than the critical flux Rayleigh number $Ra_{f,c}$. From Fig. 4 in Fernando and Smith Iv [2001], the Ra_f implied in the experimental setup is at least three order of magnitude higher than the $Ra_{f,c}$, and most of them are four or five order of magnitude higher. Therefore, it is reasonable to assume the scalings are independent of molecular viscosities and diffusivities. (2) Non-rotating scaling (equation 3.21) is the same as the prediction by mixing length theory, which is another piece of evidence that the experiments have probed the highest Ra_f regime.

The experiments are set up in a plane parallel geometry and the rotation axis is aligned with the gravity, while Jupiter has a spherical geometry and locally the gravity and rotation vector is misaligned except at the pole. However, under some approximations, the experimental results are applicable to Jupiter's atmosphere as well. First, the vertical length scale ($\sim H$) is much smaller than the horizontal length scale ($\sim R_{\rm Jup}$), thus the curvature of the geometry is not important here. Second, since we assume heat is primarily transported by ed-

dies, whose scale in the atmosphere is much smaller than planetary radii, f-approximation can be made in the governing Navier Stokes equations, and the dynamics thus only depend on the Coriolis parameter $f = 2\Omega sin\phi$, where ϕ is the latitude. Therefore, the scalings applicable to all latitudes can be derived by replacing Ω with $\Omega sin\phi$ in the equations (3.14), (3.21) & (3.22). A transitional latitude ϕ_t exists, and can be related to $Ro_t^\star$ by

$$sin\phi_t = (\frac{\alpha g F}{\rho c_p H^2 Ro_t^{\star 2}})^{1/3} \frac{1}{\Omega}, \tag{3.23}$$

$K_{\rm eddy}$ in the atmosphere thus can be written based on scalings given by equation (3.21) & (3.22):

$$K_{\rm eddy} = (0.18 \pm 0.02)(\frac{\alpha g F}{\rho c_p})^{1/3} H^{4/3}, \text{ for } \phi < \phi_t, \tag{3.24}$$

$$K_{\rm eddy} = (50 \pm 10)\frac{\alpha g F}{\rho c_p (\Omega sin\phi)^2}, \text{ for } \phi > \phi_t, \tag{3.25}$$

while ϕ_t can be determined locally based on equation (3.23) with $Ro_t^\star$ = 0.015. Clearly ϕ_t is a function of altitude. At the level where T $\sim$ 1000 K (near the quench level), we find $\phi_t = 19^\circ$ for Jupiter, and $\phi_t = 5^\circ$ for Saturn.

The adiabatic profile for Jupiter and Saturn are calculated stepwise following the method described in Fegley and Prinn [1985]. For Jupiter, we use T = 427.71 K at P = 22 bars as our reference point [Seiff et al., 1998]. The compositions considered is $X_{\rm H_2}$ = 0.864 and $X_{\rm He}$ = 0.136 [Niemann et al., 1998]. For Saturn, we use T = 134.8 K at P = 1 bar [Lindal et al., 1985] as our reference point, and the composition considered are $X_{\rm H_2}$ = 0.881 and $X_{\rm He}$ = 0.119 [Conrath and Gautier, 2000]. Strictly speaking, a wet adiabat would be more appropriate within the water cloud. However, since the quench level is around 400 bars, the wet adiabat is only a small portion of the extrapolated regions. Although we expect

the use of a wet adiabat would yield a more accurate adiabatic profile, the difference from our calculated dry adiabat would be small. Along the calculated adiabatic profile, we calculate quantities such as α, ρ, and pressure scale height H using the ideal gas law since the part of atmosphere we considered is close to ideal gas. The internal heat flux for Jupiter is estimated to be 5.444 $\pm$ 0.425 W m^{-2} [Hanel et al., 1981], and for Saturn it is estimated to be 2.01 $\pm$ 0.14 W m^{-2} [Hanel et al., 1983].

Using equations (3.24) and (3.25), we calculate $K_{\rm eddy}$ as a function of temperature T (radial direction) and latitude ϕ for both Jupiter and Saturn. The profile of $K_{\rm eddy}$ is shown in Fig 3.3 for Jupiter and Fig 3.4 for Saturn. A latitudinal dependence is clear, showing higher $K_{\rm eddy}$ near the equator where $\phi < \phi_t(T)$, and smaller $K_{\rm eddy}$ at higher latitudes where $\phi > \phi_t(T)$. The difference between equator and pole could be as large as one to two orders of magnitude. In Table 1, we compare the calculated $K_{\rm eddy}$ at a temperature level $T \sim 1000$ K (near the quench level) between Jupiter and Saturn. The values of $K_{\rm eddy}$ include uncertainties on the formulation itself and on the measured internal heat flux F. Near the equator, $K_{\rm eddy}$ is about 1×10^8 cm^2 s^{-1} for both planets. For Jupiter, $K_{\rm eddy}$ decreases to about 1×10^7 cm^2 s^{-1} at $\phi \sim 90^\circ$. For Saturn, $K_{\rm eddy}$ decreases to about 1×10^6 cm^2 s^{-1} at $\phi \sim 90^\circ$.

This latitudinal dependence of $K_{\rm eddy}$ is also shown in Flasar and Gierasch [1977] and Fig 1 in Visscher et al. [2010]. Both are based on the scalings given by equation (3.7) [Flasar and Gierasch, 1978]. In section 2.2, we have shown that experimental results do not favor this scaling. In addition, previous studies are not able to determine the transition latitude ϕ_t, and thus not able to calculate $K_{\rm eddy}$ for all latitudes.

In summary, our new formulation of $K_{\rm eddy}$ is validated against experiments, thus providing a new perspective compared with previous theoretical investigations. Also, the pre-factors in the scalings are well determined by the experimental data, which enables us to constrain $K_{\rm eddy}$ much better than before.

3.3 Deep Water Abundance Constrained by CO Thermochemistry Kinetics

In this section, we update constraints on the deep water abundance of Jupiter and Saturn from CO using the newly constrained $K_{\rm eddy}$ in this paper. We used the rate limiting step proposed in Visscher and Moses [2011], but we also considered a new CO kinetic model proposed in Venot et al. [2012], which has been applied to extrasolar planets' atmospheric chemistry [Venot et al., 2012] and Uranus atmospheric chemistry [Cavalié et al., 2014], but never before to Jupiter. We will show that these two kinetic models predict very different constraints on the deep water abundance.

We make a few definitions regarding the abundance of species Z. The concentration of species Z is denoted as [Z] with a unit of molecules cm^{-3}. Mole fraction of Z is denoted as $X_{\rm Z}$ = [Z]/n, where n is number density of the atmosphere (molecule cm^{-3}). Mixing ratio is denoted as $q_{\rm Z}$ = [Z]/[H_2]. The enrichment relative to solar is $E_{\rm Z}$ = $q_{\rm Z,planet}/q_{\rm Z,solar}$, where $q_{\rm Z,solar}$ is the mixing ratio of species Z in the Sun's atmosphere, taken from Asplund et al. [2009].

3.3.1 Constraints Using the Rate Limiting Step from Visscher and Moses [2011]

We use a timescale approach, instead of solving the diffusion-kinetics equations explicitly. The timescale approach has been used extensively in previous studies to model the abundance of disequilibrium species, and it has been shown in Visscher et al. [2010] to be able to produce fairly accurate results. The error of the time-scale approach relative to the full diffusion-kinetics modeling in their particular example was $\sim 20\%$. Since the relative error is acceptable in constraining Jupiter's deep water abundance, we choose to use the time-scale approach. Here is how we implement this approach. (1) We determine the chemical timescale $\tau_{\rm chem}$ along the adiabat; (2) we determine the mixing timescale $\tau_{\rm mix}$ along the adiabat using the newly constrained $K_{\rm eddy}$; (3) we equate $\tau_{\rm chem}$ and $\tau_{\rm mix}$ in order to find the quench level, and calculate the abundance of CO at the quench level. CO above quench level is vertically well mixed, so we can get the abundance of CO at a few bars as a function of $K_{\rm eddy}$ and the water abundance. Therefore, constraints can be put on the water abundance. Here we detail our implementation of this method to Jupiter's and Saturn's atmospheres using the rate limiting step from Visscher and Moses [2011].

- *Chemical timescale* $\tau_{\rm chem}$

  We estimate $\tau_{\rm chem}$ using the rate limiting step proposed in Visscher and Moses [2011]:

  $$\mathrm{CH_3OH + M \leftrightarrow CH_3 + OH + M}, \tag{3.26}$$

  where M represents any third body. The rate coefficients $\mathrm{k}_{3.26}$ for reaction (3.26) is calculated using the modified Tore parameters in the Appendix of

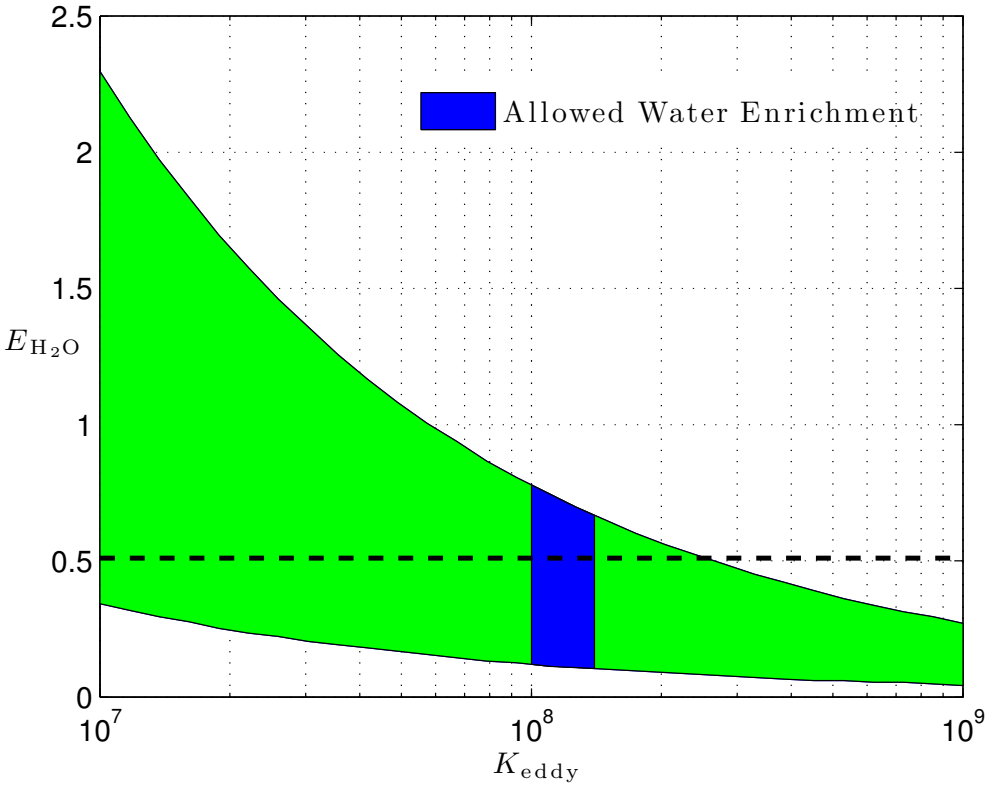

Figure 3.5 Chemical constraints on Jupiter's deep water abundance using rate limiting step from Visscher and Moses [2011]. The green area between two curves indicates the allowed $E_{\mathrm{H_2O}}$ considering a factor of five uncertainty in rate coefficient of rate limiting step [Jasper et al., 2007, Visscher and Moses, 2011] and $X_{\mathrm{CO}} = (1.0 \pm 0.2) \times 10^{-9}$ [Bézard et al., 2002]. Using $K_{\mathrm{eddy}} = (1.2 \pm 0.2) \times 10^8$ cm^2 s^{-1} constrained at the location of measurement, we find $E_{\mathrm{H_2O}} = 0.1 \sim 0.75$, corresponding to the blue area in the figure. Dashed line indicates $E_{\mathrm{H_2O}}$ measured by Galileo Entry Probe [Wong et al., 2004].

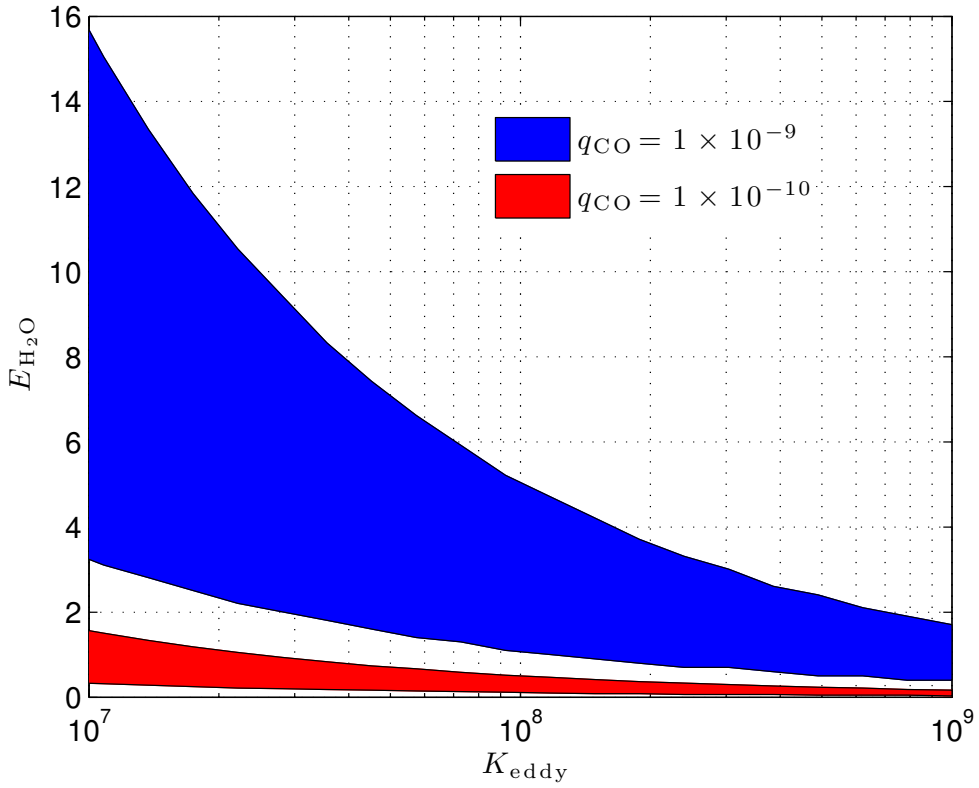

Figure 3.6 Chemical constraints on Saturn's deep water abundance using the the rate limiting step from Visscher and Moses [2011]. We consider two hypothetical tropospheric CO mixing ratio, namely, $q_{\mathrm{CO}} = 1 \times 10^{-9}$ and $q_{\mathrm{CO}} = 1 \times 10^{-10}$. The uncertainty indicated by shaded area is due to the factor of five uncertainty in the rate coefficient of the rate limiting step [Jasper et al., 2007, Visscher and Moses, 2011]. We did not impose a constraint on K_{eddy} since it sensitively depends on the latitude where CO measurement is taken.

Jasper et al. [2007] (Typos in the appendix of that paper were corrected in author's website $\underline{http://www.sandia.gov/\ ajasper/pub/}$).

The chemical timescale $\tau_{\rm chem}$ can be expressed as

$$\tau_{\rm chem}({\rm CO}) = \frac{X_{\rm CO}}{dX_{\rm CO}/dt} = \frac{X_{\rm CO}}{k_{3.26}X_{\rm CH_3OH}n}. \tag{3.27}$$

In order to eliminate $X_{\rm CH_3OH}$ in equation (3.27), assuming an equilibrium state between CH_3OH and CO:

$$\rm CH_3OH = CO + 2H_2, \tag{3.28}$$

equation (3.27) can be rewritten as

$$\tau_{\rm chem}({\rm CO}) = \frac{1}{k_{3.26}K_{3.28,\rm eq}X_{\rm H_2}^2 p^2 n}, \tag{3.29}$$

where the equilibrium constant $K_{3.28,\rm eq}$ is

$$K_{3.28,\rm eq} = \exp\left[-\frac{\Delta_f G_{\rm CH3OH} - \Delta_f G_{\rm CO}}{RT}\right]. \tag{3.30}$$

The Gibbs free energy of formation $\Delta_f G_{\rm CO}$ is from NIST-JANAF Thermochemical Table [Chase, 1998], and $\Delta_f G_{\rm CH_3OH}$ is from CRC HandBook of Chemistry and Physics [Handbook, 2012].

- *Mixing timescale* $\tau_{\rm mix}$

  The vertical mixing timescale can be expressed as

  $$\tau_{\rm mix} = \frac{L_{\rm eff}^2}{K_{\rm eddy}}, \tag{3.31}$$

  where $L_{\rm eff}$ is an effective length scale. It can be calculated following the recipe described in Smith [1998], and we find near the CO quench level, $L_{\rm eff} \approx 0.12H$ for Jupiter, and $L_{\rm eff} \approx 0.14H$ for Saturn.

- $X_{\rm CO}$ *at quench level*

We calculated $\tau_{\rm chem}$ and $\tau_{\rm mix}$ along Jupiter or Saturn's adiabat. The quench level was found by equating $\tau_{\rm chem}$ and $\tau_{\rm mix}$. The quench level depends on $K_{\rm eddy}$ and the reaction rate of the rate limiting step. For $K_{\rm eddy}$ = 1×10^8 cm^2 s^{-1}, the quench temperatures for Jupiter and Saturn are about 1100 K and 1020 K, respectively. Once the quench level is determined, we can adjust the abundance of H_2O at the quench level to a value consistent with the observed CO abundance.

The equilibrium abundance of CO is governed by the net reaction [e.g., Fegley and Prinn, 1985, 1988, Lodders and Fegley, 2002, Visscher and Fegley, 2005]

$$\mathrm{CO} + 3\mathrm{H_2} = \mathrm{CH_4} + \mathrm{H_2O}. \tag{3.32}$$

Using equilibrium constant $K_{3.32,\rm eq}$ of this reaction, the equilibrium abundance of CO can be expressed as

$$X_{\rm CO} = \frac{K_{3.32,eq} X_{\rm CH_4} X_{\rm H2O}}{X_{\rm H_2}^3 p^2}, \tag{3.33}$$

where p is the atmospheric pressure in the unit of bars. On Jupiter, the mole fractions of H_2 and CH_4 were measured by Galileo Probe Mass Spectrometer (GPMS), with a value of $X_{\rm H_2}$ = 0.864 $\pm$ 0.003 [Niemann et al., 1998], and $X_{\rm CH_4}$ = (2.05 $\pm$ 0.32) $\times$ 10^{-3} [Wong et al., 2004]. For Saturn, CH_4 is measured by Cassini CIRS with a mixing ratio $q_{\rm CH_4}$ = (5.3$\pm$0.2)×10^{-3} [Flasar et al., 2005, Fletcher et al., 2009a].

The equilibrium constant $K_{3.32,\rm eq}$ can be calculated as

$$K_{3.32,\rm eq} = \exp\left[-\frac{\Delta_f G_{\rm CO} - \Delta_f G_{\rm CH_4} - \Delta_f G_{\rm H_2O}}{RT}\right], \tag{3.34}$$

where R = 8.314 J mol^{-1} K^{-1} is the universal gas constant, and $\Delta_f G_{\rm CO}$, $\Delta_f G_{\rm CH_4}$, $\Delta_f G_{\rm H_2O}$ are Gibbs free energy of formation for CO, $\mathrm{CH_4}$, and $\mathrm{H_2O}$,

respectively. We took these values from NIST-JANAF Thermochemical Tables [Chase, 1998].

- *Constraints on $X_{\mathrm{H_2O}}$ for Jupiter and Saturn*

  Now that we can calculate X_{CO} as a function of K_{eddy} and $X_{\mathrm{H_2O}}$ using the time-scale approach, given the observed CO abundance in the troposphere, we can place constraints on $X_{\mathrm{H_2O}}$.

  On Jupiter, the tropospheric CO was measured by Bézard et al. [2002] near one of the hot spots at 9° N. X_{CO} was estimated to be (1.0 $\pm$ 0.2)$\times 10^{-9}$ at the 6 bar level. In Figure 3.5, we plot the allowed $E_{\mathrm{H_2O}}$ (enrichment relative to solar q_{O} = 9.8$\times 10^{-4}$ from Asplund et al. [2009]) as a function of K_{eddy}. We consider a factor of five uncertainty in the rate limiting step. Near 9° N, $K_{\mathrm{eddy}} = (1.2 \pm 0.2) \times 10^8$ cm^2 s^{-1} is found according to Table 1. Applying this constraint on K_{eddy}, we find $E_{\mathrm{H_2O}}$ = 0.1 $\sim$ 0.75. This constraint is consistent with the Galileo measurement of $E_{\mathrm{H_2O}}$ = 0.50 $\pm$ 0.16 [Wong et al., 2004].

  On Saturn, CO is observed at a mole fraction of (1.5$\pm$0.8)$\times 10^{-9}$ [Noll et al., 1986, Noll and Larson, 1991]. However, the fraction coming from an internal source (vertical mixing) is still unknown. Cavalié et al. [2009] put an upper limit on the amount of CO from an internal source with $q_{\mathrm{CO}} < 1 \times 10^{-9}$, however, no lower limit is obtained yet. Here we keep tropospheric CO abundance as a free parameter and explore two cases, namely, q_{CO} = 1.0$\times 10^{-9}$ and q_{CO} = 1.0$\times 10^{-10}$. The constraints on the deep water abundance are shown in Fig 3.6. Once the tropospheric CO is measured in the future, we can refer to Fig 3.4 or Table 3.1 to find out the corresponding K_{eddy} at the observation location, then refer to Fig. 6 to find out the constraints on Saturn's $X_{\mathrm{H_2O}}$.

3.3.2 Constraints Using Kinetic Model from Venot et al. [2012]

Table 3.2 Comparison between timescale approach and full diffusion-kinetic modeling using the *Venot model*.

($K_{\rm eddy}$, $E_{\rm H_2O}$)[a]	$X_{\rm CO}$ from approximation method	$X_{\rm CO}$ from full diffusion-kinetic modeling
Jupiter		
(1×10^7, 20)	7.6×10^{-10}	7.5×10^{-10}
(1×10^8, 10)	1.5×10^{-9}	1.5×10^{-9}
(1×10^9, 1.0)	6.0×10^{-10}	5.7×10^{-10}
Saturn		
(1×10^7, 20)	7×10^{-11}	6.8×10^{-11}
(1×10^8, 10)	1.5×10^{-10}	1.6×10^{-10}
(1×10^9, 1.0)	6.0×10^{-11}	6.5×10^{-11}

[a]The unit of $K_{\rm eddy}$ is cm^2 s^{-1}

Venot et al. [2012] proposed a carbon-nitrogen kinetic model and applied it to study hot Jupiter atmospheres. The kinetic model was originally developed for modeling combustion process in car engines and has been validated at a range of temperatures from 300 K to 2500 K, and pressure from 0.01 bar to some hundred bars. Considering the relevant range of temperature and pressure, this kinetic model is appropriate to study Jupiter and Saturn's disequilibrium chemistry as well. It would be useful to compare the implied $X_{\rm H_2O}$ from Visscher and Moses [2011]'s kinetic model (*VM model*) and Venot et al. [2012]'s kinetic model (*Venot model*) . To our knowledge, this comparison has never been done for Jupiter and Saturn.

Since no rate limiting step has been identified from *Venot model*, the chemical timescale cannot be explicitly calculated. Therefore, we developed a full diffusion-kinetic model, incorporating the whole kinetic network from Venot et al. [2012]. Our model is similar to the model developed in Venot et al. [2012], but with application to Jupiter's and Saturn's atmospheres. For each species i, we solve the diffusion-kinetic equation

$$\frac{\partial n_i}{\partial t} + \frac{\partial \phi_i}{\partial z} = S_i, \tag{3.35}$$

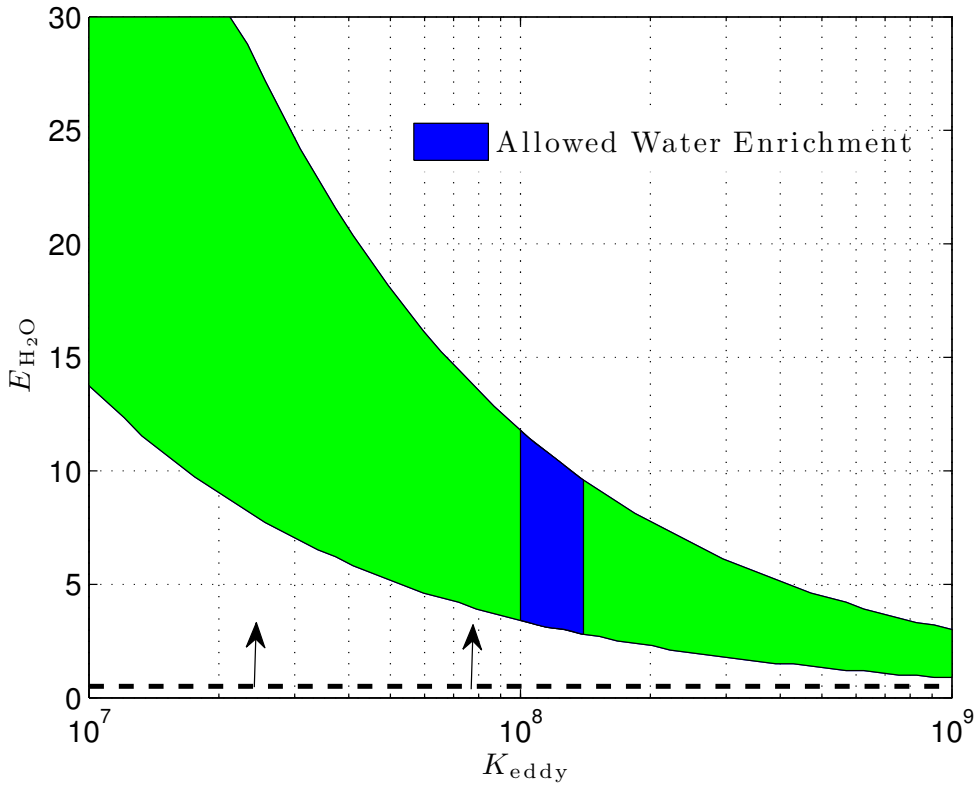

Figure 3.7 Chemical constraints on Jupiter's deep water abundance using the CO kinetic model from Venot et al. [2012]. The green area indicates allowed $E_{\mathrm{H_2O}}$ considering a factor of two uncertainty in the rate coefficient and $X_{\mathrm{CO}} = (1.0 \pm 0.2) \times 10^{-9}$ Bézard et al. [2002]. Using $K_{\mathrm{eddy}} = (1.2 \pm 0.2) \times 10^8$ near 9° N, we find $E_{\mathrm{H_2O}} = 3 \sim 11$, corresponding to the blue area in the figure.

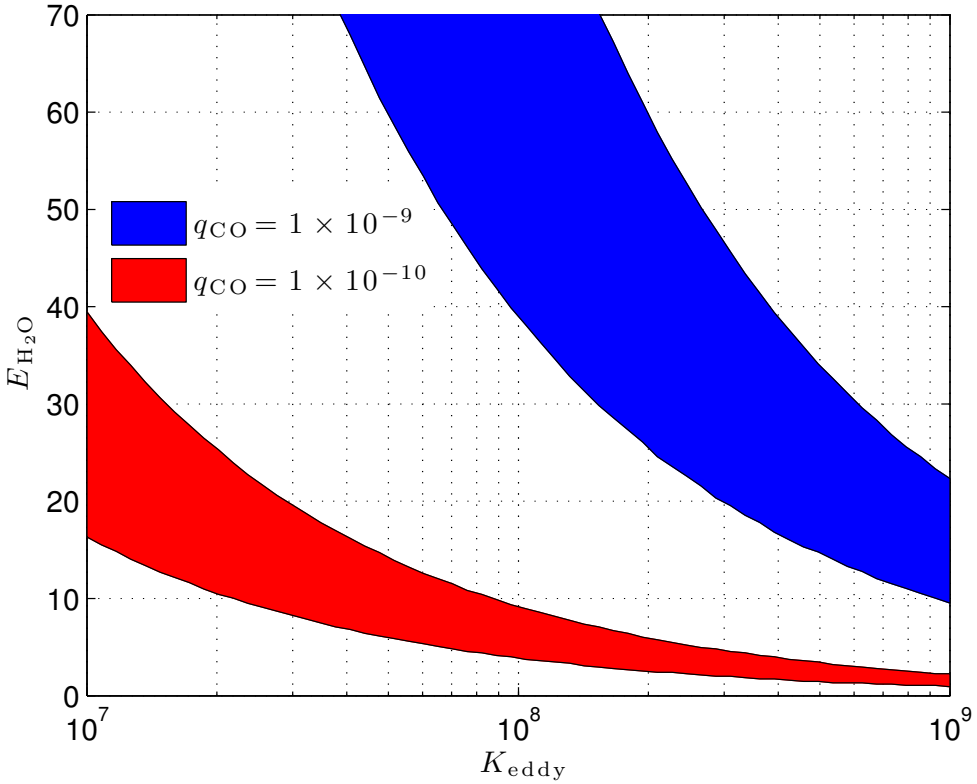

Figure 3.8 Chemical constraints on Saturn's deep water abundance using CO kinetic model from Venot et al. [2012]. We consider two hypothetical tropospheric CO mixing ratio, namely, $q_{\mathrm{CO}} = 1 \times 10^{-9}$ and $q_{\mathrm{CO}} = 1 \times 10^{-10}$. The uncertainty indicated by shaded area is due to the uncertainty of the rate coefficients. We did not impose a constraint on K_{eddy} since it sensitively depends on the latitude where CO measurement is taken.

where n_i is the number density of species i, S_i is the net production(loss) rate, and ϕ_i is the vertical flux given by

$$\phi_i = n_i K_{\rm eddy} \frac{1}{y_i} \frac{\partial y_i}{\partial z}, \tag{3.36}$$

where y_i is the mass fraction of species i. The chemical source term S_i is calculated by *cantera*, a software toolkit for solving problems involving chemical kinetics [Goodwin et al., 2015]. We take the equilibrium state as the initial condition of our model, and let the system evolve into a steady state. The steady state $X_{\rm CO}$ can be extracted from our model, for given inputs of $K_{\rm eddy}$ and $E_{\rm H2O}$.

We check the consistency between our model and the diffusion-kinetic model used in Mousis et al. [2014], the latter of which is adapted from the model used in Venot et al. [2012]. Assuming O/H is 21 times solar, C/H is 9 times solar, and $K_{\rm eddy}$ = 10^9 cm^2 s^{-1}, the model in Mousis et al. [2014] derived a CO mole fraction of 1×10^{-9} for Saturn. Using the same input, our model derived a CO mole fraction of 1.1×10^{-9}. Therefore, the two models are producing similar results, with the remaining differences probably coming from the uncertainties on the adiabat.

Although the diffusion-kinetic model is robust in calculating $X_{\rm CO}$ for given $K_{\rm eddy}$ and $E_{\rm H_2O}$, it is very time-consuming to explore the parameter space of ($K_{\rm eddy}$, $E_{\rm H_2O}$, $X_{\rm CO}$) using this method. Therefore, we developed an approximation method based on the timescale approach, which is easy and quick to implement, and accurate enough compared with the full diffusion-kinetic modeling method. The timescale approach requires the estimation of the chemistry timescale $\tau_{\rm chem}$. We assume there exists a rate limiting step $\rm R1 + R2 \rightarrow P1 + P2$, then

$$\tau_{\rm chem} = \frac{\rm [CO]}{d\rm [CO]/dt} = \frac{\rm [CO]}{k_{rls}[R1][R2]}, \tag{3.37}$$

where k_{rls} is the rate coefficient of the rate limiting step. Note that k_{rls} is generally proportional to $e^{-E/T}$, where E is the activation energy. [R1] and [R2] can be related to $[\mathrm{CO}]$ and $[\mathrm{H_2}]$ via the equilibrium constants and some powers of pressure. The equilibrium constants are proportional to $e^{\Delta G/T}$, where ΔG is the change of Gibbs free energy of formation in the reaction. Therefore, it is reasonable to assume $\tau_{\mathrm{chem}} = Ce^{A/T}p^{\alpha}$, where A, C and α are constant coefficients that need to be fitted.

We fit the coefficients based on the numerical results from our diffusion-kinetic model. Note that for each diffusion-kinetic simulation, we have numerical values for (K_{eddy}, $E_{\mathrm{H_2O}}$, X_{CO}), where K_{eddy} and $E_{\mathrm{H_2O}}$ are input parameters, and X_{CO} is the simulation result. We use the following procedure to fit the coefficients A, C and α. (1) With X_{CO} and $E_{\mathrm{H_2O}}$, we used equilibrium chemistry of CO to find out the quench temperature T_q and quench pressure p_q. (2) With K_{eddy}, we calculated the mixing timescale at the quench level. The chemical timescale at quench level $\tau_{\mathrm{chem,q}}$ is equal to the mixing timescale. (3) We therefore have one set of numerical values for (T_q, p_q, $\tau_{\mathrm{chem,q}}$) from each simulation. We run three simulations for Jupiter and three simulations for Saturn with different K_{eddy} and $E_{\mathrm{H_2O}}$, and use the six sets of data to fit the coefficients A, C and α. The derived fitting formula for τ_{chem} is:

$$\tau_{\mathrm{chem}} \approx (5 \times 10^{-6} e^{2.8\times10^4/T}) p^{-1.29} \text{ s}. \tag{3.38}$$

With the chemical timescale τ_{chem} available, we followed the procedures described in Section 3.1 to implement the timescale approach. Note that the effective length scale L_{eff} is calculated following the recipe described in Smith [1998], which has dependence on τ_{chem}. For the *Venot model*, we find $L_{\mathrm{eff}} \approx 0.10H$ for Jupiter, and $L_{\mathrm{eff}} \approx 0.12H$ for Saturn. We compared X_{CO} calculated by the timescale approach with X_{CO} calculated by the full-diffusion kinetic modeling

in Table 2. For different combinations of $K_{\rm eddy}$ and $E_{\rm H_2O}$, we find the difference on $X_{\rm CO}$ is within 10% between the timescale approach and full-diffusion kinetic modeling. This validated the timescale approach and the $\tau_{\rm chem}$ we estimated in equation (3.38).

Using the timescale approach, we derived the constraint on Jupiter's $E_{\rm H_2O}$. The constraint is shown in Fig 3.7 where find $E_{\rm H_2O} = 3 \sim 11$. As a comparison, $E_{\rm H_2O} = 0.1 \sim 0.75$ using the *VM model*. In Fig. 3.8, we plot the constraint on $E_{\rm H_2O}$ for Saturn using the *Venot model*. We did not constrain $K_{\rm eddy}$ here since it sensitively depends on latitude. In the future, once the abundance of tropospheric CO is measured, we can refer to Fig 3.4 or Table 3.1 to get $K_{\rm eddy}$, then refer to Fig. 3.8 to find the constraint on $E_{\rm H_2O}$.

3.4 Discussion

In this paper, we revisited the constraints on Jupiter's deep water abundance by disequilibrium species CO. We proposed a new formulation of eddy diffusion coefficient, based on laboratory studies of turbulent rotating convection. With newer eddy diffusion coefficient, we updated the constraints on Jupiter's deep water abundance. Using the rate limiting step from Visscher and Moses [2011], we find $E_{\rm H_2O} = 0.1 \sim 0.75$. We also consider another chemical model from Venot et al. [2012], and the constraints on deep water abundance are $E_{\rm H_2O} = 3 \sim 11$. We do not consider the possibility of a strong compositional stratification of either Jupiter or Saturn in which the heavy element abundance increases toward the center of the body [Leconte and Chabrier, 2012]. It is possible that the gravitational field measurements to be made by Juno at Jupiter and

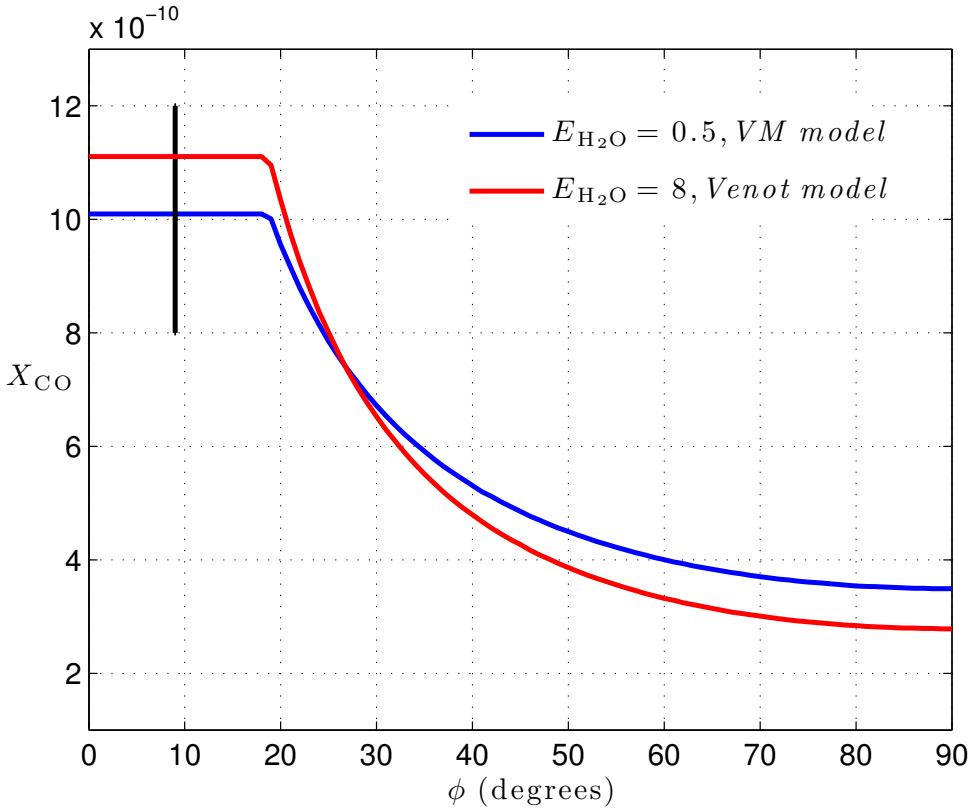

Figure 3.9 Prediction of tropospheric X_{CO} as a function of latitude for a given $E_{\mathrm{H_2O}}$. We consider two CO kinetic models, namely, the *VM model* [Visscher and Moses, 2011] and the *Venot model* [Venot et al., 2012]. The error bar indicates the measurement of X_{CO} at 9 degrees by Bézard et al. [2002]

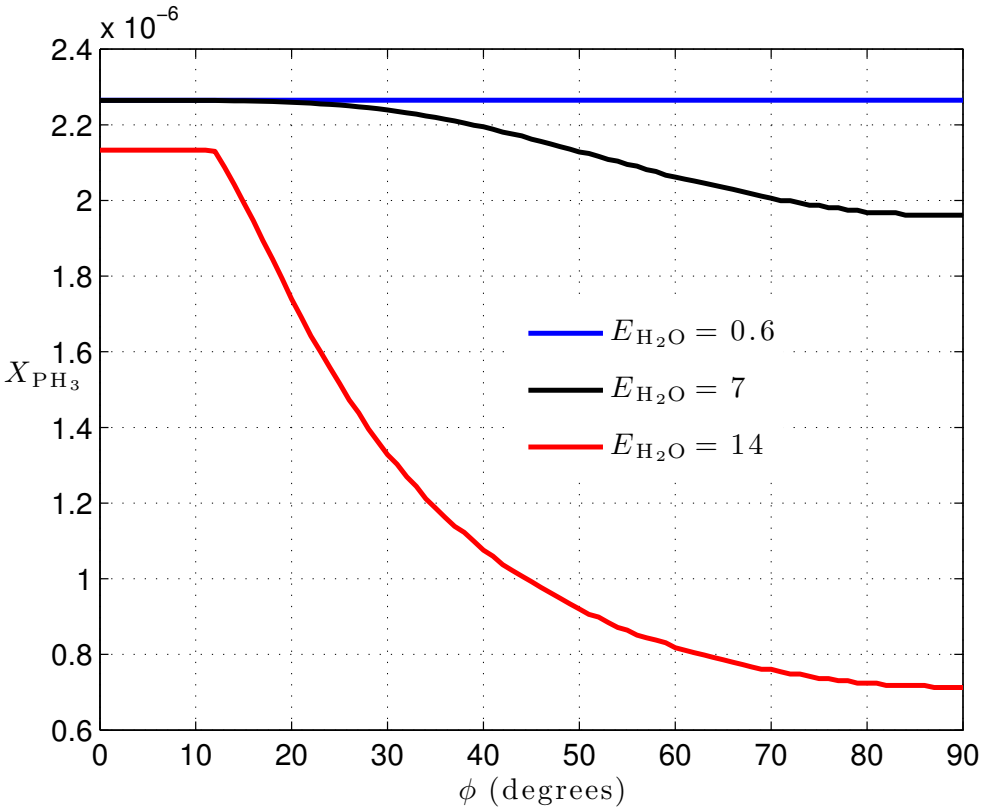

Figure 3.10 Prediction of $X_{\mathrm{PH_3}}$ as a function of latitudes for given values of $E_{\mathrm{H_2O}}$. The bulk phosphorus abundance is taken as $X_{\mathrm{P}} = 2.3\times10^{-6}$ [Mousis et al., 2012]. The rate limiting step for PH_3 - P_4O_6 conversion is taken as equation (3.40) [Visscher and Fegley, 2005].

Cassini at Saturn will provide constraints on the degree of such differentiation, but the problem of deriving oxygen abundance from such differentiation may be difficult to resolve.

The distinct ranges of E_{H_2O} found in Jupiter with the two kinetic models require very different formation conditions. The range of E_{H_2O} ($\sim$0.1–0.75) found with the kinetic model of Visscher and Moses [2011] necessities the formation of Jupiter in a region of the protosolar nebula that is strongly depleted in oxygen. A moderate H_2O enrichment by a factor of $\sim$2 in Jupiter already corresponds to a substantial *depletion* of the oxygen abundance by a factor of $\sim$2 in its feeding zone [Mousis et al., 2012]. This implies that the oxygen abundance in Jupiter's feeding zone should be depleted by factors of $\sim$5–40 times, compared to the protosolar abundance, for values of E_{H_2O} found in the $\sim$0.1–0.75 range in the envelope. Such a high oxygen depletion might be explained if Jupiter formed at a slightly lower heliocentric distance than the iceline in the protosolar nebula. At this location, the diffusive redistribution and condensation of water vapor induces two effects: it increases the density of ice at the position of the iceline but it also drops the water vapor abundance at distances slightly closer to the Sun [Stevenson and Lunine, 1988, Ali-Dib et al., 2014]. However, at this location, because the disk's temperature is higher than the water condensation temperature, it becomes difficult to accrete efficiently icy planetesimals in Jupiter's envelope in order to explain the giant planet's overall elevated metallicity. In this context, a possible explanation of the observed enrichments in Jupiter could lie in its late formation in the protosolar nebula. In this case, the photoevaporation of the disk and the delivery of condensible species in vapor forms from its outer regions may lead to a progressive homogeneous enrichment of the disk in heavy elements [Guillot and Hueso, 2006]. Jupiter's metallicity would be then

representative of the heavy element enrichment acquired by the disk's gas from which it accreted.

On the other hand, the range of E_{H_2O} ($\sim$3–11) found with the kinetic model of Venot et al. [2012] corresponds to cases of Jupiter formation in environments where the O abundance varies from moderately depleted to slightly enriched compared to the protosolar value. The value of E_{H_2O} $\sim$7 is predicted in Jupiter when it accreted planetesimals formed from a gas phase of protosolar composition [Mousis et al., 2012]. In this case, Jupiter's building blocks were agglomerated from a mixture of clathrates and pure ices condensed down to $\sim$22 K in the protosolar nebula. Any value of E_{H_2O} lower than $\sim$7 requires the formation of Jupiter at a slightly lower heliocentric distance than the ice line in the protosolar nebula. In contrast, values of E_{H_2O} higher than $\sim$7 correspond to an increase of the water abundance in the giant planet's feeding zone, thus easing the trapping of volatiles in the form of clathrates at higher disk's temperature (in the $\sim$50–80 K temperature range; Mousis et al. [2009, 2012]). In both cases, the volatiles responsible for the enrichments measured at Jupiter were supplied either via the partial erosion of its core or via accretion of planetesimals dragged from the nebula during the hydrodynamical collapse of the envelope.

In the case of Saturn, the range of E_{H_2O} remains still loosely constrained because no inner limit has been found for the internal source of CO. For the moment, depending on the value of E_{H_2O}, the range of conclusions made for Jupiter applies to Saturn as well. When an inner limit for the internal source of CO is set in the future, it will be possible to derive more specific conclusions.

Our model is still subject to improvements in the following aspects:

- *CO kinetic models*

  With a better assessment of the kinetics of chemical reactions, our model should allow derivation of a much narrower range of deep water abundances in Jupiter, and subsequently provide more robust constraints on their formation conditions. Currently, the two kinetic models, *VM model* and *Venot model*, place very different constraints on deep water abundance. The *VM model* is derived from previous Jupiter and Saturn models [e.g., Gladstone et al., 1996, Moses et al., 1995a,b, 2000a,b], with extensive updates on high temperature kinetics from combustion chemistry studies [Visscher et al., 2010]. As a comparison, the *Venot model* is based on a C0-C2 reaction base originally developed for industrial applications. A mechanism for nitrogen is coupled to the C0-C2 reaction base to model C/N/O/H chemistry. According to Venot et al. [2012], their model has been validated by various experiments over a large range of pressure and temperature [e.g., Battin-Leclerc et al., 2006, Bounaceur et al., 2007, Anderlohr et al., 2010, Bounaceur et al., 2010, Wang et al., 2010], while the *VM model* has not been validated against experiments. From this aspect, *Venot model* is more plausible than the *VM model*.

- *Potential Tests on $K_{\rm eddy}$ Formulation Using JIRAM on Juno*

  Although our new formulation of $K_{\rm eddy}$ has been validated against laboratory experiments, there are still no observational constraints on Jupiter's or Saturn's $K_{\rm eddy}$.

  The microwave radiometer onboard Juno spacecraft should be able to measure the deep water abundance in Jupiter [Janssen et al., 2005]. If performed, this measurement should be able to place constraints on $K_{\rm eddy}$, as is shown in Fig. 3.5 and Fig. 3.7.

We have predicted the dependence of $K_{\rm eddy}$ on latitude, thus the concentration of disequilibrium species should have a latitudinal variation. Measurement of disequilibrium species at different latitudes will be able to provide a test of the latitudinal dependence. In Fig. 3.9, we plot the calculated $X_{\rm CO}$ in the tropopshere as a function of latitudes. $X_{\rm CO}$ near the equator is about three times $X_{\rm CO}$ near the pole. Currently the only measurement of tropospheric CO is at 9° N [Bézard et al., 2002]. Measurement of CO at higher latitudes with less than 20% uncertainty would be able to distinguish the latitudinal variation, and thus test our formulation of $K_{\rm eddy}$.

Another disequilibrium species that has been detected in Jupiter's atmosphere is PH_3. Tropospheric abundance of PH_3 was measured by Cassini CIRS. The average value of $X_{\rm PH_3}$ below 1 bar is estimated to be $(1.9 \pm 0.1) \times 10^{-6}$ [Irwin et al., 2004, Fletcher et al., 2009b], which is order of magnitude larger than its equilibrium abundance, indicating its state of disequilibrium. The net reaction for $\rm PH_3$ destruction is [Prinn et al., 1984, Fegley and Prinn, 1985, Visscher and Fegley, 2005]

$$4\mathrm{PH_3} + 6\mathrm{H_2O} = \mathrm{P_4O_6} + 12\mathrm{H_2}. \tag{3.39}$$

Following Visscher and Fegley [2005], we use the reaction

$$\mathrm{PH_3} + \mathrm{OH} \rightarrow \mathrm{H_2POH} + \mathrm{H} \tag{3.40}$$

as the rate limiting step. The bulk phosphorus abundance is unknown. We take $X_P = 2.3 \times 10^{-6}$, which is consistent with the calculations by Mousis et al. [2012]. In Fig. 3.10, we plot the calculated $X_{\rm PH_3}$ as a function of latitude. The profile sensitively depends on the deep water abundance. For low water abundance (e.g. $E_{\rm H_2O}$ = 0.6), $\rm PH_3$ is the dominant species

regardless of $K_{\rm eddy}$. However, at large water abundance (e.g. $E_{\rm H_2O}$ = 14), the dependence on $K_{\rm eddy}$ is very sensitive.

The spectrometer JIRAM on board Juno will be able to retrieve the abundance of CO and PH_3 at 3$\sim$10 bars. The relative error for CO should be about 60%, and for PH_3 it should be about 30% [Grassi et al., 2010]. From Fig. 3.9, the latitudinal variation of CO is at the limit of instrument (60% relative error). From Fig. 3.10, if Jupiter has a bulk water abundance of $E_{\rm H_2O} \gtrsim 7$, then JIRAM should be able to see the latitudinal variation, otherwise, the latitudinal variation is too small to be resolved by JIRAM.

- *Effects of Horizontal Mixing*

  Although we predicted a latitudinal variation of CO and PH_3, we ignored the effect of possible horizontal mixing that tends to homogenize latitudinal gradients. If we assume horizontal mixing is driven by eddy diffusion, and assume horizontal $K_{\rm eddy}$ is of similar order to vertical $K_{\rm eddy}$, then the horizontal mixing timescale $\tau_{\rm mix,h} \sim R_J^2/K_{\rm eddy} \sim 10^{11}$ s, which is much larger than the vertical mixing timescale $\tau_{\rm mix} \sim 10^6$ s. Therefore, horizontal eddy diffusion is not able to effectively homogenize disequilibrium species in the troposphere. However, if significant horizontal circulation across latitudes exists, the horizontal mixing could be enhanced. Consider the meridional velocity v, and meridional scale R_J, then the horizontal mixing timescale $\tau_{\rm mix,h} \sim R_J/v$. For v = 10 m s^{-1}, $\tau_{\rm mix,h} \sim 7 \times 10^6$ s. Compared with vertical mixing timescale $\tau_{\rm mix} \sim 10^6$ s, horizontal mixing could smooth out the latitudinal gradient to some degrees. The determination of horizontal profile of CO or PH_3 under horizontal mixing would require the knowledge of tropospheric circulation of Jupiter, which is still unknown.

  Although we do not know exactly the extent of horizontal mixing, we can

explore its effect on the constraints of $E_{\mathrm{H_2O}}$ by considering two extreme conditions, namely, no mixing and 100% mixing. For no mixing, the results are $E_{\mathrm{H_2O}} = 0.1 \sim 0.75$ using the *VM model* and $E_{\mathrm{H_2O}} = 3 \sim 11$ using the *Venot model*. For 100% mixing, we assume CO is well mixed across latitudes. According to our calculations, the results are $E_{\mathrm{H_2O}} = 0.2 \sim 1.0$ using the *VM model* and $E_{\mathrm{H_2O}} = 4.7 \sim 16.3$ using the *Venot model*. Therefore, horizontal mixing does not significantly affect our constraints on Jupiter's deep water abundance.

3.5 Conclusion

In this paper, we improved the thermochemical constraints on Jupiter's deep water abundance in two aspects. First, we developed a new formulation for eddy diffusion coefficient based on experiments dedicated to turbulent rotating convection. Application of the new formula to Jupiter and Saturn reveals a smooth transition from slow rotation regime (near the equator) to rapid rotation regime (near the pole), and a strong latitudinal dependence. We estimate an uncertainty for our newly-derived coefficient of less than 25%, which is much better than the one order of magnitude used in the literature. Secondly, we considered two updated chemical-kinetic models and derived the constraints on Jupiter's deep water abundance. Using the rate limiting step proposed by Visscher and Moses [2011], we find the enrichment of water (relative to solar) for Jupiter is $E_{\mathrm{H_2O}} = 0.1 \sim 0.75$, while using the chemical-kinetic model proposed by Venot et al. [2012], we find $E_{\mathrm{H_2O}} = 3 \sim 11$. With a better assessment of chemical kinetics, our model should allow deriving a much narrower range of deep water abundance in Jupiter. The constraint on Saturn's deep water abundance

is still loose due to the lack of measurements of tropospheric CO abundance.

CHAPTER 4

MODELING DISEQUILIBRIUM SPECIES FOR JUPITER AND SATURN: IMPLICATIONS FOR JUNO AND SATURN ENTRY PROBE

4.1 Introduction

Disequilibrium species in the atmosphere of Jupiter and Saturn can be used to constrain the deep water abundance and the deep eddy diffusion coefficient in the atmospheres of Jupiter and Saturn [e.g., Prinn and Barshay, 1977, Fegley and Lodders, 1994]. Various disequilibrium species such as CO, PH_3, GeH_4, and AsH_3 have been detected on Jupiter and Saturn with abundances orders of magnitude higher than their respective chemical equilibrium abundances at the pressure level where they are observable [e.g., Beer, 1975, Noll et al., 1986, Ridgway et al., 1976, Larson et al., 1980, Fink et al., 1978, Noll et al., 1988, Bézard et al., 1989, Noll et al., 1989]. These species at a few bars are transported upward by vertical mixing from the deep atmosphere where they are more abundant, therefore, they contain the information of the atmosphere down to a few hundred bars. In this paper, we model the vertical profiles of disequilibrium species with updated thermodynamic and kinetic data. The dependence on the water abundance and the eddy diffusion coefficient is investigated.

Our study is timely for the following reasons. The JIRAM instrument on board the Juno spacecraft will be able to measure the disequilibrium species CO, PH_3, GeH_4, and AsH_3 down to a few bars when it will arrive at Jupiter in 2016 [Grassi et al., 2010]. The microwave radiometer onboard Juno will also be able to measure the deep water abundance [Janssen et al., 2005]. With the abundances of disequilibrium species and water, constraints should be made

on the deep eddy diffusion coefficient. A Saturn probe proposal has been submitted to the ESA 2015 call for medium class mission [Mousis et al., 2015] and a similar concept is under study for a submission to the NASA 2016 New Frontier call[Atkinson et al., 2012]. Current entry probes are designed to go down to 10–20 bar and can make in-situ measurements of the atmosphere composition via mass spectrometry [Wong et al., 2004]. However, it is unlikely that such probes will be able to descend below the water cloud deck and measure the deep water abundance. A study with the updated kinetic data is then necessary for evaluating whether deep water abundance can be effectively constrained by disequilibrium species.

We use the diffusion-kinetic model developed in Wang et al. [2015]. A C/N/O/H reaction network is employed to predict the abundances of various carbon bearing species. The reaction networks for P/H/O and Si/H/O species are applied for the first time to study planetary atmospheres in this paper. New chemical pathways for PH_3 and GeH_4 destructions are then proposed. New compilations of thermochemical data, especially for P, Ge, and As, are used in our model.

The paper is organized as follows. In section 4.2, we introduce the current status of the measurement of disequilibrium species. In section 4.3, we describe our models for the chemistry and transport of disequilibrium species. In section 4.4, we present our results. In section 4.5, we discuss the implications for Juno and a Saturn entry probe. The conclusions are summarized in section 4.6.

Table 4.1 Observed mixing ratios of some disequilibrium species

	Jupiter		Saturn	
	q	references	q	references
CO	$1.0\pm0.2\times10^{-9}$	Bézard et al. [2002]	$<1.0\times10^{-9}$	Cavalié et al. [2009]
PH_3	$8\pm1\times10^{-7}$	Irwin et al. [1998]	$4\pm1\times10^{-6}$	Fletcher et al. [2011]
SiH_4	$<2.5\times10^{-9}$	Treffers et al. [1978]	$<2\times10^{-10}$	Noll and Larson [1991]
GeH_4	$7\pm2\times10^{-10}$	Bjoraker et al. [1986]	$4\pm2\times10^{-10}$	Noll et al. [1988]
AsH_3	$2.2\pm1.1\times10^{-10}$	Noll et al. [1990]	$3\pm1\times10^{-9}$	Noll and Larson [1991]

4.2 Measurements of disequilibrium species: current status

The tropospheric abundances of CO, PH_3, SiH_4, GeH_4 and AsH_3 are primarily measured in the 5μm window for Jupiter and Saturn. Apart from a 1 ppb tropospheric component [e.g., Larson et al., 1978, Bjoraker et al., 1986], CO also has a stratospheric component [e.g., Bézard et al., 2002]. The tropospheric CO is supplied by vertical convective mixing from deep levels where CO prevails [Prinn and Barshay, 1977], while the stratospheric CO can be supplied by micrometeoroids [Prather et al., 1978], infalling materials from icy satellites [Strobel, 1979], or shock chemistry from infalling kilometer to subkilometer-sized comets [Lellouch et al., 1995, Bézard et al., 2002]. At Jupiter and Saturn, comets are more probable than other sources [Bézard et al., 2002, Cavalié et al., 2010]. The tropospheric CO contains information on the deep atmosphere, and thus can be used to probe the deep water abundance and the deep eddy diffusion coefficient. The retrieval of Saturn's tropospheric CO has not been successful due to its very low mixing ratios [Cavalié et al., 2009]. Tropospheric PH_3 was measured in the 5μm window for Jupiter with a mixing ratio of $(6 \sim 9) \times 10^{-7}$ [e.g., Kunde et al., 1982, Bjoraker et al., 1986, Encrenaz et al., 1996, Irwin et al., 1998], and for Saturn with a mixing ratio of $(3 \sim 5) \times 10^{-6}$ [e.g., Noll and Larson, 1991, de Graauw et al., 1997, Fletcher et al., 2011]. The vertical profile of PH_3 was retrieved from the spectra by Cassini CIRS and VIMS [Fletcher et al., 2009a, 2011]. The PH_3

abundance starts to be depleted in the upper troposphere where the pressure is about 1 bar [Fletcher et al., 2012], due to decreased eddy mixing, UV photolysis and chemical re-equilibration [Irwin et al., 1998, 2004]. Tropospheric GeH_4 was identified and measured at the 5μm window [Fink et al., 1978, Noll et al., 1988] at a mixing ratio of a few times 10^{-10}. The mixing ratio of GeH_4 in the stratosphere is expected to be lower than that in the troposphere because of UV photolysis. The tropospheric AsH_3 was measured on both Jupiter and Saturn [Bézard et al., 1989, Noll et al., 1989, Noll and Larson, 1991]. The mixing ratio of AsH_3 on Jupiter is about 2×10^{-10} [Noll et al., 1990], while for the Saturn, the mixing ratio is about 3×10^{-9} [Bézard et al., 1989, Noll and Larson, 1991]. In table 4.1, we summarize the measurements of tropospheric CO, PH_3, SiH_4, GeH_4, and AsH_3 abundances for both Jupiter and Saturn.

4.3 Model

4.3.1 Introduction to the model

Table 4.2 Elemental abundances used in the simulation for Jupiter and Saturn.

	Jupiter			Saturn		
	q	E	references	q	E	references
He	0.157	0.920	Niemann et al. [1998]	0.135	0.794	Conrath and Gautier [2000]
C	2.37×10^{-3}	4.4	Wong et al. [2004]	5.33×10^{-3}	9.91	Fletcher et al. [2009b]
N	6.64×10^{-4}	4.92	Wong et al. [2004]	4.54×10^{-4}	3.36	Fletcher et al. [2011]
O	variable in the simulation			variable in the simulation		
S	8.90×10^{-5}	3.38	Wong et al. [2004]	3.76×10^{-4}	14.3	Briggs and Sackett [1989]
P	7×10^{-7}	1.4	Irwin et al. [1998]	4×10^{-6}	7.8	Fletcher et al. [2011]
Si	2.85×10^{-4}	4.4	assumed	6.47×10^{-4}	10	assumed
Ge	3.93×10^{-8}	4.4	assumed	8.93×10^{-8}	10	assumed
As	2.2×10^{-10}	0.55	Noll et al. [1990]	3.0×10^{-9}	7.5	Noll and Larson [1991]

The elemental abundances of Jupiter and Saturn used in this paper are sum-

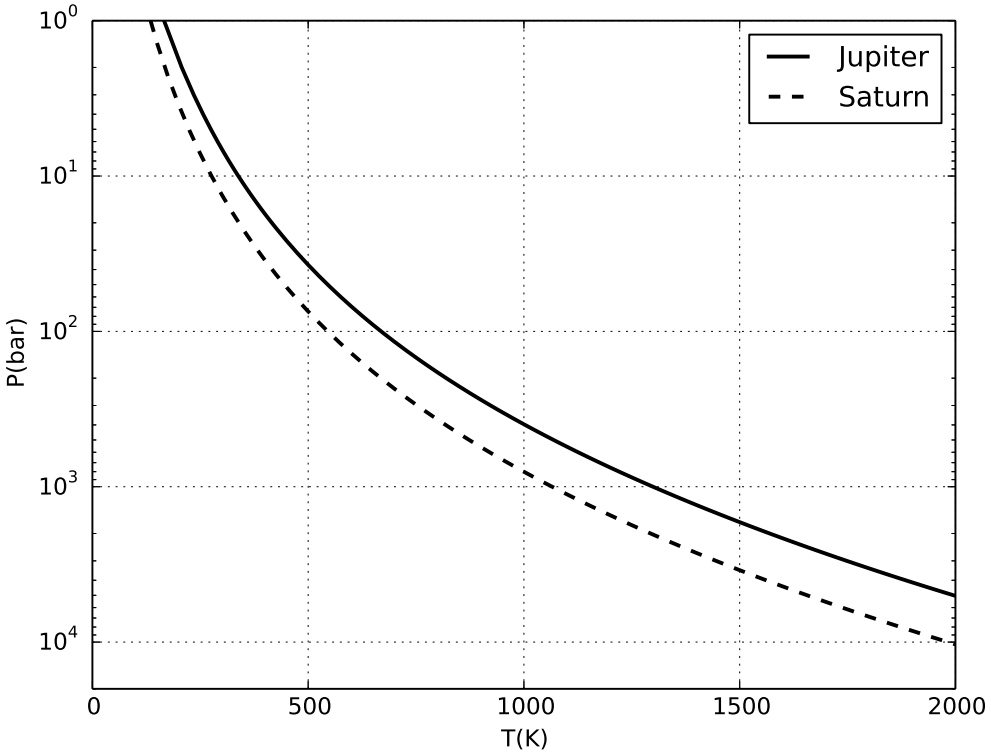

Figure 4.1 Adiabatic profiles of Jupiter and Saturn computed following the method described in Fegley and Prinn [1985].

marized in table 4.2. We use the solar composition table from Asplund et al. [2009] as our reference. The elemental abundances are inferred from the observed abundances of their hydrogen compounds. For phosphorus, we assume the total phosphorus abundance is equal to the observed PH_3 abundance. For silicon and germanium, we assume they have enrichments similar to carbon, since their observed hydrogen compounds (SiH_4 and GeH_4) do not represent their total elemental abundances. For arsenic, we assume its total abundance is represented by the observed AsH_3 abundance.

4.4 Results

In this section, we predict the abundances of various disequilibrium species in Jupiter's and Saturn's atmospheres at a few bars pressure. Above this altitude level, the abundances are affected by photochemistry and the enrichment from external sources, which are not included in our calculations here. The dependence on the water abundance and the deep eddy diffusion coefficient are investigated.

We make a few definitions regarding the abundance of species Z. Its concentration is denoted as [Z] with units of molecules·cm^{-3}. Mole fraction of Z is denoted as $X_{\rm Z}$ = [Z]/n, where n is total number density of the atmosphere (molecule·cm^{-3}). Mixing ratio is denoted as $q_{\rm Z}$ = [Z]/[H_2]. For an element M, we define E_M as the enrichment of M relative to solar, which is the ratio of [M]/[H] in the planet to that in the Sun, where [M] and [H] are the total number density of M and H atoms respectively, in whatever form. The elemental composition of the solar atmosphere is taken from Asplund et al. [2009]. The el-

emental abundances of Jupiter and Saturn used in our simulations can be found in Table 4.2.

4.4.1 Simulation results using the C/N/O/H reaction network

The C/N/O/H reaction network used is described in section 2. We considered the two aforementioned reaction networks, namely, network A and network B. The vertical profile of the mixing ratios of species is computed and the ($E_{\mathrm{H_2O}}$, K_{eddy}) parameter space is investigated. As an illustration, the mixing ratios along Jupiter's adiabat for parameters $E_{\mathrm{H_2O}}$ = 10 and K_{eddy}=1×10^8 cm^{2}s^{-1} using the network A are presented in Fig. 4.2. Our calculations show that N_2 is the major nitrogen bearing species after NH_3 with a mixing ratio of about 1 ppm. C_2H_6, CO and CO_2 are the major carbon bearing species after CH_4. CO and CO_2 are the major oxygen bearing species after H_2O. The mixing ratio of CO and C_2H_6 are at 1 ppb level, while the mixing ratio of CO_2 is about 0.1 ppb. Mixing ratios of other species such as CH_3NH_2 and HCN are below 1×10^{-12}.

We focus on three species, CO, C_2H_6 and CO_2, and investigate their dependence on parameters $E_{\mathrm{H_2O}}$ and K_{eddy}. For each combination of ($E_{\mathrm{H_2O}}$, K_{eddy}), we run the simulation to steady state. The mixing ratios of C_2H_6, CO, and CO_2 have been extracted from each simulation and the results are summarized in Fig. 4.2. As is shown by the figure, the abundance of C_2H_6 is sensitive to the vertical eddy diffusion coefficient while it is not affected by the deep water abundance. Therefore, C_2H_6 is a good tracer for the eddy diffusion coefficient alone. In contrast, the abundance of CO is both sensitive to the eddy diffusion coefficient and the deep water abundance. The constraints on the deep water abundance

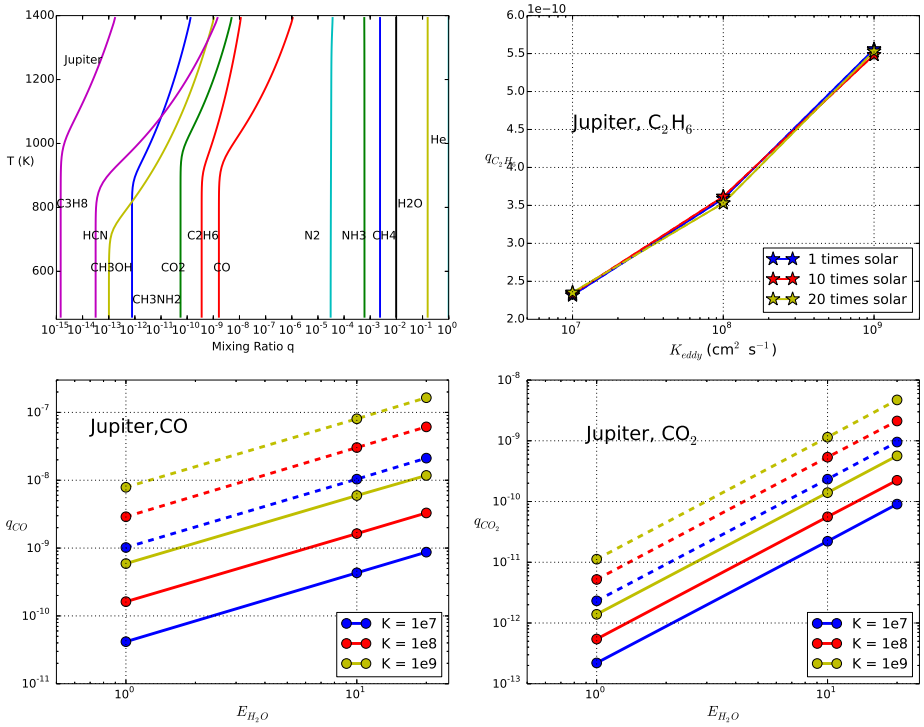

Figure 4.2 Simulation results for Jupiter using the C/N/O/H reaction network. Upper left plot is the mixing ratio of species along Jupiter's adiabatic profile for parameters: $E_{\mathrm{H_2O}}$ = 10 and K_{eddy}=1×10^8 cm^{2}s^{-1} using the network A. Only species with mixing ratios $q > 1 \times 10^{-15}$ at 450 K are plotted. Upper right plot is the predicted mixing ratio of C_2H_6 as a function of K_{eddy} for a range of assumed water abundances. Solid lines are calculated using network A, and dashed lines are calculated using network B. Lower plots are the predicted mixing ratio of CO and CO_2 as a function of the water enrichment $E_{\mathrm{H_2O}}$ for different vertical eddy diffusion coefficient K_{eddy}. Solid lines are calculated using network A, and dashed lines are calculated using network B.

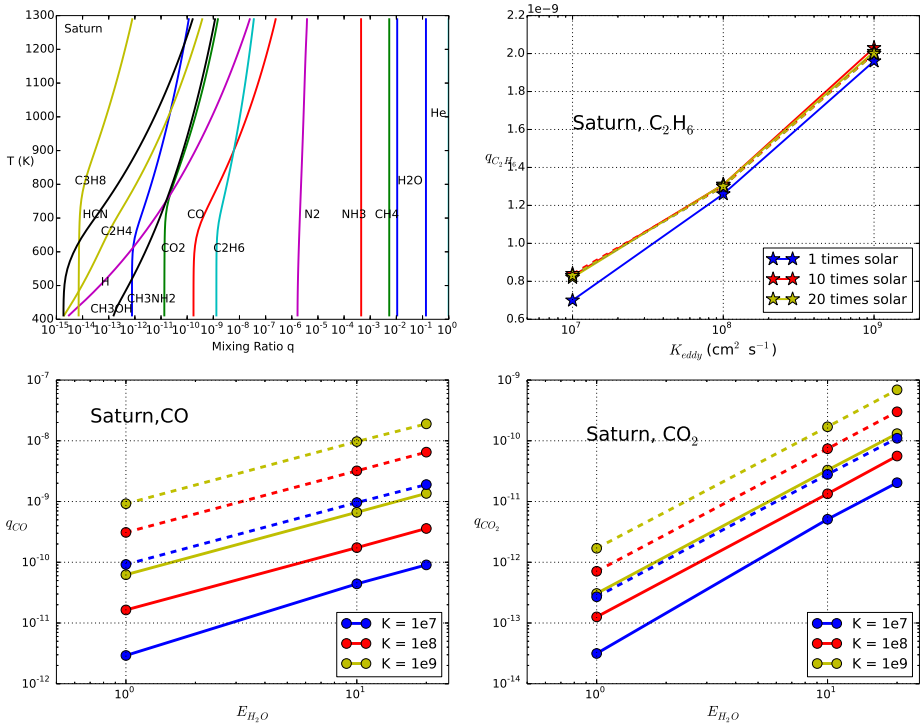

Figure 4.3 Simulation results for Saturn using the C/N/O/H reaction network. Upper left plot is the mixing ratio of species along Saturn's adiabatic profile for parameters: $E_{\mathrm{H_2O}}$ = 10 and K_{eddy}=1×10^8 cm^{2}s^{-1} using the network A. Only species with mixing ratios $q > 1 \times 10^{-15}$ at 400 K are plotted. Upper right plot is the predicted mixing ratio of C_2H_6 as a function of K_{eddy} for a range of assumed water abundances. Solid lines are calculated using network A, and dashed lines are calculated using network B. Lower plots are the predicted mixing ratio of CO and CO_2 as a function of the water enrichment $E_{\mathrm{H_2O}}$ for different vertical eddy diffusion coefficient K_{eddy}. Solid lines are calculated using network A, and dashed lines are calculated using network B.

placed by the CO abundance is limited by the information on the eddy diffusion coefficient. If both CO and C_2H_6 can be measured, we can use the mixing ratio of C_2H_6 to put a tight constraint on the $K_{\rm eddy}$, then we can determine how much water is needed to match the observed CO abundance with the predicted CO abundance. CO_2 is another tracer for the deep water abundance and the eddy diffusion coefficient. Although it is very sensitive to the water abundance ($\propto E^2_{\rm H_2O}$), its mixing ratio is an order of magnitude less than CO, making it more difficult to be measured. In Fig. 4.2, we also show the results computed using the network B. The predictions on CO and CO_2 abundances using network B are very different from those using network A. Therefore, significant uncertainties still remain for the CO kinetics that require laboratory measurements for their definite resolutions.

The tropospheric CO abundance on Jupiter was measured at the Northern Equatorial Belt ($\sim\ 9^\circ$) by Bézard et al. [2002] with a mole fraction of $(1.0 \pm 0.2) \times 10^{-9}$. Combined with the predicted eddy diffusion coefficient of $\sim 1 \times 10^8$ cm^{2}s^{-1} [Wang et al., 2015] near the equatorial regions, the deep water abundance is constrained to be ~ 7 times solar with network A and ~ 0.6 times solar with network B.

The simulation results for Saturn are presented in Fig. 4.3. Similarly to the results for Jupiter, we find C_2H_6 is a good tracer for the eddy diffusion coefficient. Both CO and CO_2 are good tracers for the deep water abundance. Dual constraints from CO and C_2H_6 can break the degeneracy between high (low) eddy diffusion coefficient and high (low) deep water abundance.

The tropospheric CO abundance on Saturn was not measured so far and an upper limit is put by Cavalié et al. [2009] with a mixing ratio smaller than 1

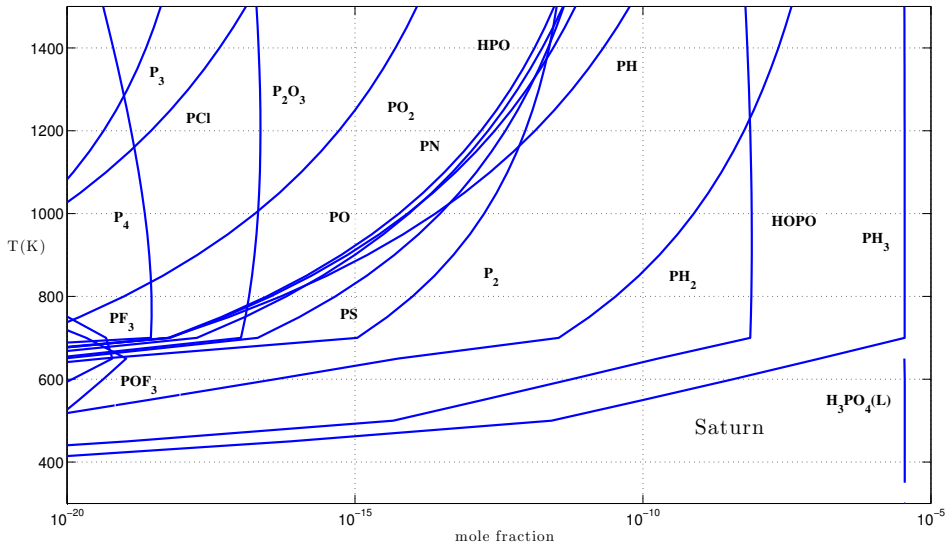

Figure 4.4 Equilibrium mole fractions of phosphorus containing species along Saturn's adiabat computed using the NASA Chemical Equilibrium Application (CEA) software. The elemental input we used are P/H = 7.8 times solar, O/H = 10 times solar, and other elemental abundances are solar except He, C, N, S, Si, Ge, and As, which are listed in table 4.2.

ppb. Combined with the predicted eddy diffusion coefficient of $\sim 1\times10^8$ cm^{2}s^{-1} [Wang et al., 2015] near the equator, the deep water abundance is constrained to be $\lesssim 60$ times solar with network A and $\lesssim 10$ times solar with network B.

4.4.2 Simulation results using the H/P/O reaction network

We use the NASA CEA chemical equilibrium code to compute the equilibrium abundances of phosphorus containing species along Saturn's adiabat, and the results are shown in Fig. 4.4. The elemental abundances used in the calculations are summarized in Table 4.2. Our calculations show that H_3PO_4 is the major phosphorus bearing species below 700 K instead of P_4O_6 in the literature [e.g.,

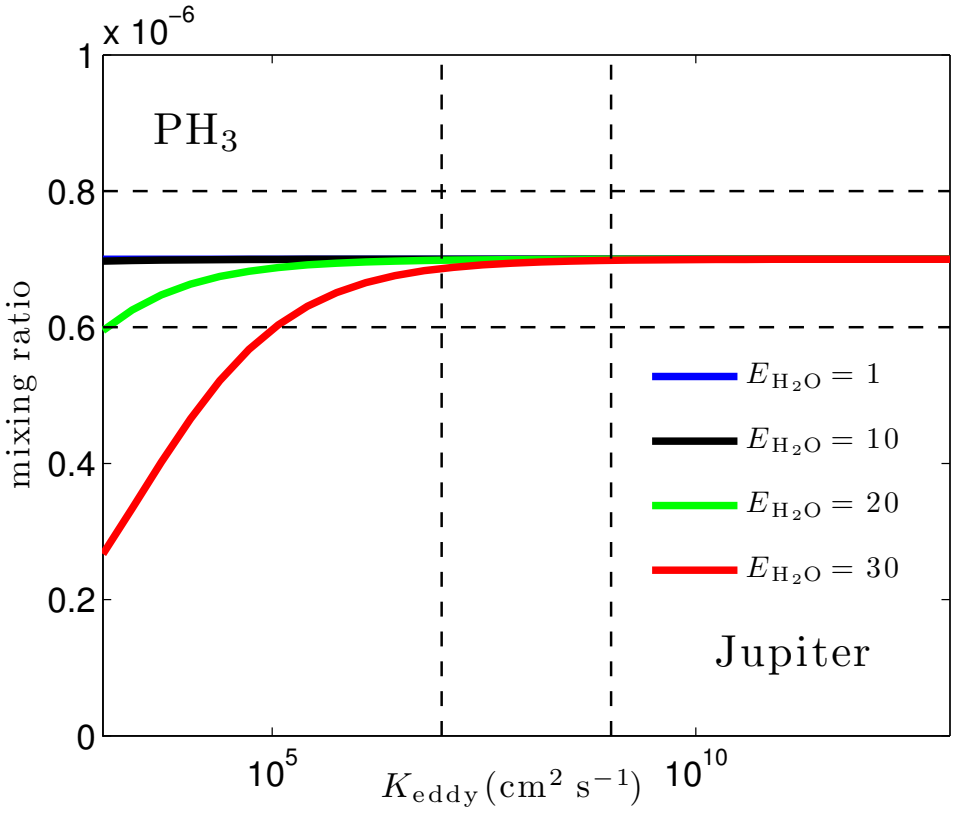

Figure 4.5 The predicted mixing ratio of PH_3 as a function of the vertical eddy diffusion coefficient $K_{\rm eddy}$ in Jupiter's atmosphere at a few bars level. The horizontal dashed lines show the range of observed PH_3 mixing ratio $q_{\rm PH_3} = 7.0 \pm 1.0 \times 10^{-7}$ [e.g., Irwin et al., 1998]. The vertical dashed lines show the range of plausible eddy diffusion coefficient.

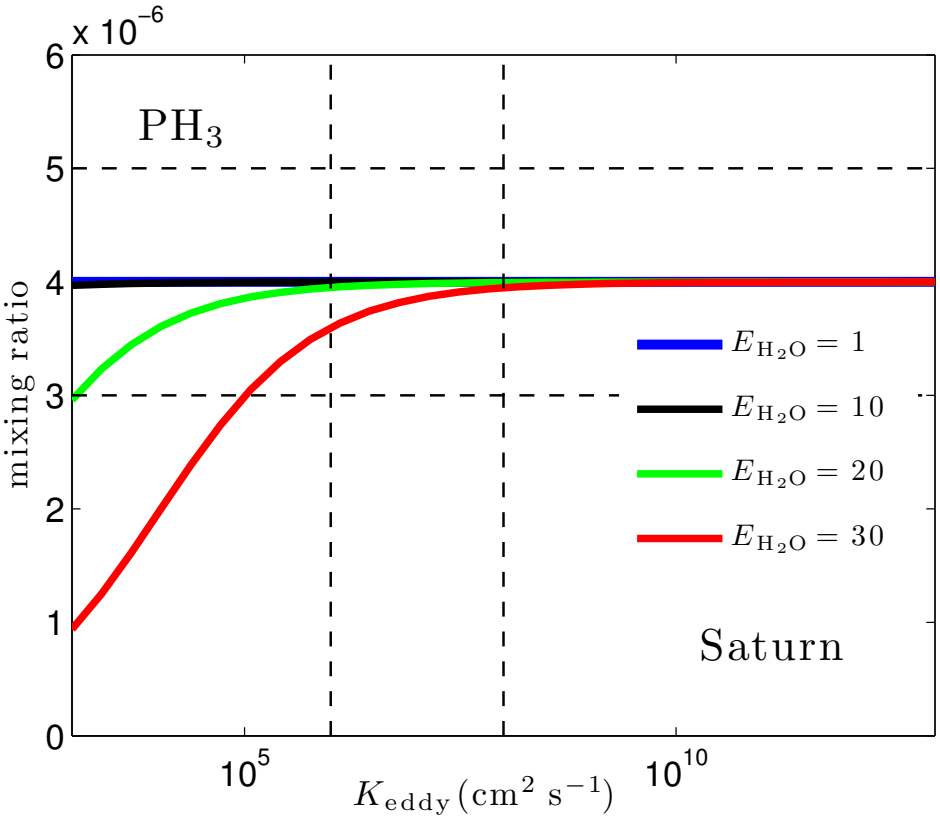

Figure 4.6 The predicted mixing ratio of PH_3 as a function of the vertical eddy diffusion coefficient $K_{\rm eddy}$ in Saturn's atmosphere at a few bars level.The horizontal dashed lines show the range of observed PH_3 mixing ratio $q_{\rm PH_3} = 4.0 \pm 1.0 \times 10^{-6}$ [e.g., Fletcher et al., 2011]. The vertical dashed lines show the range of plausible eddy diffusion coefficient.

Fegley and Lodders, 1994, Visscher and Fegley, 2005]. We find the difference is due to the different thermodynamic data used for P_4O_6. Fegley and Lodders [1994] and others use the standard enthalpy of formation of P_4O_6 ($\Delta H_f^0[P_4O_6]$) from JANAF table [Chase et al., 1985], which is based on the experiments by Koerner and Daniels [1952]. As a comparison, the CEA code uses the $\Delta H_f^0[P_4O_6]$ from Gurvich's table [Gurvich and Veyts, 1990], which is based on the experiments by Hartley and McCoubrey [1963]. Fegley and Lodders [1994] favored the data from the JANAF table because they see "no compelling reasons, such as a problem with experimental methods or data reduction, to reject the work of Koerner and Daniels [1952] in favor of the work of Hartley and McCoubrey [1963]". They point out that the discrepancy needs to be resolved by a new experimental determination of the $\Delta H_f^0[P_4O_6]$. However, we favor the data from Gurvich's table for the following reasons. Hartley and McCoubrey [1963] actually pointed out that in the experiment of Koerner and Daniels [1952] the sample examined is a mixture of P_4O_6 and P_4O_{10} rather than pure P_4O_6. The identification of P_4O_6 is not necessarily definitive and it may lead to the more negative values of the enthalpy of formation for P_4O_6 (due to pollution by P_4O_{10}). Later studies by Muenow et al. [1970] and Smoes and Drowart [1973] also supported the measurement by Hartley and McCoubrey [1963]. Quantum chemical calculations by Morgon [2012] get values of the enthalpy of formation of P_4O_6 that are closer to the values of Hartley and McCoubrey [1963]. We didn't find another direct or indirect measurement that supported the values by Koerner and Daniels [1952]. The Burcat database [Burcat and Ruscic, 2005] adopted the values by Hartley and McCoubrey [1963] and pointed out that the values used in JANAF is erroneous. For these reasons, we choose to take the data from Gurvich's table. Our computation shows that PH_3 is converted to H_3PO_4 at about

700 K in Saturn's atmosphere. From our computations for Jupiter, PH_3 is largely converted to H_3PO_4 at about 650 K in Jupiter's atmosphere.

The main chemical pathway for PH_3/H_3PO_4 conversion is identified from the H/P/O reaction network by comparing the rates of all the reactions in the network. This method is very robust since no information is needed other than the kinetic data. The details of our analysis are presented in the Appendix B. We find the main chemical pathway consists of the following reactions:

$$PH_3 \leftrightarrow PH_2 + H \tag{4.1a}$$

$$PH_2 + H_2O \leftrightarrow H_2POH + H \tag{4.1b}$$

$$H_2POH + PH_2 \leftrightarrow HPOH + PH_3 \tag{4.1c}$$

$$HPOH \leftrightarrow HPO + H \tag{4.1d}$$

$$HPO \leftrightarrow PO + H \tag{4.1e}$$

$$PO + H_2O \leftrightarrow HOPO + H \tag{4.1f}$$

$$HOPO + H \leftrightarrow PO_2 + H_2 \tag{4.1g}$$

$$PO_2 + H_2O \leftrightarrow HOPO_2 + H \tag{4.1h}$$

$$HOPO_2 + H_2O \leftrightarrow H_3PO_4 \tag{4.1i}$$

$$PH_3 + 4\,H_2O \leftrightarrow H_3PO_4 + 4H_2 \tag{4.1, net}$$

The rate determining step for the pathway is reaction (4.1h). The rate coefficient for this reaction is unknown, however, the backward reaction coefficient is estimated in Twarowski [1995]. For the reverse reaction of 4.1h, the rate coefficient $k_{4.1h,r} = 5.24 \times 10^{-11} e^{-6014/T}$ cm^{3}molecule^{-1}s^{-1}. Using the detailed

balance, the forward rate coefficient $k_{4.1h} = k_{4.1h,r}K_{4.1h,eq}$, where $K_{4.1h,eq}$ is the equilibrium constant of reaction (4.1h). Therefore, the forward rate coefficient is estimated to be $k_{4.1h} = 2.35 \times 10^{-12}e^{-1.067\times10^4/T}$ cm^{3}molecule^{-1}s^{-1}.

In Figures 4.5 and 4.6, we have plotted the predicted mixing ratios of PH_3 as a function of the $K_{\rm eddy}$ computed using the rate determining step. Our calculations show that the mixing ratio of PH_3 is not sensitive to the values of $K_{\rm eddy}$ unless $K_{\rm eddy}$ is less than 1×10^5 cm^{2}s^{-1}. We also compared the predicted PH_3 for different values of $E_{\rm H_2O}$. The mixing ratio of PH_3 is also not sensitive to the value of $E_{\rm H_2O}$ unless $E_{\rm H_2O}$ is greater than 30. PH_3's insensitivity to parameters is due to its quench level deep in the regime where it is the dominant species. For example, when $K_{\rm eddy}$ = 1×10^7 cm^{2}s^{-1} and $E_{\rm H_2O} = 10$, the quench level is at $T \approx 900K$. From our equilibrium calculations shown in Fig. 4.4, PH_3 is stable and dominant until below 700 K. Almost all the phosphorus is sequestered in PH_3 on Jupiter and Saturn.

4.4.3 Simulation results for SiH4

Figure 4.7 shows the predicted equilibrium abundances of some Si-bearing species along Saturn's adiabat computed using the NASA CEA code. The elemental abundances used in the calculations are summarized in Table 4.2. $MgSiO_3$ (l,s) and Mg_2SiO_4(s) condensate are the primary carriers of Si below 2000 K. The mixing ratio of SiH_4 is 1×10^{-9} at about 1500 K, and decreases to 1×10^{-18} at about 1000 K. The equilibrium results are in agreement with the results from Fegley and Lodders [1994]. Observationally, the upper limit for $q_{\rm SiH_4}$ on Jupiter is 2.5×10^{-9} [Treffers et al., 1978], and the upper limit for $q_{\rm SiH_4}$ on Sat-

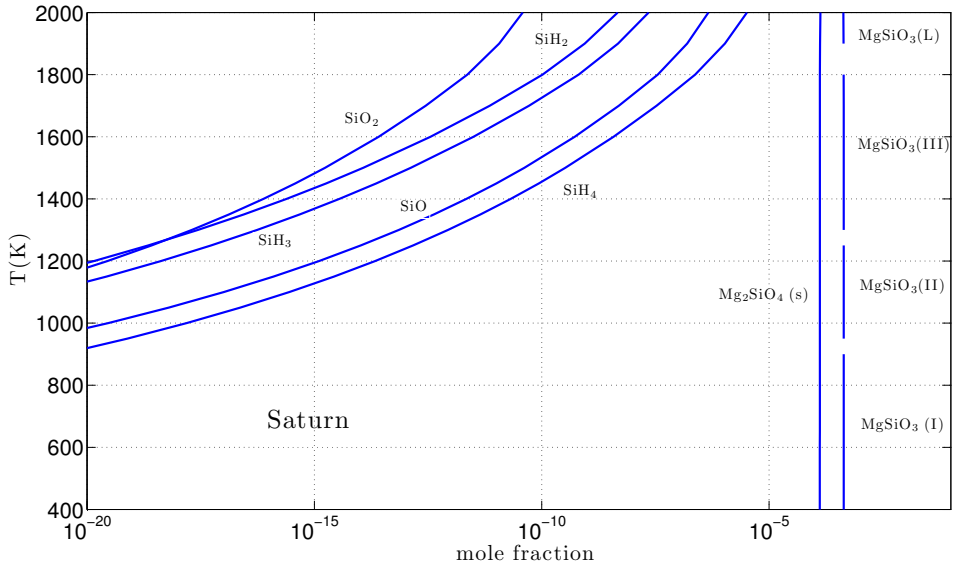

Figure 4.7 Equilibrium mole fractions of some Si-bearing species along Saturn's adiabat computed using the NASA CEA code. The elemental input we used are Si/H = 10 time solar, O/H = 10 times solar, and other elemental abundances are solar except He, C, N, S, P, Ge, and As, which are listed in table 4.2.

urn is 2.0×10^{-10} [Noll and Larson, 1991]. This indicates that almost all of the silicon on Jupiter and Saturn is removed by the rock formation and subsequent condensation. The total oxygen in Jupiter should be at least the oxygen locked in the rocks [e.g., Visscher and Fegley, 2005]. Since $MgSiO_3$(s) is the major condensates for silicon, each silicon atom is combined with three oxygen atoms. Assuming the total silicon enrichment relative to solar is similar to the enrichment for carbon, then Si/H is about 1.43×10^{-4} on Jupiter and 3.24×10^{-4} on Saturn. The oxygen locked with silicon therefore has a mixing ratio of $O/H > 4.4\times10^{-4}$ for Jupiter and $O/H > 1.0\times10^{-3}$ for Jupiter and Saturn, corresponding to about 0.9 and 2.0 times solar, respectively. Adding this part of oxygen and the oxygen sequestered in water would give the total oxygen in Jupiter and Saturn.

Thanks to the detailed kinetic data of Miller et al. [2004], we can extract the

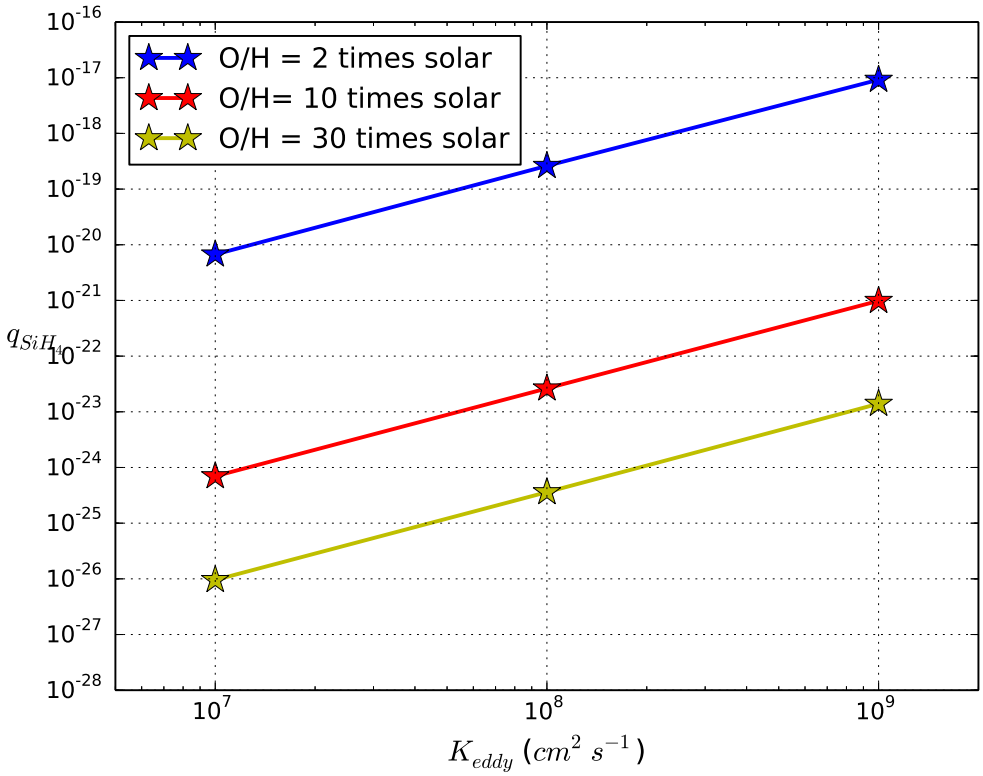

Figure 4.8 Predicted mixing ratio of SiH4 as a function of the vertical eddy diffusion coefficient $K_{\rm eddy}$ for Saturn. Different oxygen abundances are explored. Si/H = 10 times solar in the calculation.

main chemical pathway for SiH_4 destruction from the reaction network. The main chemical pathway is identified by comparing the rates of all the reactions in the network. The analysis is detailed in the Appendix C. The main chemical pathway of SiH_4 destruction is given by the following reactions:

$$SiH_4 + M \leftrightarrow SiH_2 + H_2 + M, \tag{4.2a}$$

$$SiH_2 + H_2O \leftrightarrow HOSiH + H_2, \tag{4.2b}$$

$$HSiOH \leftrightarrow SiO + H_2, \tag{4.2c}$$

$$SiO + H_2O \leftrightarrow Si(OH)_2, \tag{4.2d}$$

$$Si(OH)_2 + H \leftrightarrow HOSiO + H_2, \tag{4.2e}$$

$$Si(OH)_2 \leftrightarrow HSiO(OH) \tag{4.2f}$$

$$HSiO(OH) + H \leftrightarrow HOSiO + H_2, \tag{4.2g}$$

$$HOSiO \leftrightarrow SiO_2(cr) + H, \tag{4.2h}$$

$$SiO_2(cr) + Mg(OH)_2 \leftrightarrow MgSiO_3(s) + H_2O, \tag{4.2i}$$

$$SiH_4 + H_2O + Mg(OH)_2 \leftrightarrow MgSiO_3(s) + 4H_2. \tag{4.2, net}$$

The steps (4.2a) to (4.2h) are directly identified from the network, but the last step (4.2i) is added because SiO_2(cr) is not a stable product in the atmospheres of Jupiter and Saturn according our equilibrium calculations and those of Fegley and Lodders [1994]. A reaction incorporating Si into to $MgSiO_3$(s) completes the chemical pathway. Compared with the chemical path proposed in Fegley and Lodders [1994], the formation of SiH_2 and $MgSiO_3$(s) is the same, but the path from SiH_2 to SiO_2(cr) is different. The difference is due to the methodologies used to identify main chemical pathways. Fegley and Lodders [1994]

constructed their chemical pathway by identifying important intermediates observed in the experiments and then devising a pathway to connect the reactants, intermediates, and the products. There might be other important intermediates that are missing from the pathway, and the way of connection is not unique. This method is used when we do not have a reaction network or do not have enough kinetic data to perform detailed analysis. However, since we now have a reaction network, we can simulate the chemical evolution using the network and identify the fastest route from SiH_4 to SiO_2(cr). Our analysis is detailed in the Appendix C. Among the chemical pathway, we find reactions 4.2b, 4.2e, and 4.2g all serve as the bottlenecks. There is no unique rate limiting step for SiH_4 destruction.

This analysis helps us simplify the original H/Si/O reaction network from Miller et al. [2004]. The original network is designed for the simulation of SiH_4 burning in the molecular oxygen. Therefore, the composition is silicon-rich and oxygen-rich. However, the atmosphere of Jupiter and Saturn is hydrogen rich. Some species in the reaction network are expected to be unimportant in Jupiter and Saturn's atmosphere, and thus can be removed from the network to increase the efficiency of time integration. In the simplified reaction network, the species included are H_2, He, H_2O, OH, H, SiH_4, SiH_3, SiH_2, SiO, $Si(OH)_2$, HSiOH, HSiO(OH), HOSiO, and SiO_2(c). These species are the major intermediates for SiH_4 destruction, as is shown in Fig. C.1 in the Appendix C. This simplified reaction network is used to predict the abundance of SiH_4 along Saturn's adiabat for different values of $K_{\rm eddy}$ and $E_{\rm O}$. The results are presented in Fig. 4.8. For $E_{\rm O} = 2$ and $K_{\rm eddy}$ = 1×10^9 cm^2 s^{-1}, the predicted mixing ratio of SiH_4 at a few bars level is about 1×10^{-17}, while for $E_{\rm O} = 30$ and $K_{\rm eddy}$ = 1×10^7 cm^2 s^{-1}, the mixing ratio of SiH_4 falls to 1×10^{-26}. For the two extreme

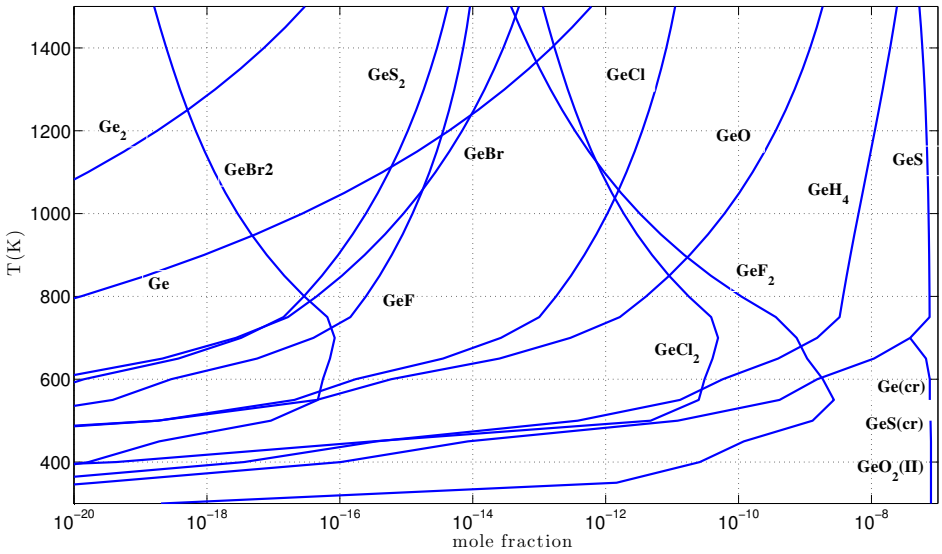

Figure 4.9 Equilibrium abundances of germanium containing species along Saturn's adiabat computed using NASA CEA code. We use Ge/H = 10 times solar, and O/H = 10 times solar. Other elemental abundances are also assumed to be solar except He, C, N, S, P, Si, and As, which are listed in table 4.2.

cases considered here, SiH_4 abundance is too small to be detected. Therefore, we conclude SiH_4 is not expected in Saturn's troposphere. The same analysis is applied to Jupiter. Similar to the result for Saturn, SiH_4 is also not expected in Jupiter's troposphere. Fegley and Lodders [1994]'s calculation for SiH_4 kinetics also concludes the low mixing ratio of SiH_4. We confirm this result using a new Si/H/O reaction network.

4.4.4 Simulation results for GeH4

In Fig. 4.9, we show the equilibrium abundances of germanium containing species along Saturn's adiabat computed using the NASA CEA code. The elemental abundances used in the calculations are summarized in Table 4.2. The

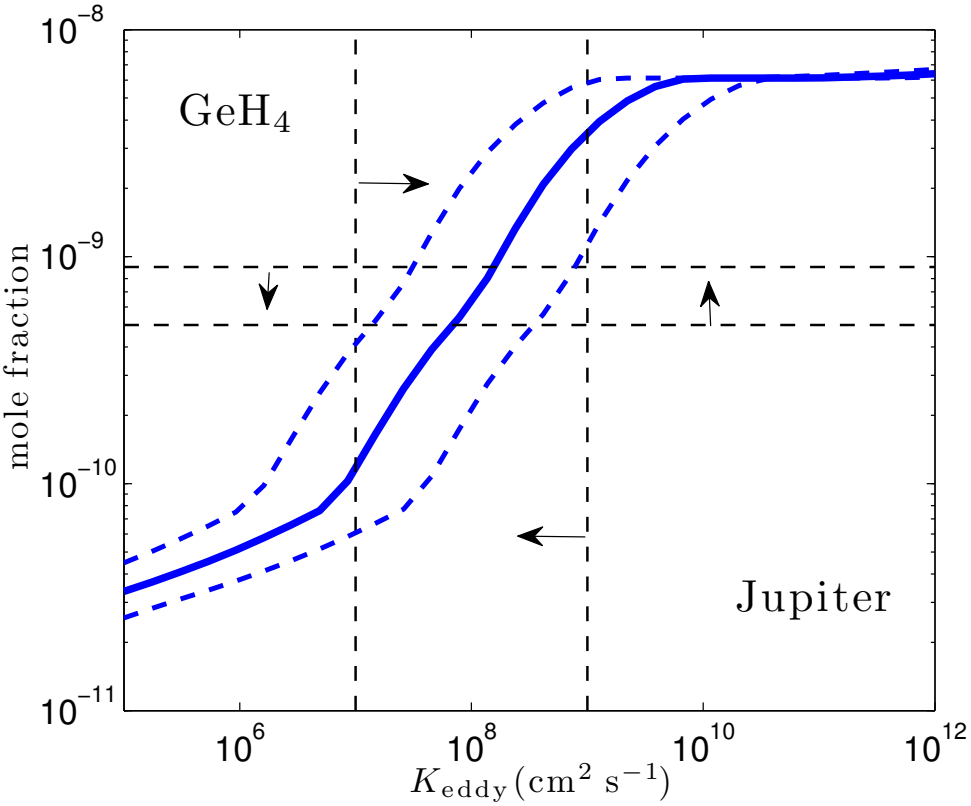

Figure 4.10 Predicted mole fraction of GeH_4 as a function of $K_{\rm eddy}$, the vertical eddy diffusion coefficient. The horizontal dashed lines show the range of observed mole fractions of GeH_4 [Bjoraker et al., 1986]. The vertical dashed lines show the plausible range of $K_{\rm eddy}$ for Jupiter. The blue dashed curves correspond to a factor of 5 uncertainty on both sides of the rate coefficient (total factor of 25).

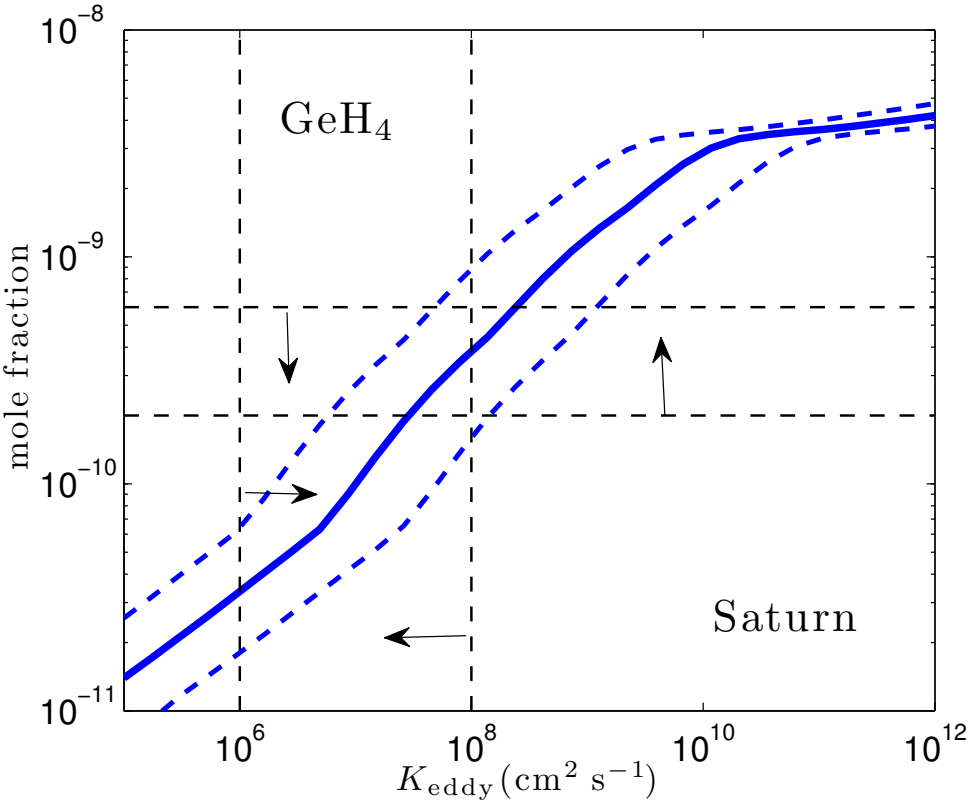

Figure 4.11 Predicted mole fraction of GeH_4 as a function of $K_{\rm eddy}$, the vertical eddy diffusion coefficient. The horizontal dashed line shows the observed range for X_{GeH_4}, which is $4\pm2\times10^{-10}$ [Noll et al., 1988]. The vertical dashed lines show the plausible range of $K_{\rm eddy}$ for Saturn. The blue dashed curves correspond to a factor of 5 uncertainty on both sides of the rate coefficient (total factor of 25).

figures show that GeH_4 is not the dominating germanium containing species, and it is converted to more abundant GeS at lower temperature. Condensation happens near 700 K, and the major condensates are Ge(cr), GeS(cr) and GeO_2(cr). There are limited data for the GeH_4 kinetics, therefore, we propose a chemical pathway for the conversion between GeH_4 and GeS by analogy with SiH_4 and SiO, since Si and Ge are in the same group and next to each other in the periodic table, and O and S are in the same group and also next to each other in the periodic table. The main chemical pathway for the conversion from SiH_4 to SiO is given by reactions 4.2a, 4.2b, and 4.2c. The rate determining reaction is 4.2b. By analogy, we propose the main chemical pathway below for the conversion from GeH_4 to GeS.

$$GeH_4 + M \leftrightarrow GeH_2 + H_2 + M, \tag{4.3a}$$

$$GeH_2 + H_2S \leftrightarrow HSGeH + H_2, \tag{4.3b}$$

$$HSGeH \leftrightarrow GeS + H_2, \tag{4.3c}$$

and the rate determining reaction is 4.3b. This chemical pathway is very similar to the one proposed in Fegley and Lodders [1994]. The only difference is the step from GeH_2 to HSGeH. In Fegley and Lodders [1994], two steps are used: the first is GeH_2 + $H_2S \leftrightarrow H_2Ge{=}S + H_2$, and the second is $H_2Ge{=}S \leftrightarrow HGe{=}SH$. In the H/Si/O reaction network, the rate coefficient for SiH_2 + $H_2O \leftrightarrow H_2Si{=}O$ + H_2 is $3.84 \times 10^{10} T^{-0.6} e^{-4905/T}$ $cm^3mol^{-1}s^{-1}$, and the rate coefficient for SiH_2 + $H_2O \leftrightarrow HSi{=}OH + H_2$ is $2.15{\times}10^{10} T^{0.7} e^{-4956/T}$ $cm^3mol^{-1}s^{-1}$ [Zachariah and Tsang, 1995]. At 800 K, the first reaction is much slower than the second reaction. By analogy, we therefore favor the single step from GeH_2 to HGe=SH proposed here instead of the double step proposed in Fegley and Lodders [1994].

The rate coefficient for the reaction 4.3b is not in the literature. Again by analogy with reaction SiH_2 + H_2O, we use $k_{4.3b} \approx 2.15\times10^{10}T^{0.7}e^{-4956/T}$ $cm^3mol^{-1}s^{-1}$ [Zachariah and Tsang, 1995]. The predicted mole fraction of GeH_4 as a function of the vertical eddy diffusion coefficient $K_{\rm eddy}$ is shown in Fig. 4.10 and 4.11 for Jupiter and Saturn, respectively. For Jupiter, our predicted mole fraction is consistent with the observed mixing ratio of $7^{+4}_{-2}\times10^{-10}$ by Bjoraker et al. [1986] with the values of $K_{\rm eddy}$ predicted by Wang et al. [2015]. For Saturn, our predicted mole fraction is also consistent with the observed value of $(4\pm2)\times10^{-10}$ by Noll et al. [1988]. This consistency indicates the rate coefficient of GeH_2 + H_2S is close to our estimate here. Within a factor 5 uncertainty on both sides of the rate coefficient (total factor of 25), we find the predicted mixing ratios of GeH_4 is in agreement with the observed values. Adjusting the rate coefficient even higher or lower will yield a disagreement between the prediction and the observation. Therefore, the rate coefficient of reaction 4.3b should be within a factor of 5 of our estimation. When we have an accurate measurement of the rate coefficient, we can use the GeH_4 abundance to constrain the value of $K_{\rm eddy}$. The sensitivity of GeH_4 abundance on the $K_{\rm eddy}$ implies the effectiveness of using GeH_4 abundances to constrain the $K_{\rm eddy}$, but the kinetics needs to be better constrained by laboratory measurements first.

4.4.5 Simulation results for AsH3

Equilibrium calculations show that AsH_3 is the dominant arsenic bearing species until it is converted to As_4 or As_2S_2 at about 400 K [Fegley and Lodders, 1994]. Due to the lack of kinetic data, it is quite uncertain where the quench level is. Fegley and Lodders [1994] proposed three possible chemical pathways

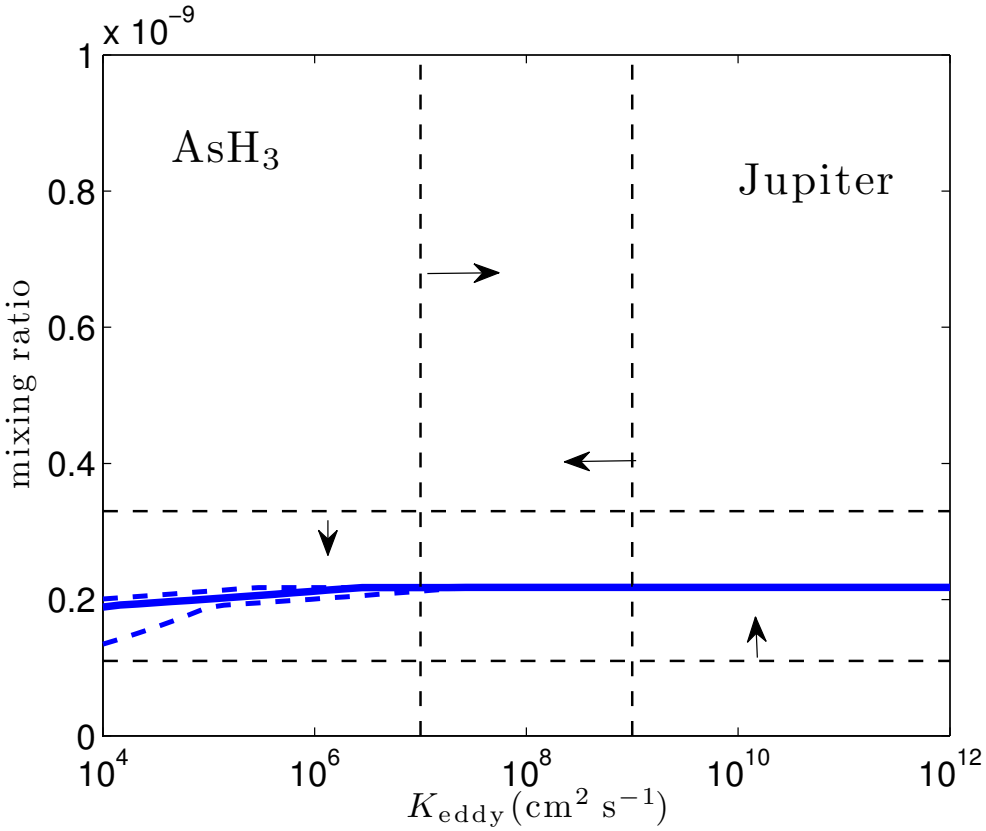

Figure 4.12 The predicted mixing ratio of AsH_3 as a function of $K_{\rm eddy}$, the vertical eddy diffusion coefficient. The horizontal dashed lines show the observed AsH_3 mixing ratio, $q_{\rm AsH_3} = 2.2 \pm 1.1 \times 10^{-10}$ [Noll et al., 1990]. The vertical dashed lines show the plausible range of $K_{\rm eddy}$ [Wang et al., 2015]. The observed abundance of AsH_3 corresponds to 0.3$\sim$0.8 times solar As/H ratio.

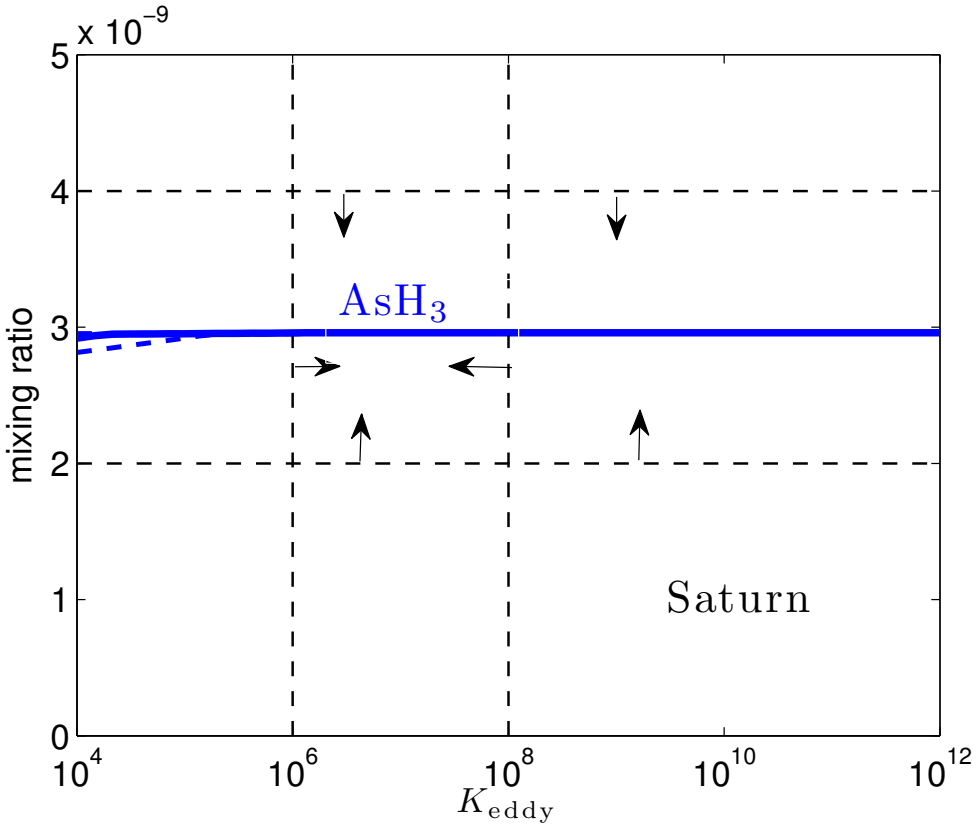

Figure 4.13 The predicted mixing ratio of AsH_3 as a function of $K_{\rm eddy}$, the vertical eddy diffusion coefficient. The horizontal dashed lines show the observed AsH_3 mixing ratio, $q_{\rm AsH_3}$ = 3±1×10^{-9} [Bézard et al., 1989, Noll et al., 1989, Noll and Larson, 1991]. The vertical dashed lines show the plausible range of $K_{\rm eddy}$ [Wang et al., 2015]. The observed abundance of AsH_3 corresponds to 5∼10 times enrichment relative to solar.

of the conversion from AsH_3 to As_4 or As_2S_2. The first pathway starts from the combination of AsH and AsH_3 forming As_2H_2, then As_2H_2 is decomposed into As_2 which combines to form the As_4 condensates. A similar mechanism starts from two AsH_2 forming the As_2H_2, and the rest is the same. The third one start from the combination of AsH with HS forming AsS, and two AsS combines to form the As_2S_2 condensates. The first and the third chemical pathway were investigated by Fegley and Lodders [1994]. The second one was not investigated because the authors do not have the thermodynamic data for AsH_2. However, the second pathway is more likely than the fist pathway since AsH_2 is expected to be more abundant than AsH. Now we study the second pathway, which is described by the following reactions:

$$AsH_3 + H \leftrightarrow AsH_2 + H_2, \tag{4.4a}$$

$$AsH_2 + AsH_2 \leftrightarrow As_2H_2 + H_2, \tag{4.4b}$$

$$As_2H_2 \leftrightarrow As_2 + H_2, \tag{4.4c}$$

$$As_2 + As_2 \leftrightarrow As_4, \tag{4.4d}$$

$$As_4 \leftrightarrow As_4(s), \tag{4.4e}$$

where the rate determining step is taken as the reaction 4.4b. The thermodynamic data for AsH_2 is from Tirtowidjojo and Pollard [1986]. The rate coefficient of the reaction 4.4b is taken as $4.63 \times 10^{-11} T^{0.04} e^{-16.8/T}$ cm^3 molecule^{-1} s^{-1}, by analogy with the rate coefficient of SiH_2 + SiH_2 [Dollet and de Persis, 2007]. The analogy between As and Si is probably not good, but we are forced by the lack of kinetic data for elements in the same column. We consider an overall two order of magnitude uncertainty for the rate coefficient. The kinetic results are shown in Fig. 4.12 and 4.13. From our calculations, the predicted AsH_3 abun-

dance is nearly equal to the total arsenic abundance for a large range of the $K_{\rm eddy}$. Now with the three chemical pathways studied, the conclusion is that AsH_3 abundance is not sensitive to the value of $K_{\rm eddy}$, and $AsH_3/H \approx As/H$ in both Jupiter and Saturn.

The AsH_3 is observed on Jupiter with a mixing ratio of $(2.2 \pm 1.1) \times 10^{-10}$ [Noll et al., 1990], corresponding to 0.3$\sim$0.8 times solar abundance. The AsH_3 is observed on Saturn with a mixing ratio of $(3 \pm 1) \times 10^{-9}$ [Bézard et al., 1989, Noll et al., 1989, Noll and Larson, 1991], corresponding to 5$\sim$10 times solar abundance. The higher enrichment of As on Saturn than on Jupiter is consistent with other elements, such as C and P. However, the subsolar As/H ratio on Jupiter is puzzling because other rock forming elements such as phosphorus and germanium are all enriched relative to solar [e.g., Fegley and Lodders, 1994]. There could be three possibilities. One is the observations have underestimated the AsH_3 abundance in Jupiter, and the AsH_3 abundance could be higher than solar. The second possibility is the observations are correct, but the kinetics are not. This may be hard to understand since the kinetics work well for Saturn. The third possibility is both observations and the kinetics are correct, and the subsolar abundance of As is realistic, but then a mechanism is needed to deplete arsenic on Jupiter. The JIRAM instrument on board Juno spacecraft has the capability of measuring the AsH_3 abundance at a few bars in Jupiter's atmosphere [Grassi et al., 2010]. However, to resolve this issue, experimental measurements on AsH_3 are necessary to better determine the arsenic kinetics.

4.5 Discussion

In section 4, we have presented our modeling results on the disequilibrium species using updated thermodynamic and kinetic data for Jupiter and Saturn. We have explored the dependence on the two free parameters in our model: the eddy diffusion coefficient and the deep water abundance. We find that CO and CO_2 are sensitive to both the eddy diffusion coefficient and the deep water abundance, while C_2H_6 and GeH_4 are only sensitive to the eddy diffusion coefficient. In this section, we discuss how Juno and a Saturn probe can improve our understanding on the $K_{\rm eddy}$ and $E_{\rm H_2O}$ through the measurement of disequilibrium species. We also discuss the uncertainties on the kinetic networks and suggest reactions that should be further studied.

4.5.1 Further constraints by Juno

Juno arrived at Jupiter in July 2016, and the microwave radiometer is mapping the water abundance down to $\sim$ 100 bars. The JIRAM instrument can measure the abundances of H_2O, NH_3, PH_3, CO, GeH_4, AsH_3 at a few bars level [Grassi et al., 2010]. Using the measured deep water abundance and the tropospheric CO abundance measured by Bézard et al. [2002], the eddy diffusion coefficient can be constrained as is shown by Fig. 4.2 in this paper and Fig. 5 in Wang et al. [2015]. Another constraint on the $K_{\rm eddy}$ can be placed using the measured GeH_4 abundance, as is shown by Fig. 4.10. However, a quantified reaction network is needed, or at least a determination of the rate limiting reaction is required to reduce the uncertainties in GeH_4 kinetics.

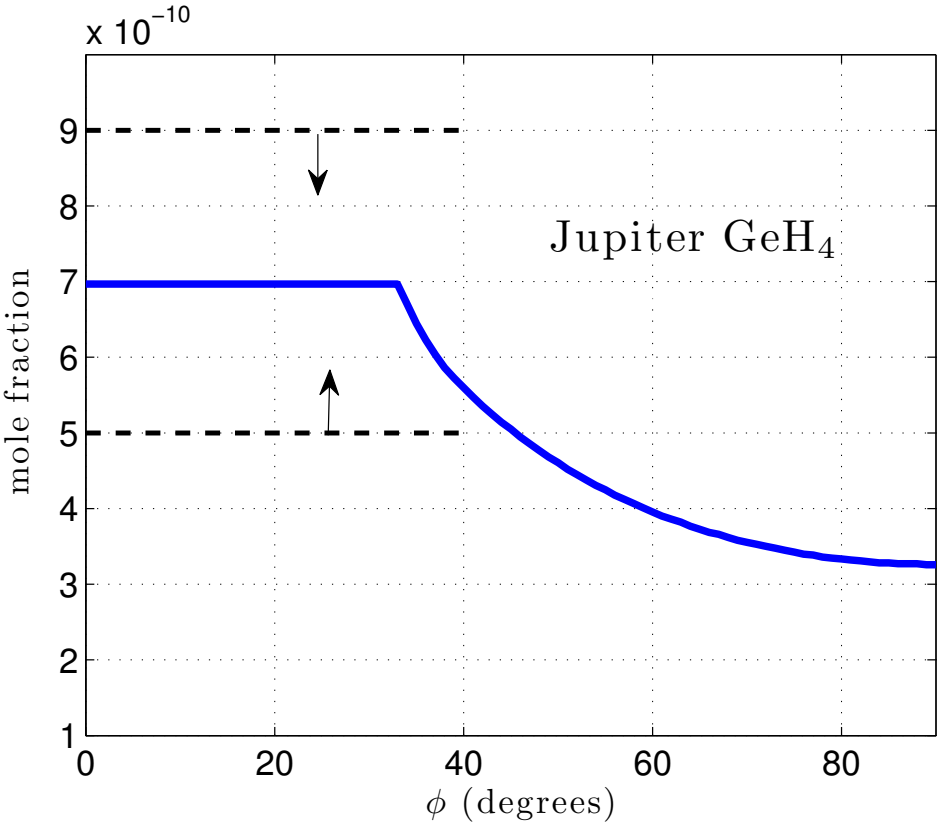

Figure 4.14 Mole fraction of GeH_4 as a function of the latitude for Jupiter computed using the germanium chemical model. The horizontal profile of the vertical eddy diffusion coefficient used in the calculation is from Wang et al. [2015]. The horizontal dashed lines show the average mole fractions of GeH_4 over longitude and over latitude between -40° and 40°, corresponding to a value of $7\pm2\times10^{-10}$ [Bjoraker et al., 1986].

Both Flasar and Gierasch [1978] and Wang et al. [2015] predicted latitudinal variations on the deep eddy diffusion coefficient due to the rotational effects on the convection. The latitudinal variation of the eddy diffusion coefficient should result in latitudinal variations of the abundances of CO, C_2H_6, CO_2, and GeH_4 at a few bars level. Multi-latitude measurements of CO and GeH_4 will test the prediction, if performed by JIRAM. We predict no latitudinal variation on the PH_3 and AsH_3 abundances since their abundances are not sensitive to the eddy diffusion coefficient. The horizontal (latitudinal) profile of CO on Jupiter is presented in the Fig. 9 of Wang et al. [2015]. The mole fraction of CO is predicted to be about 1×10^{-9} near the equator and decreases to about 4×10^{-10} near the pole. Fig. 10 of Wang et al. [2015] shows latitudinal variations of PH3 on Jupiter because the old chemical model is used in that paper. With the new chemical model for phosphorus in this paper, we predict no latitudinal variations for PH_3 at a few bars level. The predicted horizontal profile of GeH_4 is shown in Fig. 4.14. The horizontal profile of eddy diffusion coefficient used in the calculations is from Wang et al. [2015]. The mole fraction of GeH_4 is predicted to be about 7×10^{-10} near the equator and slowly decreases to about 3×10^{-10} near the pole.

4.5.2 Application to a Saturn entry probe

A Saturn entry probe with a mass spectrometer on board will be able to make in-situ measurements of the composition of Saturn, including the abundances of various disequilibrium species at a few bars level. The mass spectrometer is expected to have much higher resolution than the one on the Galileo entry probe. Therefore, it has the capability to make more precise and sensitive measurements. The probe may not be able to descend below the water cloud deck, and

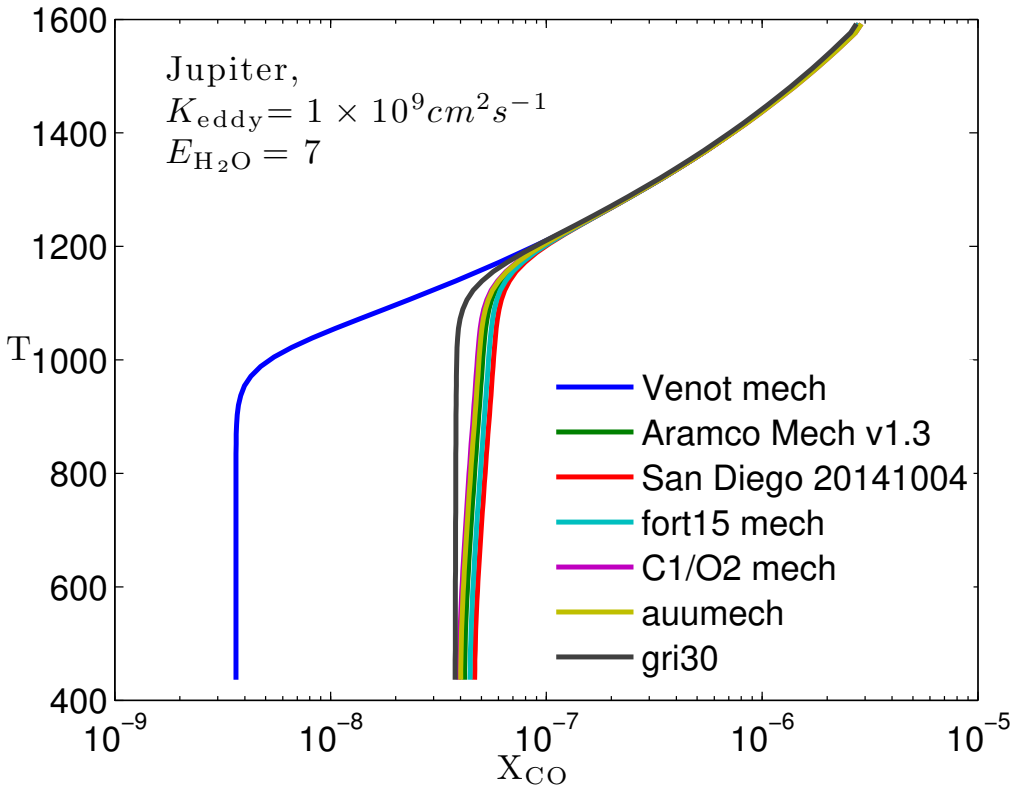

Figure 4.15 Comparisons on the the predicted mixing ratios of CO among various reaction networks from the combustion community. All the reaction networks shown here have been validated against many combustion experiments.

therefore cannot really determine the deep (global) water abundance. However, as is shown by Fig. 4.3, if both C_2H_6 and CO can be measured, useful constraints can be placed on both the eddy diffusion coefficient and the deep water abundance. The mixing ratio of C_2H_6 on Saturn is predicted to be about 1×10^{-9}, and the mixing ratio of the tropospheric CO is predicted to be below 1×10^{-9}. Therefore, any instrument must be sensitive enough to measure sub-ppb level of mixing ratios. In addition, since CO and N_2 have nearly identical molecular weight, the payload must resolve the ppb level CO from the ppm level N_2. In Wang et al. [2015], we predicted a higher eddy diffusion coefficient near the equator and a decreasing eddy diffusion coefficient at higher latitudes. Therefore, we expect CO and C_2H_6 to be higher in abundance near the equator. The probe entry site should be preferentially near the equator in order to maximize the possibility of detecting CO and C_2H_6. The mixing ratio of GeH_4 is predicted to be a few times 10^{-10}, and is a sensitive function of the eddy diffusion coefficient. The measurement of GeH_4 can add another constraint on the eddy diffusion coefficient.

The Juno mission measurements provide a potentially important synergy with the Saturn Probe measurements. By measuring both the deep water abundance and disequilibrium species, it will be possible to determine both the deep oxygen abundance and the magnitude of vertical eddy mixing. The latter determination is especially robust if the disequilibrium species are measured as a function of latitude [Wang et al., 2015]. Having a determination of the Jovian value of the eddy mixing will provide a useful constraint on that for Saturn, which will help lift the degeneracy between deep water abundance and vertical mixing from Saturn Probe measurements. Alternatively, if both CO and C_2H_6 can be measured by Saturn Probe, then an independent determination of the

eddy mixing from those measurements will allow comparison of the vertical dynamics from the hundreds of bars pressure level upward on the two planets. All of this depends on the ability to resolve the uncertainties in the kinetics.

4.5.3 Uncertainties in the kinetics

The uncertainties in the kinetics affect the constraints on both the eddy diffusion coefficient and the deep water abundance. In the planetary science community, various reaction networks have been developed for modeling many kinds of atmospheres, such as the atmosphere of Jupiter [Visscher et al., 2010], hot Jupiters [e.g., Moses et al., 2011, Venot et al., 2012, Miguel and Kaltenegger, 2014], terrestrial exoplanets [e.g., Hu and Seager, 2014] and brown dwarfs [Zahnle and Marley, 2014]. These reaction networks are successful in predicting the presence of major species in the atmospheres under a wide range of temperature and pressure conditions. However, the predicted mixing ratios are subject to large errors due to the large uncertainties on individual rate coefficients in the network. As an example, the CO/CH_4 chemistry has been studied for decades [e.g., Prinn and Barshay, 1977, Yung et al., 1988, Visscher and Moses, 2011], yet some uncertainty still remains because of reaction coefficients under debate [e.g. Moses, 2014]. The accuracy of most kinetic networks have yet to be tested by experiments except the one of Venot et al. [2012]. The Venot et al. [2012] network is derived from one in the combustion industry and has been validated against various combustion experiments. So is this reaction network accurate in modeling the atmospheres of giant planets? One concern is that the combustion experiments are usually conducted under carbon and oxygen rich environment, however, the atmo-

spheres of giant planets are extremely hydrogen-rich (Moses, personal communication, 2015). We investigated several other reaction networks developed in the combustion community. The reaction networks we investigated are: the "Aramco Mech v1.3" from Metcalfe et al. [2013]; the "San Diego Mechanism version 20141004" (`http://web.eng.ucsd.edu/mae/groups/combustion/mechanism.html`); the "C1/O_2 mechanism" from Li et al. [2007]; the "fort15 mech" from Sung et al. [1998]; the "aaumech" from Coda Zabetta and Hupa [2008]; and the "GRI-30 mech" from `http://www.me.berkeley.edu/gri_mech/`. All the reaction networks listed above have been validated against many combustion experiments. We applied these reaction networks to Jupiter's atmosphere and compared the predicted CO mixing ratios in Fig. 4.15. The predicted CO mixing ratios do not agree with each other, especially the Venot et al. [2012] network, which is predicting a much lower value than other networks. The source of the difference is that no other networks include the channel H + $CH_3OH \leftrightarrow CH_3 + H_2O$, which means this channel is not important for oxidation in an oxygen-rich environment. However, if this channel is indeed as fast as that measured in Hidaka et al. [1989] as used by the Venot et al. [2012] network, it can be crucial in determining the whole CO/CH_4 conversion rate. The comparison in Fig. 4.15 does not imply the Venot et al. [2012] network is wrong, but illustrates the point that networks validated under oxygen rich environments can give different results when applied to a hydrogen-rich environment. Ideally, networks should be tested by experiments conducted under hydrogen-rich conditions in order to improve their accuracy. In this paper, due to the unresolved uncertainties in kinetics, we considered two extreme cases for CO reaction networks. The Moses et al. [2011] reaction network represents the slowest pathway for CO destruction, while the Venot et al. [2012] model represents the fastest

pathway for CO destruction. In order to have more precise predictions on CO, C_2H_6 and GeH_4, a few reactions need to be further investigated experimentally or theoretically to determine their rate coefficients. For a tighter CO mixing ratio prediction, the reaction rate coefficient of H + $CH_3OH \leftrightarrow CH_3 + H_2O$ should be experimentally studied under conditions relevant to Jupiter and compared with the theoretical estimate by Moses et al. [2011], and the experimental estimate by Hidaka et al. [1989]. For a tighter C_2H_6 mixing ratio prediction, the rate coefficient of $CH_3 + CH_3 + M \leftrightarrow C_2H_6 + M$ under high pressure should be better determined. For a better GeH_4 mixing ratio prediction, the rate coefficient of $GeH_2 + H_2S \leftrightarrow$ HGe=SH + H_2 should be determined. The arsenic chemistry in a hydrogen rich environment should be studied to tighten the constraints on the total As abundance.

4.6 Conclusions

In this paper, we used a diffusion kinetic code developed in Wang et al. [2015] to predict the abundances of various disequilibrium species on Jupiter and Saturn with updated thermodynamic and kinetic data. The dependence on the vertical eddy diffusion coefficient and the deep water abundance have been explored. We summarize our simulation results below.

- We find C_2H_6 is a useful tracer for the deep eddy diffusion coefficient. The degeneracy between high (low) eddy diffusion coefficient and high (low) deep water abundance from CO constraints can be broken by adding the constraint by C_2H_6.

- We find PH_3 is converted to H_3PO_4 instead of P_4O_6 as in previous studies. We identified a new chemical pathway based on a H/P/O reaction network. The PH_3 abundance is predicted to be insensitive to either the eddy diffusion coefficient or the deep water abundance unless E_{H_2O} is higher than 20.
- We confirm that SiH_4 is not expected in the troposphere of either Jupiter or Saturn based on a H/Si/O reaction network. A new chemical pathway for $SiH_4/MgSiO_3$ (s) conversion is proposed.
- We propose a new chemical pathway for GeH_4 destruction. The GeH_4 abundance is predicted to be a sensitive function of the eddy diffusion coefficient.
- We confirm that the element As is primarily sequestered in AsH_3 in Jupiter and Saturn's atmosphere by exploring a new chemical pathway for AsH_3 destruction.
- Since the eddy diffusion coefficient is predicted by theoretical models to be latitudinally dependent, we predict the tropospheric abundances of CO, C_2H_6, CO_2, and GeH_4 to have latitudinal variations, and the tropospheric abundances of PH_3 and AsH_3 to have no latitudinal variations.

Juno can provide multiple constraints on the eddy diffusion coefficient from its measurement of disequilibrium species by JIRAM and its measurement of the deep water abundance from the microwave radiometer. A probe with a mass spectrometer sensitive enough to detect sub-ppb level of CO and C_2H_6 can place constraints on both the deep diffusion coefficient and the deep water abundance on Saturn. A probe should be sent to equatorial latitude to maximize the probability of detecting disequilibrium species. The predictions on the disequilibrium

chemistry are limited by the uncertainty in kinetics. Several reactions are worth further investigations to reduce the uncertainties and they are $H + CH_3OH \leftrightarrow CH_3 + H_2O$, $CH_3 + CH_3 + M \leftrightarrow C_2H_6 + M$, and $GeH_2 + H_2S \leftrightarrow HGe{=}SH + H_2$.

CHAPTER 5

MODELING SYNTHETIC SPECTRA FOR TRANSITING EXTRASOLAR GIANT PLANETS: DETECTABILITY OF H2S AND PH3 WITH JWST

5.1 Introduction

The atmospheres of exoplanets can be characterized by transit spectroscopy [e.g., Seager and Sasselov, 2000, Hubbard et al., 2001]. The transit spectra contain information about the composition and vertical thermal structure of the atmospheres. Interpretation of the transit spectra has led to the discovery of atoms like sodium, potassium [Charbonneau et al., 2002, Redfield et al., 2008, Jensen et al., 2011, Sing et al., 2012, 2015, Nikolov et al., 2014, Wilson et al., 2015], and molecules like water vapor [Deming et al., 2013, Huitson et al., 2013, Mandell et al., 2013, Crouzet et al., 2014, McCullough et al., 2014, Wakeford et al., 2013, 2017, Kreidberg et al., 2014b, 2015, Evans et al., 2016, Line et al., 2016] in the atmospheres of hot Jupiters. Other molecules such as CH_4, CO, CO_2 were also reported in the literature to be detected, however, the detection of these molecules are not confirmed by later observations or other retrieval techniques [e.g., Gibson et al., 2011, Hansen et al., 2014, Line et al., 2014]. Currently, the determination of molecular abundances is limited by the quality of the transit spectra [Burrows, 2014].

James Webb Space Telescope (JWST)'s large aperture (6.5 m), wide wavelength coverage (λ = 0.6 $\sim$ 28 μm) and multiple instrument modes will ensure that it will collect the highest quality transit spectra [e.g., Beichman et al., 2014]. Greene et al. [2016] simulated how well JWST observations can constrain the temperature-pressure profile and molecular abundances of H_2O, CH_4, CO, CO_2

and NH_3. Other molecules such as H_2S and PH_3 are not included in their calculations. However, H_2S and PH_3 are the primary carriers of sulfur and phosphorus in hydrogen-rich atmospheres [e.g., Visscher et al., 2006], and they potentially contribute to the absorptions in the transit spectra.

PH_3 has been observed in the atmospheres of Jupiter and Saturn [e.g. Fletcher et al., 2009a, and references therein]. The PH_3 observed in the upper troposphere and stratosphere is supplied by the vertical convection from deeper and hotter regions of the atmosphere where PH_3 is thermochemically stable. The same process may be at work in the exoplanets. H_2S was measured in the troposphere of Jupiter by the Galileo entry probe[Irwin et al., 1998, Wong et al., 2004]. H_2S is the primary carrier of sulfur in the atmospheres of Jupiter and Saturn except above a few bars level where H_2S is removed by forming the NH_4SH cloud. For exoplanets with higher stellar irradiation, H_2S may not condense in the upper atmosphere. Therefore, H_2S can potentially contribute to the transit spectra of extrasolar giant planets.

The non-equilibrium chemistry of phosphorus species was not explored in the context of exoplanets with hydrogen-rich atmospheres in the literature. The vertical mixing can drive the chemistry out of equilibrium, just like the case in Jupiter and Saturn. Non-equilibrium chemistry of sulfur in extrasolar giant planets was studied by Zahnle et al. [2009]. From their calculations, H_2S is predicted to be the primary carrier of sulfur up to $\sim$ 10 mbar. Above 10 mbar, photochemistry is at work and the abundance of H_2S decreases at higher altitude.

In this paper, we model the non-equilibrium chemistry of phosphorus in the hydrogen-rich atmospheres of exoplanets. We also model the non-equilibrium

chemistry of C/N/O/S bearing species in order to get the vertical profiles of major molecules in the atmospheres. To evaluate whether H_2S and PH_3 can be detected by JWST transit observations, we modeled the synthetic transmission and emission spectra from a single transit event observation with simulated noise levels.

The paper is organized as the follows. In section 5.2, we describe our chemical model, synthetic spectra model, and JWST noise model. In section 5.3, we present our results on the computed abundance profiles of major C/N/O/S/P bearing species. In section 5.4, we present the synthetic transit spectra for four planetary systems with different levels of stellar insolation. In section 5.5, we add simulated JWST noise into the synthetic spectra, and evaluate the detectability of H_2S and PH_3. In section 5.6, we discuss the implications for JWST transit observations, and limitations of our model. In section 5.7, we present the conclusions of this paper.

5.2 Methodology

In this section, we describe our methodology for modeling the synthetic JWST transit spectra. We first model the chemistry of C/N/O/S/P and identify major species in the atmospheres that are abundant and thus potentially important for the opacity. Then we model the noiseless primary and secondary transit spectra using the computed abundance profiles. Finally we model the transit spectra with simulated JWST noise, and determine whether certain molecules will be spectroscopically detectable by JWST. We detail our methodologies in what follows.

5.2.1 Chemical model

We use a one-dimensional diffusion-kinetic model developed in Wang et al. [2015, 2016] to compute the vertical profiles of molecular abundances. The code solves the equation

$$\frac{\partial Y_i}{\partial t} = \frac{1}{\rho}\frac{\partial}{\partial z}(\rho K_{\rm eddy}\frac{\partial Y_i}{\partial z}) + P_i - L_i, \tag{5.1}$$

where Y_i is the mass fraction of species i, ρ is the density of the atmosphere, z is the vertical coordinate, $K_{\rm eddy}$ is the vertical eddy diffusion coefficient, P_i is the chemical production rate of species i, and L_i is the chemical loss rate of species i. Two physical processes are modeled by the equation. One is the chemical production or loss of species i, and the other is the vertical transport of species i. The mixing ratio of species in the atmospheres is determined by the dynamic balance between these two physical processes. We neglect the effect of photochemistry. The effect on the chemical abundances is the photo-dissociation of hydrogen-bearing species (e.g., H_2O, CH_4, NH_3) and the production of photochemical products (e.g., C_2H_6, C_2H_2, HCN) [Moses et al., 2011, 2013, Venot et al., 2012, Kopparapu et al., 2012, Agúndez et al., 2014, Miguel and Kaltenegger, 2014]. Photochemistry changes the abundances only in the upper atmosphere that is at millibar levels. Therefore, we expect our computed abundance profiles are valid below $\sim$ 10 mbar.

The diffusion-kinetic model requires three kinds of input. First is the temperature-pressure ($T-P$) profile; second is a list of thermodynamic properties and a list of reactions between these species; third is the elemental compositions and the eddy diffusion coefficient. We detail how we choose the inputs below.

- $T - P$ profile: we compute the $T - P$ profile using the model developed in Parmentier and Guillot [2014], Parmentier et al. [2015], which is a non-gray analytical model.
- Thermodynamic properties and reaction rates: the thermodynamic properties are used to compute the equilibrium abundances as well as the backward reaction rates. The thermodynamic properties are compiled from Burcat and Ruscic [2005], McBride et al. [1993], Dean and Bozzelli [2000], and Venot [2012]. The kinetic network used for modeling the C/N/O/H chemistry is consisting of 108 species and 1000 reactions, originally from Venot et al. [2012]. The H/P/O reaction network consists of 24 species and 175 reactions, originally from Twarowski [1995]. A more detailed description of the C/N/O/H and H/P/O reaction networks used in this paper can be found in Wang et al. [2016], and both reaction networks can be downloaded at the KIDA database (`http://kida.obs.u-bordeaux1.fr/networks.html`).
- Elemental abundances: we assume the elemental composition of the atmosphere is solar. The solar elemental abundances are from Asplund et al. [2009].
- Eddy diffusion coefficient: $K_{\rm eddy}$ is used in the one-dimensional chemical models for parameterizing the vertical transport. There is no observational constraint on the eddy diffusion coefficient on exoplanets. However, its values can be approximated by multiplying the vertical convective velocity derived from 3-D General Circulation Models (GCM) with the pressure scale height [e.g., Moses et al., 2011, Venot et al., 2012, Parmentier et al., 2013]. This mixing length theory approximation has an uncertainty on the order of 10 in the estimated eddy diffusion coefficient [Smith, 1998].

In this paper, we choose to use a constant profile for the $K_{\rm eddy}$, with values equal to 1×10^9 cm^2 s^{-1} throughout the atmospheres. Moses et al. [2011] computed the abundances of C/N/O/H bearing species in HD209458b and HD189733b for a range values of eddy diffusion coefficient. The resulted differences in the molecular abundances are between a factor of one to five for different species.

In each simulation, we provide the elemental abundances, the $K_{\rm eddy}$, and the $T-P$ profile to set up the code, then we initialize the Y_i of species with chemical equilibrium mass fractions. The Y_i are evolved towards a steady state where the diffusion terms balance the chemical production/loss terms in equation (5.1). The output is vertical profiles of Y_i for each species in the model.

5.2.2 Synthetic spectra model

To simulate the synthetic spectra of transiting exoplanets, we modified the Smithsonian Astrophysical Observatory 1998 (SAO98) radiative transfer code (see Traub and Stier [1976], Traub and Jucks [2002], Kaltenegger and Traub [2009] and references therein for details). The line-by-line radiative transfer code calculates the atmospheric emergent spectra and also transmission of stellar radiation through the atmosphere with disk-averaged quantities at high spectral resolution. The atmosphere is divided in different layers, where the transmission is calculated using Beer's law. Updates include a new database with molecules relevant for giant planets that include H_2O, CH_4, CO, CO_2, NH_3, N_2, HCN, PH_3, H_2S taken from HITRAN [Rothman et al., 2013] and HITEMP [Rothman et al., 2010] database.

The overall high-resolution spectrum is calculated with 0.1cm^{-1} wavenumber steps. We also smear them out to a resolving power of 100 to simulate the resolution that we will obtain with the MIRI instrument at JWST. The smoothing was done using a triangular smoothing kernel.

5.2.3 JWST noise model

Table 5.1 Parameters for computing noise - extension of Table 4 in Greene et al. [2016]

Instrument	Mode	Optics	λ (μm)	native R	$A_{\rm pix}$ (arcsec^2)[a]	$n^b_{\rm pix}$	b (e$^-$ s^{-1} arcsec^{-2})[c]	N_d	$n_{\rm ints}$	noise floor (ppm)[d]
NIRISS	bright SOSS	GR700XD	1−2.5	∼700	0.065″×0.065″	∼50	627.61	∼18	∼1×10^4	20
NIRCam	LW grism	F322W2	2.5−3.9	∼1700	0.064″×0.064″	∼4	203.62	∼18	∼1×10^4	30
NIRCam	LW grism	F444W	3.9−5.0	∼1700	0.064″×0.064″	∼4	308.74	∼18	∼1×10^4	30
MIRI	Slitless	LRS prism	5.0−11.0	∼100	0.110″×0.110″	∼4	5156.0	∼28	∼1×10^4	50

[a] http://www.stsci.edu/jwst/instruments/
[b] two times the spatial extent of point source spectrum
[c] The background photon rate is computed at the JWST exposure time calculator https://demo-jwst.etc.stsci.edu/
[d] The adopted noise floor values are from Greene et al. [2016]

The noise of primary and secondary transit spectra is simulated following the recipes in Greene et al. [2016]. Here we provide a compact summary of the noise modeling methodology, along with parameters in the model, summarized in Table 5.1. The selected JWST observing modes are from Table 4 of Greene et al. [2016]. The NIRISS instrument with bright SOSS mode covers the wavelength 1.0 $\sim$ 2.5 μm with a native resolution of $\sim$ 700; the NIRCAM instrument with LW grism mode covers the wavelength 2.5 $\sim$ 5.0 μm with a native resolution of $\sim$ 1700; the MIRI instrument with slitless mode covers the wavelength 5.0 $\sim$ 12 μm with a resolution of $\sim$ 100. We adopted a cutoff at 12 μm for MIRI slitless mode because the transmission becomes low at longer wavelength [Kendrew et al., 2015]. The selected JWST modes provide a wavelength coverage between 1.0 and 12 μm. We choose a binned resolution of R = 100 for all modes to ensure each bin contains enough photon in our simulation.

There are four noise components: the signal photon shot noise, the background photon shot noise, the detector noise, and the systematic noise. The equations for computing each component are from Greene et al. [2016]. For completeness, we present these equations below, and describe how we choose the parameter values in these equations.

- The number of signal photons in each spectral bin is computed following the equation

$$S_\lambda = F_\lambda A_{\rm tel} t \frac{\lambda^2}{hcR} \tau, \tag{5.2}$$

  where S_λ is the number of signal photons in each spectral bin, F_λ is the flux of the signal as received at the telescope, $A_{\rm tel}$ is area of the aperture of JWST, t is the total integration time, R is the binned spectral resolution, and τ is the total system transmission. The total integration time t is adopted as 0.9 times the full transit duration T_{14}. The transmission τ is computed as the product of the telescope ($\sim$ 0.9) and selected instrument ($\sim$ 0.3). The signal flux F_λ is measured at three configurations, namely, in-transit, out-transit, and in-eclipse. We assume the total integration time for the three configurations are all equal to t. The signal shot noise is equal to the square root of S_λ.

- The background signal is computed following the equation

$$B_\lambda = b_\lambda t A_{\rm pix} n_{\rm pix} R_{\rm native} / R, \tag{5.3}$$

  where B_λ is the background photon numbers in each spectral bin, b_λ is the background electron flux, $A_{\rm pix}$ is the area subtended by each pixel, $n_{\rm pix}$ is two times the number of spacial pixels covered by the spectrum, and $R_{\rm native}$ is the native resolution of the spectrum before binning. The values

of above parameters used in this simulation are summarized in Table 5.1. The background shot noise is equal to the square root of B_λ.

- The total detector noise in single transit observation is calculated as

$$N_{\rm d,tot} = N_d \sqrt{n_{\rm pix} n_{\rm ints} R_{\rm native}/R}, \tag{5.4}$$

where N_d is the total detector noise in one integration, and $n_{\rm ints}$ is the number of integrations in one transit observation. The parameter $n_{\rm ints}$ depends on the total transit duration, the brightness limit of each instrument mode, and the brightness of the star. The parameter values are summarized in Table 5.1.

- The systematic noise cannot be reduced by summing over more observations. We adopted the systematic noise floor as suggested by Greene et al. [2016], as presented in Table 5.1.

The four noise components are combined quadratically to compute the total noise in each spectral bin for a single transit observation.

5.3 Results for abundance profiles

In this section, we present our results for the chemistry of C/N/O/S/P species. Temperature and pressure are the most important factors for determining the molecular abundances. The chemistry is very different for differently irradiated atmospheres. We simulate the atmospheres with different equilibrium temperatures (500 K, 750 K, 1000 K, 1500 K, 2000 K). The T-P profiles used in the calculations are shown in Fig. 5.1. The vertical eddy diffusion coefficient used is $1{\times}10^9$ cm^2 s^{-1}, and the composition is assumed to be solar. In the following

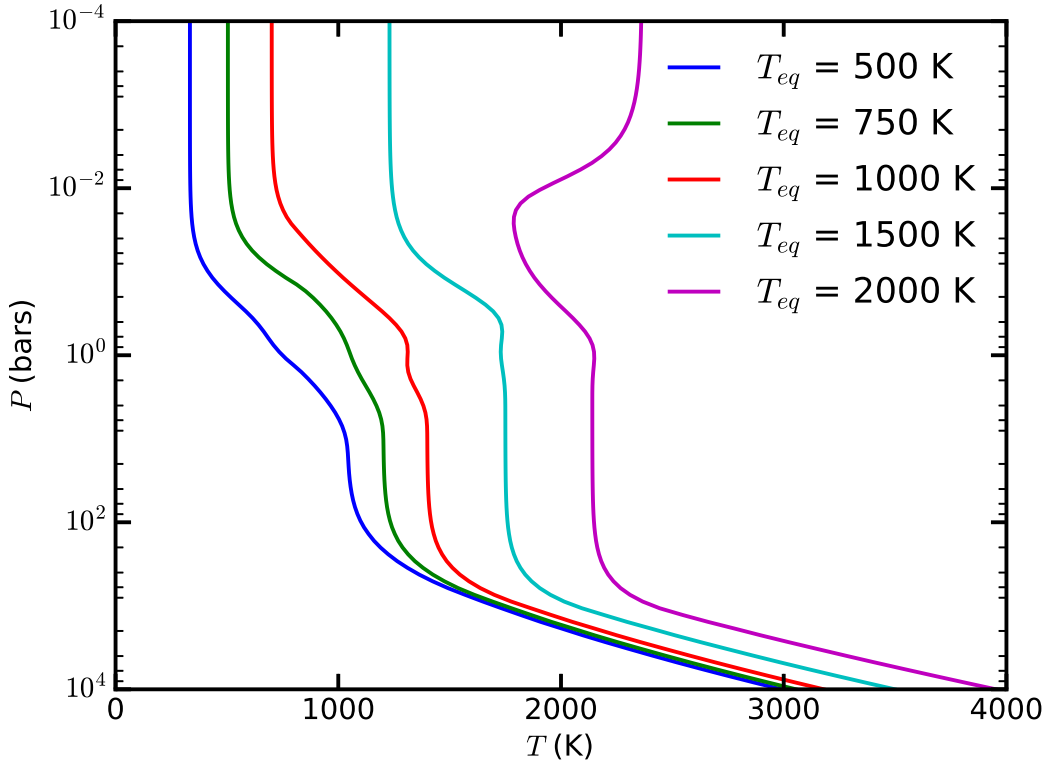

Figure 5.1 Horizontally-averaged temperature-pressure profile for extrasolar giant planets computed using the approach in Parmentier and Guillot [2014], Parmentier et al. [2015]. Different lines correspond to different equilibrium temperatures, caused by the irradiation from the star.

subsections, we present the computed vertical abundance profiles for $T_{\rm eq}$ = 500 K, 1000 K, 1500 K, and 2000 K.

5.3.1 Results for phosphorus species

Assuming a solar elemental abundances for phosphorus, hydrogen, and oxygen, we compute the abundance profiles of H/P/O bearing species for different levels of insolation. We present our results for the phosphorus chemistry in Fig. 5.2. The most abundant H/P/O bearing species are PH_3, PH_2, PH, HOPO, H_3PO_4, and P_2. For atmospheres with $T_{\rm eq}$ = 500 K and $T_{\rm eq}$ = 1000 K, the abundances are out of chemical equilibrium due to the effect of vertical mixing. For atmospheres with $T_{\rm eq}$ = 1500 K and $T_{\rm eq}$ = 2000 K, the abundances are in chemical equilibrium. The vertical mixing still exists, however, the mixing time scale is longer than the chemical timescale, and the abundances quickly re-equilibrate after mixing. The major phosphorus species are different for different levels of insolation. For an atmosphere with $T_{\rm eq}$ = 500 K, the dominant phosphorus-containing species is PH_3. This is similar to Jupiter, which has an equilibrium temperature at approximately 160 K. For an atmosphere with $T_{\rm eq}$ = 1000 K, PH_3 and P_2 are the most abundant phosphorus containing species above 1 bar. Below 1 bar, PH_3 is still the dominant species. At this temperature, part of the PH_3 is thermally decomposed into PH_2. The reactions between radicals can produce molecules with two or more phosphorus atoms such as P_2. At $T_{\rm eq}$ = 1500 K and 2000 K, the temperature is high enough that most PH_3 is thermally decomposed into PH_2 and PH.

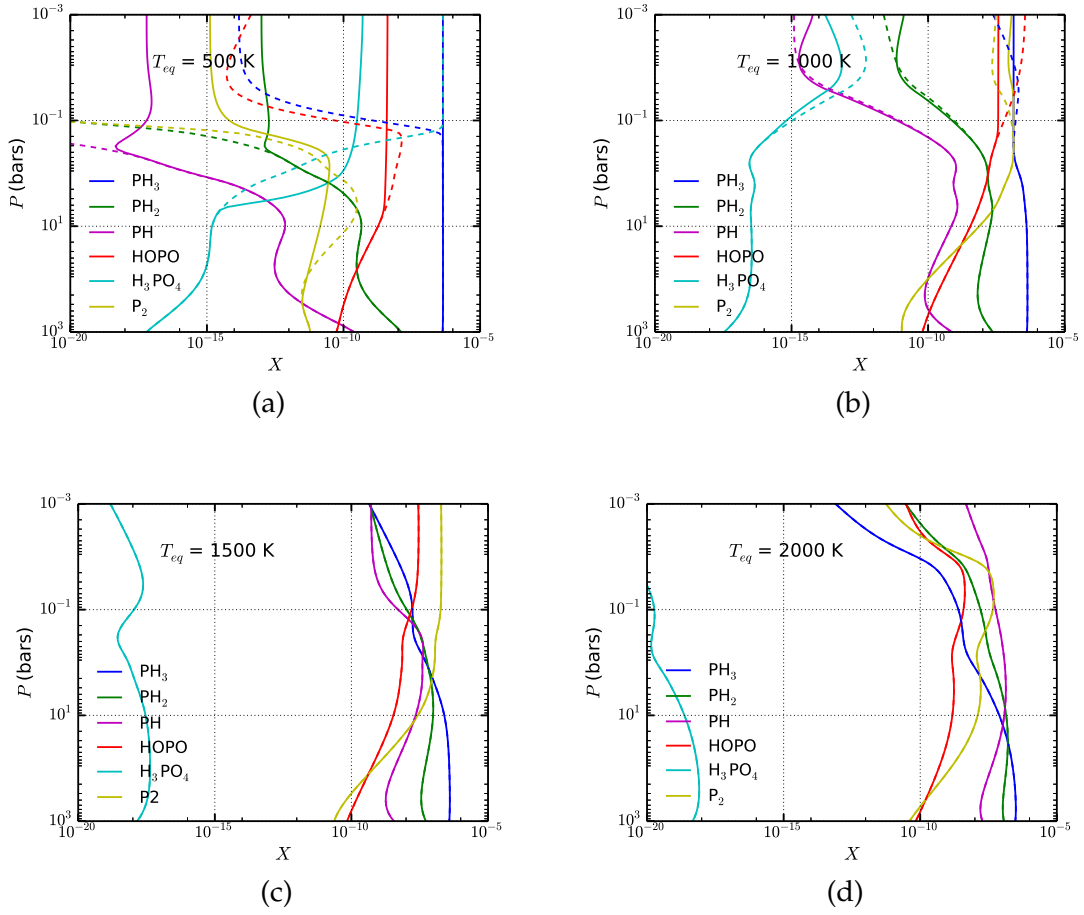

Figure 5.2 Computed mole fractions of major phosphorus-bearing species (PH_3, PH_2, PH, HOPO, H_3PO_4, and P_2) in the atmospheres of extrasolar giant planets. Solid lines show the disequilibrium abundances computed using the diffusion-kinetic model, and the dashed lines show the abundances assuming local chemical equilibrium. The four plots correspond to different equilibrium temperatures: (a) $T_{\rm eq}$ = 500 K, (b) $T_{\rm eq}$ = 1000 K, (c) $T_{\rm eq}$ = 1500 K, (d) $T_{\rm eq}$ = 2000 K. The elemental abundances are summed to be one solar. The eddy diffusion coefficient $K_{\rm eddy}$ is set at 1×10^9 cm^{2}s^{-1}.

5.3.2 Results for sulfur species

We compute the equilibrium abundances of sulfur species along the T-P profile in order to identify the most abundant sulfur bearing species. We consider species H_2S, HS, H_2S_2, CH_3SH, S, S_2, SO, SO_2, CS, CS_2, COS, and SN. The results are shown in Fig. 5.3. For atmospheres with $T_{\rm eq} = 500$ K, 1000 K, and 1500 K, H_2S is the dominant species at pressure levels between 1×10^{-4} bar and 1×10^{4} bar. For atmospheres with $T_{\rm eq} = 2000$ K, H_2S is the dominant species below 0.01 bar. Above 0.01 bar, atomic S is the dominate species. Since vertical mixing has the effect of homogenizing the abundances, the addition of vertical mixing into the model is not expected to change the result for H_2S. However, we ignore the effect of photochemistry, which may affect the vertical profile at low pressure levels. Zahnle et al. [2009]and Zahnle and Marley [2014] have done photochemical modeling of sulfur species in the atmospheres of hot Jupiters. From their calculations, H_2S is largely photo-dissociated at $P \gtrsim 0.01$ bar, but remains the dominant sulfur carrier at $P \lesssim 0.01$ bar. Therefore, it is reasonable to assume H_2S is the dominant sulfur bearing species below 0.01 bar.

5.3.3 Results for C/N/O/H species

It is necessary to carefully model the contribution of C/N/O/H bearing species to the transit spectra if we want to identify spectral features of H_2S and PH_3. Molecules such as H_2O or CO are more abundant than H_2S and PH_3, and thus contribute the most to the transit spectra. In order to find molecules that are more abundant than H_2S and PH_3, we performed independent calculations for C/N/O/H chemistry. Our results are in general consistency with results re-

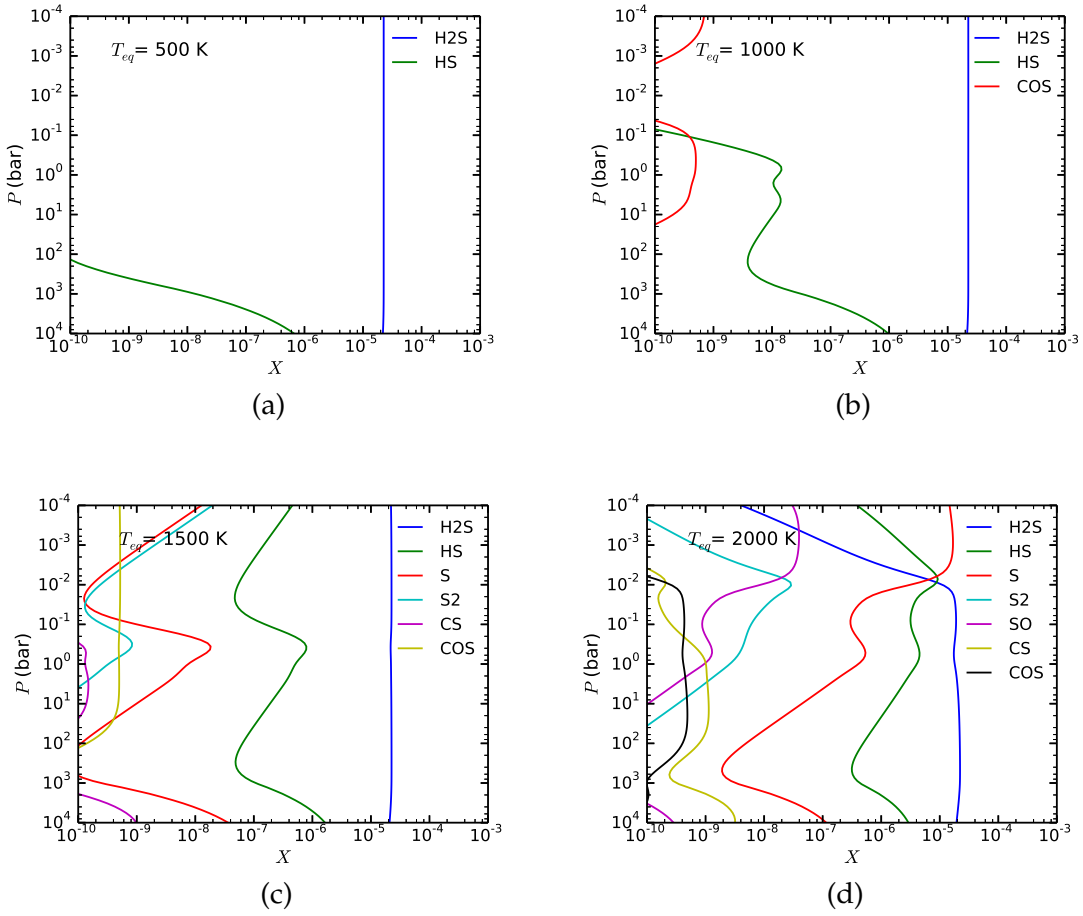

Figure 5.3 Computed equilibrium mole fractions of major sulfur-bearing species in the atmosphere of extrasolar giant planets. The disequilibrium calculations including vertical mixing are not done since the vertical mixing is not expected to change the profiles of H_2S. The four plots correspond to models with different equilibrium temperatures: (a) $T_{\rm eq} = 500K$, (b) $T_{\rm eq} = 1000K$, (c) $T_{\rm eq} = 1500K$, (d) $T_{\rm eq} = 2000K$. The elemental abundances used here is one solar.

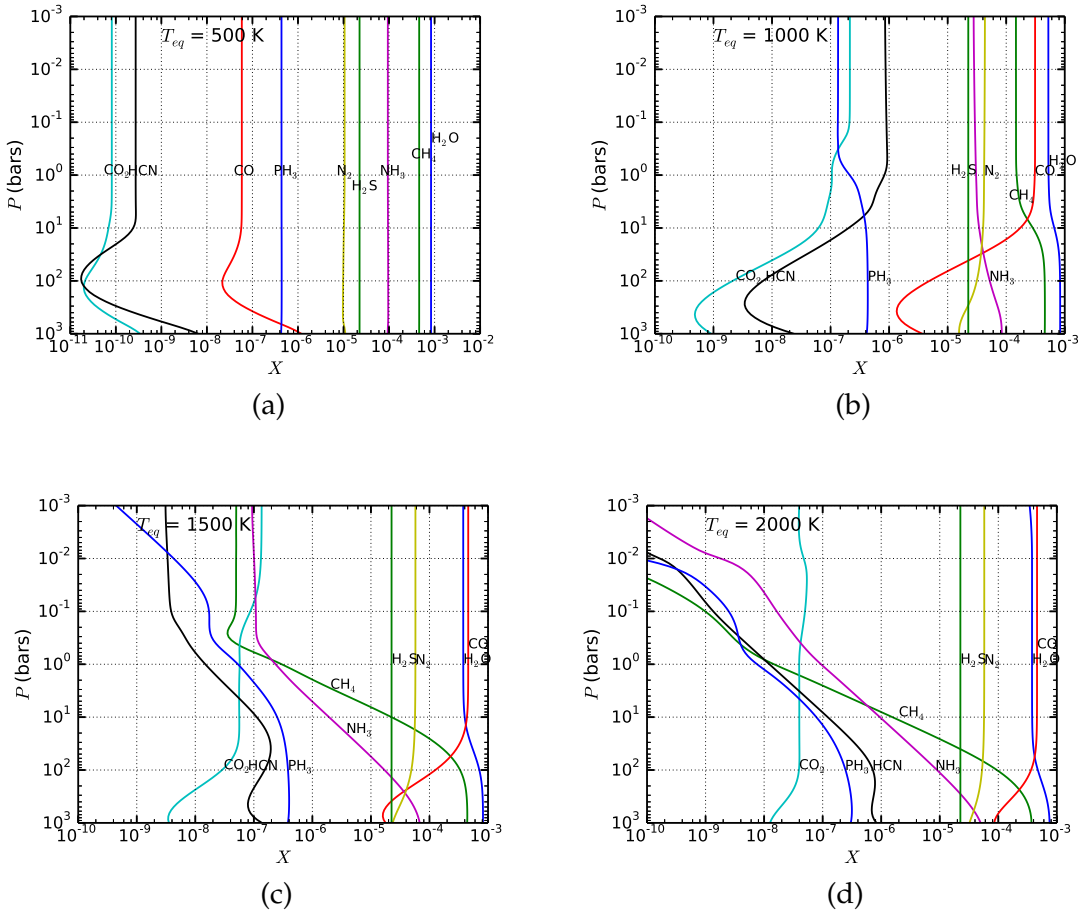

Figure 5.4 Computed mole fractions of major C/N/O/S/P bearing species in the atmosphere of extrasolar giant planets. The four plots correspond to models with different equilibrium temperatures: (a) $T_{\rm eq}$ = 500 K, (b) $T_{\rm eq}$ = 1000 K, (c) $T_{\rm eq}$ = 1500 K, (d) $T_{\rm eq}$ = 2000 K. The elemental abundances used here is one solar. The vertical eddy diffusion coefficient used here is $K_{\rm eddy} = 1 \times 10^9$ cm^2 s^{-1}.

ported in the literature [e.g., Moses et al., 2011, Venot et al., 2012, Miguel and Kaltenegger, 2014, Hu and Seager, 2014]. We find the major C/N/O/H bearing molecules are H_2O, CO, CH_4, CO_2, N_2, NH_3, and HCN. These molecules must be included in the spectra calculation in order to cover all important opacity sources. We present our computed vertical profile of these molecules along with PH_3 and H_2S in Fig. 5.4. The results are shown for four different levels of stellar insolation.

For atmospheres with $T_{\rm eq} = 500$ K, the most abundant species are H_2O, CH_4, NH_3, H_2S, N_2 and PH_3. The abundances are nearly homogeneous in the vertical direction down to ~ 10 bars. The atmosphere is strongly homogenized by vertical mixing, and species are in a disequilibrium state. CH_4 is the primary carbon-bearing species, H_2O is the primary oxygen-bearing species, NH_3 is the primary nitrogen-bearing species, H_2S is the primary sulfur-bearing species, and PH_3 is the primary phosphorus-bearing species.

For atmospheres with $T_{\rm eq} = 1000$ K, the most abundant species are H_2O, CO, CH_4, N_2, NH_3, H_2S, HCN, and PH_3. Abundances are nearly homogeneous down to 1-10 bars due to the effect of vertical mixing. CO carries about 2/3 of the total carbon abundance, and CH_4 carries the other 1/3 of the total carbon abundance. H_2O is the dominant oxygen bearing species. N_2 and NH_3 each carries about 1/2 of the total nitrogen abundance. This temperature marks the transition temperature for CO/CH_4 conversion and N_2/NH_3 conversion. For $T_{\rm eq} \lesssim 1000$ K, CH_4 and NH_3 are the major carbon and nitrogen carriers; for $T_{\rm eq} \gtrsim 1000$ K, CO and N_2 are the major carbon and nitrogen carriers.

For atmospheres with $T_{\rm eq} = 1500$ K, the most abundant species are CO, H_2O, N_2, and H_2S. CO is the primary carrier of both oxygen and carbon. The rest of

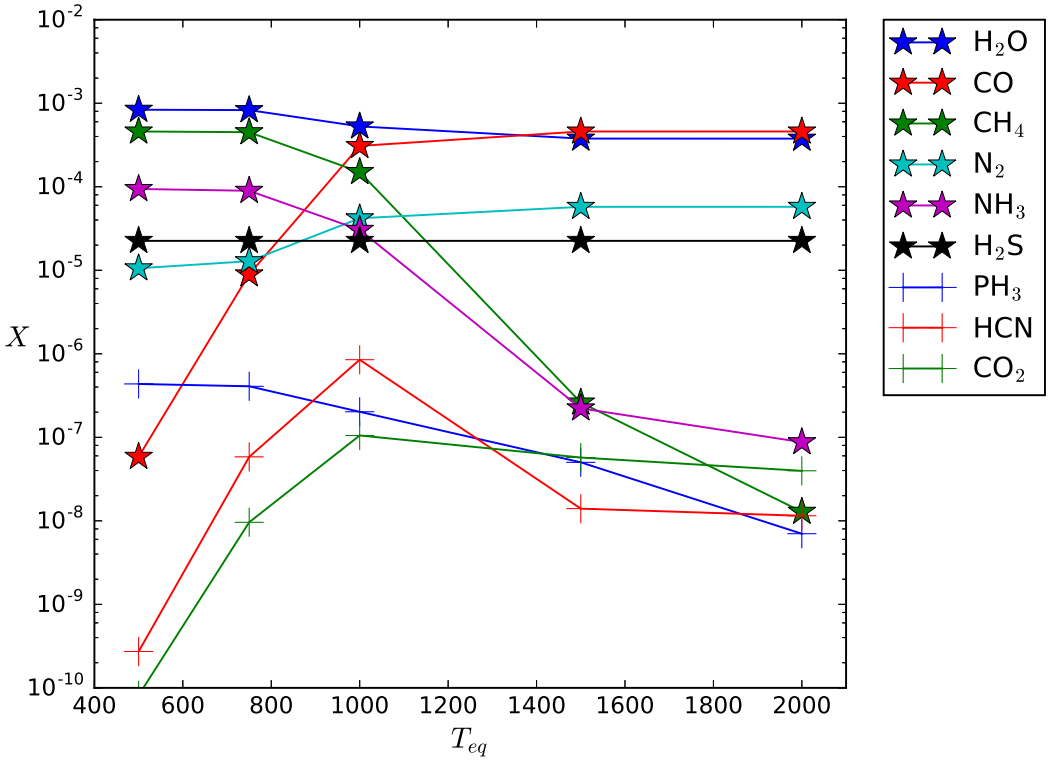

Figure 5.5 Mole fractions at 1 bar as a function of the equilibrium temperatures of atmospheres. The species plotted are H_2O, CO, CH_4, CO_2, NH_3, N_2, HCN, H_2S, and PH_3.

the oxygen is in the form of H_2O. N_2 is the primary carrier of nitrogen. CH_4 and NH_3 are much less abundant in the atmospheres.

For atmospheres with $T_{\rm eq}$ = 2000 K, the most abundant species are CO, H_2O, N_2, and H_2S. The abundances are nearly in chemical equilibrium due to the high temperature. CH_4, NH_3, and PH_3 are much less abundant.

Table 5.2 Fiducial planetary system parameters in the model

T_{eq} (K)	M_p (M_J)	R_p (R_J)	$a_{\rm semi}$ (AU)	P (days)	$T_\star$ (K)	$R_\star$ ($R_\odot$)	T_{14} (s)	D (pc)	K (mag)
500	1.0	1.0	0.310	63.1	5700	1.0	26000	50	6.8
750	1.0	1.0	0.138	18.7	5700	1.0	17333	50	6.8
1000	1.0	1.0	0.0776	7.89	5700	1.0	13000	50	6.8
1500	1.0	1.0	0.0345	2.34	5700	1.0	8666	50	6.8
2000	1.0	1.0	0.0194	0.986	5700	1.0	6500	50	6.8

5.3.4 Influence of insolation

There are three regimes for the abundance profiles depending on the level of insolation. For highly irradiated atmospheres (e.g., $T_{\rm eq} > 1500$ K), the chemical abundances are in local chemical equilibrium. Therefore, when doing atmosphere composition and T-P profile retrieval, assumptions of chemical equilibrium should be valid. For moderately irradiated atmospheres (e.g., $T_{\rm eq} < 1000$ K), the vertical mixing tends to produce a homogeneous abundances in the atmospheres. It should be valid to assume a constant mixing ratio profile when doing atmospheric retrieval. In between is the transition regime when both chemical reactions and vertical mixing are important in the atmospheres. In this regime, the abundance profiles will depend the vertical eddy diffusion coefficient as well as the T-P profile. In Fig 5.5, we show the computed abundances at 1 bar level as a function of $T_{\rm eq}$. From the figure, CO, CO_2, and N_2 abundances increase as $T_{\rm eq}$ increases, while CH_4, NH_3, and PH_3 abundances decrease as $T_{\rm eq}$ increases. H_2O and H_2S abundances remain approximately unchanged relative to the change of $T_{\rm eq}$. The HCN abundance increases and decreases as $T_{\rm eq}$ increases.

5.4 Results for noiseless spectra modeling

In this section, we present the synthetic primary and secondary transit spectra for four fiducial planetary systems. The parameters for the planetary systems are summarized in Table 5.2. The planets being modeled are extrasolar giant planets with different levels of insolation. The vertical T-P profiles for the planets are presented in Fig. 5.1 and the vertical abundance profiles are presented in Fig 5.4. The molecules included are H_2O, CO, CH_4, CO_2, N_2, NH_3, HCN, H_2S and PH_3.

The spectral features for H_2O, CO, CH_4, CO_2, and NH_3 have been explored in the literature [e.g. Greene et al., 2016]. The other species are H_2S, PH_3 and HCN. From our computations in section 5.3, we found H_2S is the primary carrier of sulfur for all different equilibrium temperatures; PH_3 is the primary carrier of phosphorus for planets with $T_{\rm eq} < 1000$ K; HCN has a mixing ratio of 1 ppm for $T_{\rm eq}$ = 1000 K. These molecules are potentially identifiable from the transit spectra. Although HCN is not the primary carrier of either carbon or nitrogen, it is a disequilibrium species and its abundances are indicative of the strength of vertical mixing. Therefore, we also investigate the spectral feature of HCN and see if JWST can potentially detect and measure the abundance of HCN.

Here we focus on identifying spectral features for PH_3, H_2S, and HCN in the primary and secondary transit spectra. We compare the spectra including all nine species with the spectra with one specific species excluded, in order to find the spectral feature of that specific species.

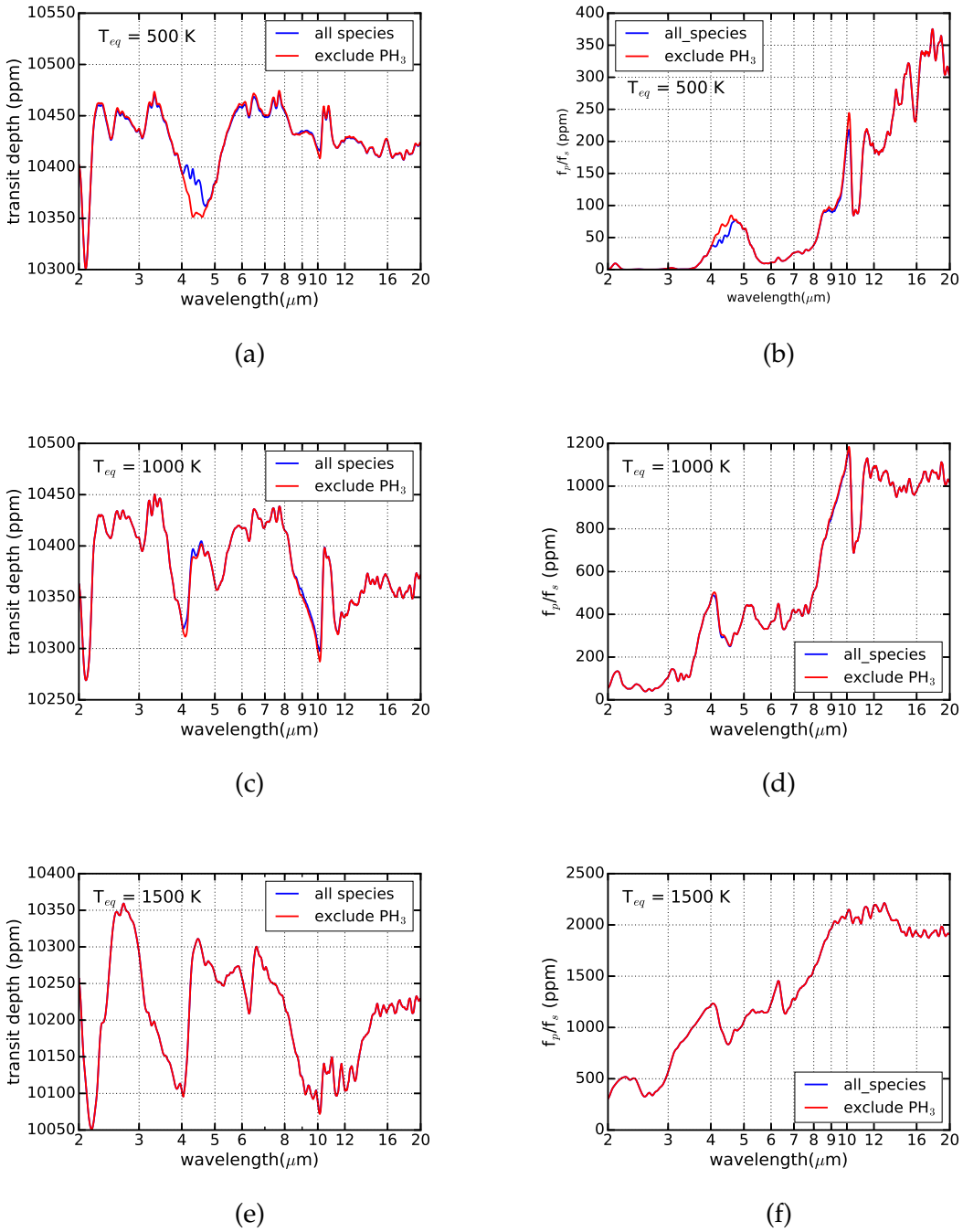

Figure 5.6 Simulated transmission and emission spectra for *all species* (including H_2O, CO, CH_4, CO_2, NH_3, N_2, HCN, H_2S, and PH_3) compared with *all species except* PH_3. The difference between the blue curve and the green curve indicates the absorption from PH_3. The spectra are smoothed to a resolution of 100.

5.4.1 PH_3

In Fig. 5.6, we present the primary and secondary transit spectra for planets with $T_{\rm eq}$ = 500 K, 1000 K, and 1500 K in Table 5.2. We compare the spectra simulated with *all species*, and the spectra simulated with *all species except* PH_3. The difference between these two spectra indicates the absorption from PH_3. For the planet with $T_{\rm eq}$ = 500 K, the absorption from PH_3 occurs between 4 and 5 μm. The absorption depth is about 40 ppm in the primary transit spectra. The absorption is about 20 ppm in the secondary transit spectra. For the planet with $T_{\rm eq} = 1000K$, the absorption is about 5 ppm in the primary transit spectra, while in the secondary transit spectra, the absorption is too small to be seen in the figure. For the plane with $T_{\rm eq} = 1500K$, there is no apparent PH_3 absorption feature in the spectra.

The lack of PH_3 spectral feature for $T_{\rm eq}$ = 1000 K and 1500 K is due to the thermal decomposition of PH_3 under high temperatures. From Fig. 5.2, for planets with $T_{\rm eq} = 500K$, almost all of the phosphorus are in the form of PH_3; while for planets with $T_{\rm eq}$ = 1000 K and 1500 K, most phosphorus are in the form of P_2 and PH_2. Therefore, the spectral features of PH_3 are only expected in moderately irradiated atmospheres.

5.4.2 H_2S

In Fig. 5.7, we present the synthetic primary and secondary transit spectra for the planets with $T_{\rm eq}$ = 750 K, 1000 K, and 1500 K in Table 5.2. We compare the spectra simulated with *all species* and the spectra simulated with *all species except* H_2S. For planets with $T_{\rm eq}$ = 750 K, the absorption depth is very small. In the primary transit spectra, there is a 5 ppm absorption at $2.6 \sim 2.8$ μm and a 10 ppm

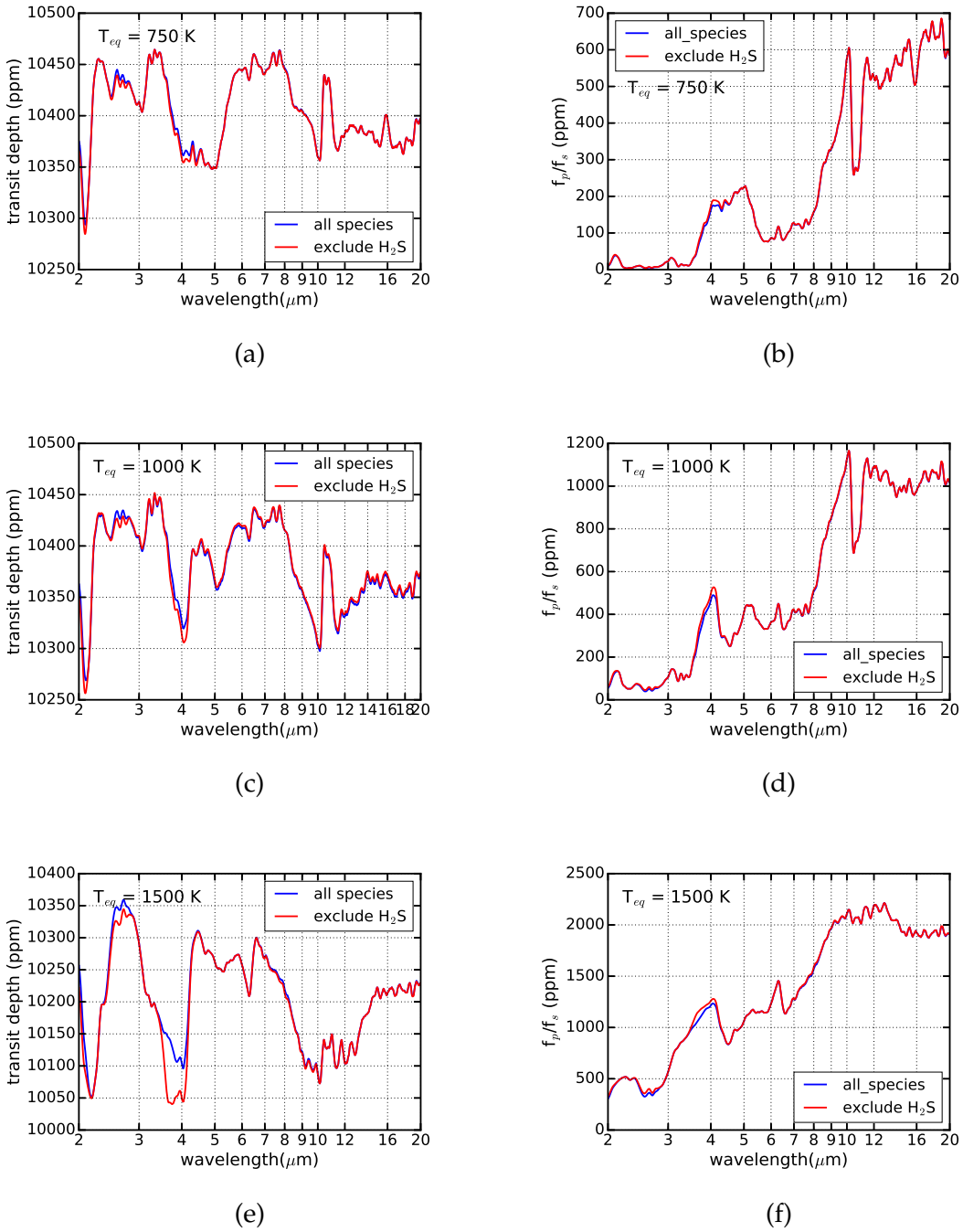

Figure 5.7 Simulated transmission and emission spectra for *all species* (including H_2O, CO, CH_4, CO_2, NH_3, N_2, HCN, H_2S, and PH_3) and *all species except* H_2S. The difference between the green curve and the blue curve indicates the absorption by H_2S. The spectra are smoothed to a resolution of 100.

absorption at 3.9 $\sim$ 4.3 μm. In the secondary transit spectra, there is a 10 ppm absorption at 3.9$\sim$ 4.3 μm. For planets with $T_{\rm eq}$ = 1000 K, the absorption depths are also very small, for both primary transit and secondary transit spectra. For planets with $T_{\rm eq}$ = 1500 K, the absorption depths are much bigger. In the primary transit spectra, the absorption depth is about 15 ppm at 2.6$\sim$2.8 μm, and 100 ppm at 3.5$\sim$4.1 μm. In the secondary spectra, the absorption depth is about 10 ppm at 2.6 $\sim$ 2.8 ppm and 100 ppm at 3.5$\sim$ 4.1 μm.

The spectral feature of H_2S is more prominent in highly irradiated atmosphere. What determines the relevance of H_2S in the spectra is other species. In cold atmospheres, H_2S has to compete with the more abundant NH_3 and CH_4 to absorb photons while in the hottest case those two molecules are less abundant, leaving more space to H_2S to absorb photons and be seen in the spectra. Another factor that may also contribute is the larger pressure scale height in hotter atmospheres.

5.4.3 HCN

In Fig. 5.8, we present the synthetic primary and secondary transit spectra for planets with $T_{\rm eq}$ = 750 K, 1000 K, and 1500 K listed in Table 5.2. For the planet with $T_{\rm eq}$ = 750 K and 1500 K, there are little absorption from HCN, mainly because the mixing ratio of HCN is very low, as shown in Fig. 5.4. For the planet with $T_{\rm eq}$ = 1000 K, there are small absorption features between 12 and 16 μm. The absorption depth in the primary transit spectra is about 15 ppm, and the absorption depth in the secondary transit spectra is about 80 ppm.

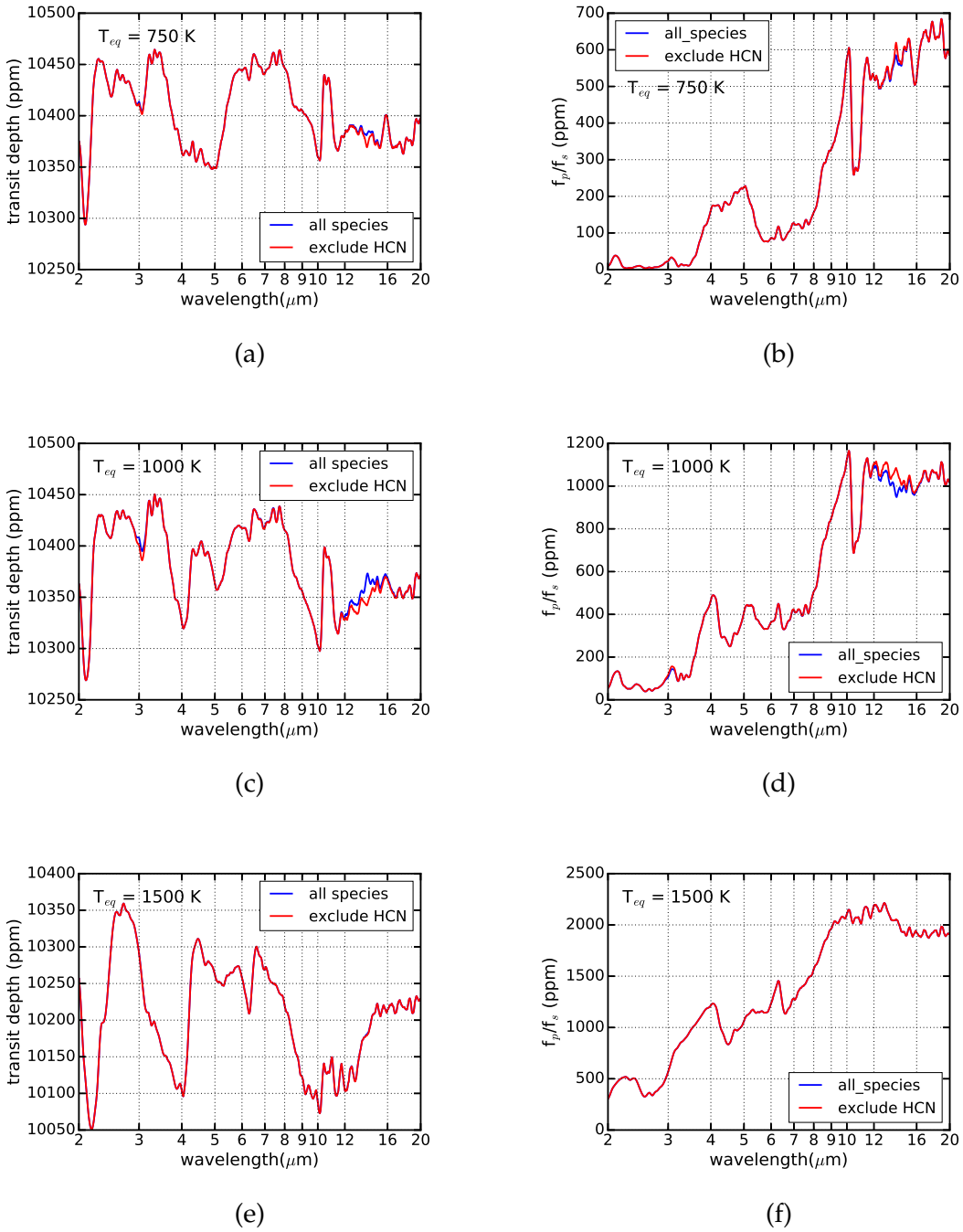

Figure 5.8 Simulated transmission and emission spectra for *all species* (H_2O, CO, CH_4, CO_2, NH_3, N_2, HCN, H_2S, and PH_3) and *all species except* HCN. The difference between the green curve and the blue curve indicates the absorption by HCN. The spectra are smoothed to a resolution of 100.

5.5 Results for JWST transit spectra modeling

In this section, we model the JWST spectra observations for primary and secondary transit. The instruments and modes for transit observations are shown in Table 5.1. The wavelength range modeled is between 2 μm and 11 μm. In section 5.4, we identified spectral features for PH_3, H_2S, and HCN. The spectral feature of PH_3 is between 4 μm and 5 μm, the spectral feature of H_2S is between 3 μm and 4 μm, and the spectral feature of HCN is between 12 μm and 16 μm. The feature of HCN is beyond the limit of MIRI LRS mode [Beichman et al., 2014]. In this paper, we focus on the detectability of H_2S and PH_3.

5.5.1 Results for JWST noise modeling

The transit depth is computed by the subtraction between the number of photons out of transit and in transit, and divided by the number of photons out of transit. The noise of the transit depth is thus approximately the inverse of the signal to noise ratio for the stellar flux. Here we compute the noise to signal ratio following the procedure described in section 5.2.3, including computing the signal shot noise, the background shot noise, the detector noise, as well as the systematic noise.

In Fig. 5.9, we show different noise components as a function of wavelength. The star being modeled is a Sun-like star at a distance of 50 pc, and the K-band magnitude is 6.8. The integration time is set at three hours. In this case, the systematic noise is the most important noise component. The signal shot noise is the most important random noise component. The background noise and the

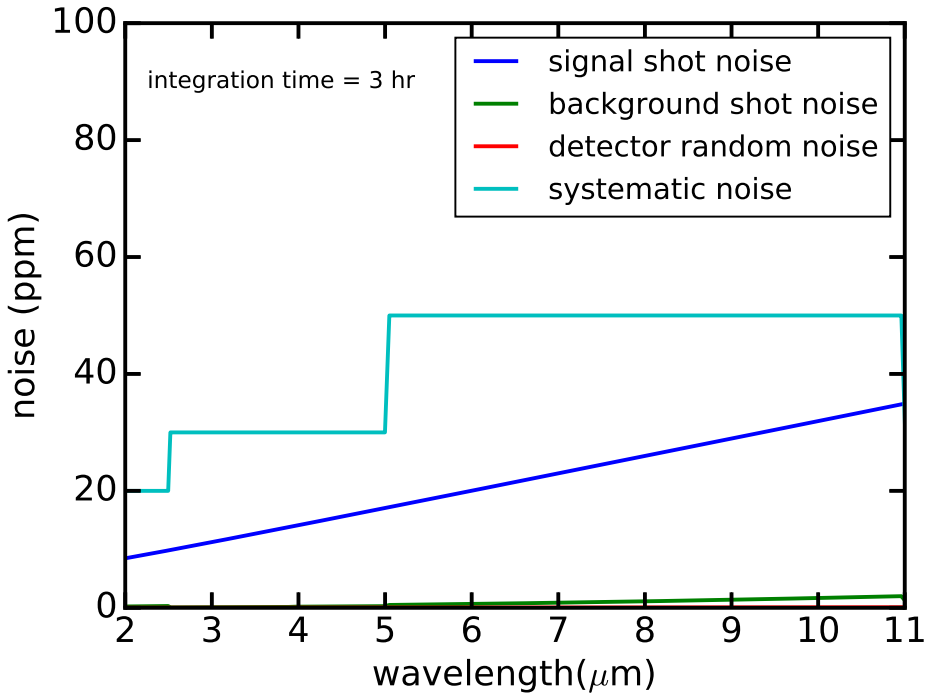

Figure 5.9 Different noise components as a function of wavelength for selected JWST instruments and modes in Table 5.1. The target of the transit observation is a Sun-like at a distance of 50 pc with K-band magnitude of 6.8. The integration time is three hours in this calculation.

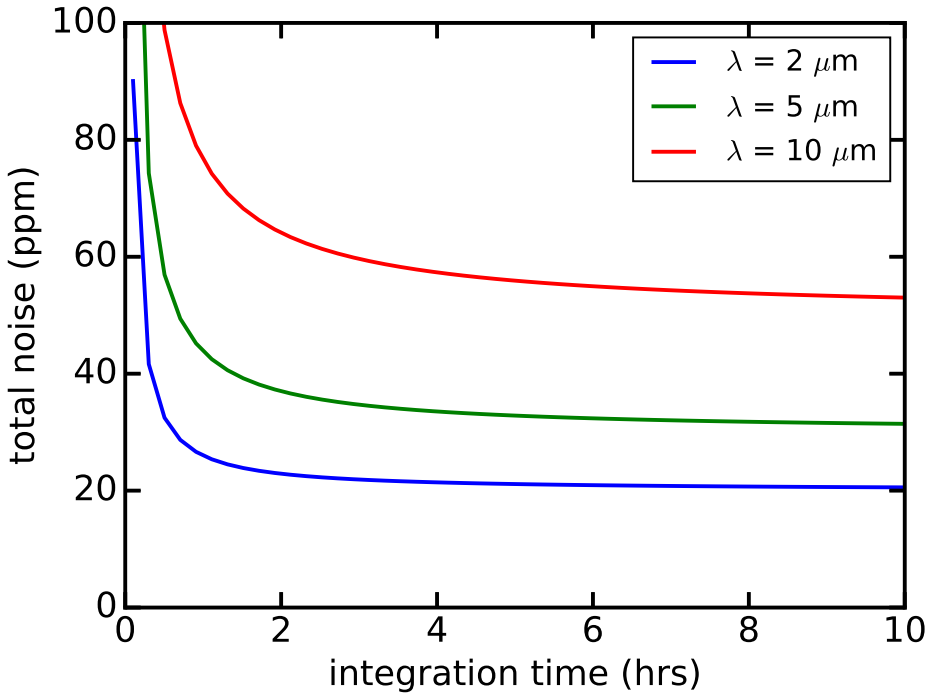

Figure 5.10 Total noise as a function of integration time for selected JWST instruments and modes in Table 5.1. The target of the transit observation is a Sun-like star at a distance of 50 pc with K-band magnitude of 6.8. The selected wavelength bins are at 2 μm, 5 μm, and 10 μm,respectively.

detector noise contributions are small. The large aperture of JWST enables the collection of large number of photons in the integration time, thus reducing the random noise to a very small level. The total noise is limited by the systematic noise level.

In Fig. 5.10, we show the total noise as a function of the integration time. The star being modeled is still a Sun-like star at a distance of 50 pc, with K-band magnitude of 6.8. The total noise includes both systematic noise and the random noise. The total noise decreases quickly when the integration time is less than one hour, due to the reduction of error by collecting more photons. For an integration time longer than one hour, the total noise converges to the systematic noise floor. Note that the random noise is approximately proportional to the distance. Therefore, for a Sun-like star at a distance of 100 pc, the required integration time to reach the systematic noise floor is about two hours.

5.5.2 PH_3

In Fig. 5.11, we show the synthetic primary and secondary transit spectra with simulated JWST noise and compare the spectra with and without PH_3. We only show the case with $T_{\rm eq}$ = 500 K. For higher equilibrium temperatures (1000 K and 1500 K), the spectral feature of PH_3 is below 5 ppm that JWST is unlikely to detect it. The spectral absorption feature is between 4.0 and 4.7 μm. In the primary transit spectra, the absorption depth from PH_3 is approximately one standard deviation of the noise. Since there are ~ 10 measurements within this feature, the shape of the spectral feature can be resolved. A single transit observation using the NIRCam LW grism mode with F444W filter is sufficient to

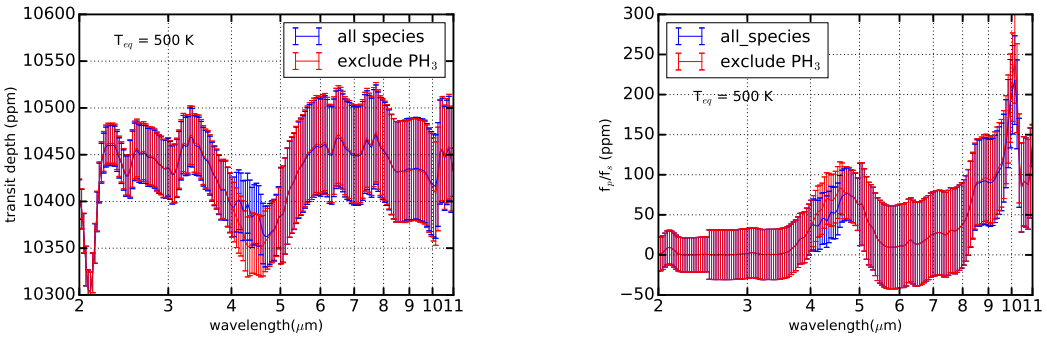

(a) (b)

Figure 5.11 Synthetic transmission and emission spectra with simulated JWST noise for the planets presented in Table 5.2 with $T_{\rm eq}$ = 500 K. The blue curve is the spectra simulated including all nine species in Fig. 5.4, and the red curve is simulated including all nine species except PH_3. The simulated JWST instruments and modes are summarized in Table 5.1.

cover the spectral feature. The absorption feature in the secondary transit spectra is harder to detect since the absorption depth from PH_3 is only about half the standard deviation of the noise. Therefore, it is the most effective for detecting PH_3 to use the primary transit spectra with the NIRCam LW grism mode and F444W filter, and get the spectra between 3.9 μm and 5.0 μm.

5.5.3 H_2S

In Fig. 5.12, we show the synthetic primary and secondary transit spectra with simulated JWST noise and compare the spectra with and without H_2S. We only show the case for $T_{\rm eq}$ = 1500 K. For lower equilibrium temperatures (500 K, 750 K, 1000 K), the absorption from H_2S is below 10 ppm and JWST is unlikely to detect it. The spectral absorption feature of H_2S is between 3.5 and 4 μm. In the primary transit spectra, the absorption depth is about two times the standard deviation of the noise. The shape of the absorption feature can be resolved with

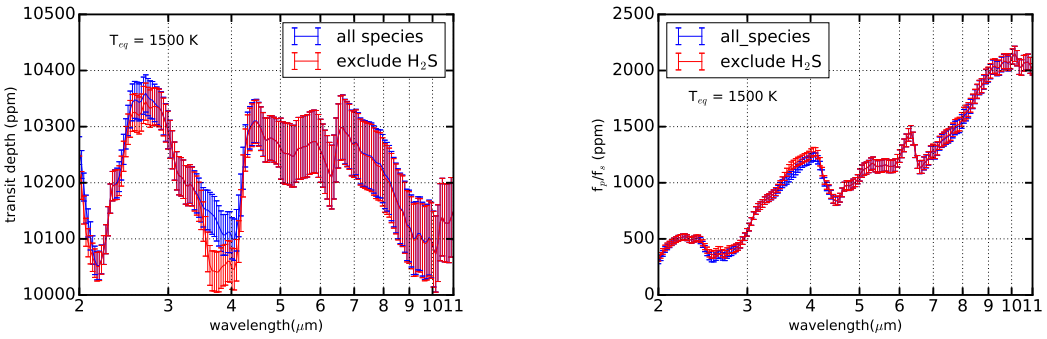

(a) (b)

Figure 5.12 Synthetic transmission and emission spectra with simulated JWST noise for planets presented in Table 5.2 with $T_{\rm eq}$ = 1500 K. The blue curve is the spectra simulated including all nine species in Fig. 5.4, and the red curve is simulated including all nine species except H_2S. The simulated JWST instruments are summarized in Table 5.1.

the binned spectral resolution of R $\sim$ 100. To cover the spectral feature of H_2S, one can use the NIRCam LW grism mode with F322W2 filter, getting the spectra between 2.4 μm and 4.0 μm. In the secondary transit spectra, the absorption depth is approximately two times the standard deviation of the noise. Therefore, it is also likely to detect H_2S in the secondary transit spectra. The same mode of NIRCam can be used to obtain the secondary transit spectra.

5.6 Discussion

In this paper, we investigate the disequilibrium phosphorus chemistry in hydrogen-rich atmospheres of exoplanets. We find PH_3 is the primary carrier of phosphorus for planets with $T_{\rm eq} \sim$ 500 K. For planets with 1000 K $\lesssim T_{\rm eq} \lesssim$ 1500 K, the primary carrier is P_2. For very higher temperatures ($T_{\rm eq} \sim$ 2000 K), phosphorus is mainly sequestered in PH_2 and PH. We also investigate the chemistry

of C/N/O/S bearing species. The most abundant carbon and nitrogen bearing species depend on the level of insolation. H_2S is the primary carrier of sulfur for planets with $T_{\rm eq} < 2000$ K. With the computed abundance profiles for H_2O, CO, CO_2, CH_4, NH_3, N_2, H_2S, PH_3, and HCN, we model the synthetic primary and secondary transit spectra and identify spectral features for PH_3, H_2S, and HCN. The detectibility of PH_3 and H_2S with JWST transit observations are evaluated by simulating the noise levels. We find PH_3 can be detected in the primary transit spectra for moderately irradiated extrasolar giant planets with $T_{\rm eq} \lesssim 500$ K using JWST NIRCam LW grism mode and F444W filter. H_2S can be detected in both primary and secondary spectra of extrasolar giant planets with $T_{\rm eq} \gtrsim 1500$ K using JWST NIRCam LW grism mode and F322W2 filter.

Our results imply that JWST has the potential to detect H_2S in exoplanet atmospheres with $T_{\rm eq} > 1500$ K in a single transit, and constrain the elemental abundances of sulfur. The advantage of extrasolar giant planets compared with solar system giant planets is that H_2S does not condense in many hot exoplanetary atmospheres. The abundance of H_2S probed by the secondary transit spectra should represent the bulk abundance of sulfur. Our results also imply that it is possible to detect PH_3 in the atmospheres of extrasolar giant planets with $T_{\rm eq} < 500$ K, but the determination of abundances may be difficult since the absorption depth from PH_3 is close to the expected noise level. JWST's large aperture and photon collection abilities enable the reduction of random noise to ~ 20 ppm level in a single transit observation of three hours (see Fig. 5.9 and Fig. 5.10). However, the total noise is limited by the systematic noise component. Further reduction of systematic noise would be necessary for determining the abundances of PH_3 in extrasolar giant planets.

The transit spectra of PH_3 and H_2S are complicated by the presence of clouds or hazes in the atmospheres of extrasolar giant planets. Current observations indicate that clouds or hazes are ubiquitous in the atmospheres of exoplanets [e.g. Pont et al., 2008, Deming et al., 2013, Kreidberg et al., 2014a]. Clouds and hazes reduce the amplitude of transmission spectra and thus decrease the molecular spectral features with a negative effect on the determination of molecular abundances. The emission spectra are less affected by the clouds and hazes [e.g., Line et al., 2016]. The spectral absorption depth of H_2S in the emission spectra is much greater than the expected noise level. Therefore, the H_2S feature can be detected using the emission spectra for atmospheres with clouds and haze. However, the absorption depth of PH_3 in the emission spectra is smaller than the expected noise level, therefore, the detection of PH_3 will be difficult if the atmosphere is covered by clouds or hazes.

Our results also highlight the importance of including H_2S when doing abundances retrieval from future JWST transit observations. For planets with $T_{\rm eq} \gtrsim 1500$ K, the absorption from H_2S is non-negligible in both transmission and emission spectra. PH_3 is not spectroscopically important except for planets with $T_{\rm eq} \lesssim 500$ K.

We also considered HCN in our model since we find HCN is non-negligible for planets with $T_{\rm eq}$ = 1000 K, with a mixing ratio of 1 ppm. Since photochemistry also produces HCN, we expect more HCN in the upper atmospheres. The absorption features of HCN are mainly between 12 and 16 μm. This wavelength range is beyond the coverage of the MIRI LRS siltless mode. Therefore, we did not discuss further the detectability of HCN with JWST.

Our paper is subject to improvements in the following aspects.

- In this paper, we restrict our study to solar composition atmospheres. However, the elemental composition of exoplanetary atmospheres can be diverse. Jupiter's atmosphere is enriched in heavy elements relative to solar. It is reasonable to assume extrasolar giant planets have similar enrichment. If all the heavy elements (C,N,O,S,P) are enriched similarly, the shape of the abundance profiles is preserved with only an upward shift. We expect the transmission spectra to have smaller spectral amplitudes since the pressure scale height is expected to be smaller for higher molecular mass atmospheres. This has an adverse effect on detecting molecules. However, higher mean molecular weight often correlates with smaller mass. For Neptune-size planets, the smaller gravity means higher scale height, and larger spectral amplitudes. The opposite effect of gravity and molecular mass on the spectra should rely on detailed modeling of Neptune -size exoplanets, which will be discussed in our next paper. If carbon and oxygen are not similarly enriched, for example C/O different than solar, the composition will be dramatically different for hot atmospheres.

- In this paper, we neglect the effect of photochemistry on the primary and secondary transit spectra. Photochemistry affects the spectra in two ways. First, photochemistry changes the abundance profiles in the upper atmospheres. The effect on the secondary transit spectra is expected to be small since the absorption in the planetary emission spectra occurs near the 1 bar level. There may be some effects on the primary transit spectra since the light travels a longer path in the transmission spectra than in the emission spectra. Most absorption should still be from more abundant molecules (e.g. H_2O, CH_4, CO, NH_3, H_2S, PH_3) in the atmospheres. The photochemical products (C_2H_6, C_2H_2, HCN) may contribute a small amount

of absorption and it is unclear whether JWST is able to detect these photochemical species. The second effect of photochemistry is the production of hazes. The flat transmission spectra for hot Jupiters and super-Earth may be caused by the photochemical hazes in the upper atmospheres. The effect of hazes on the spectra is the shrinking of the spectral amplitude, making the detection of molecules more difficult.

5.7 Conclusions

We modeled phosphorus chemistry in the atmospheres of Jupiter-mass planets assuming solar composition. We find PH_3 is the primary carrier of phosphorus for atmospheres with $T_{\rm eq} < 1000$ K; P_2 is the primary carrier of phosphorus for $T_{\rm eq}$ greater than 1000 K and smaller than 1500 K; PH and PH_2 are the primary phosphorus bearing species for $T_{\rm eq} > 2000$ K. We also compute the abundance profiles of major H/C/N/O/S bearing species. With the computed vertical profiles for H_2O, CO, CO_2, CH_4, NH_3, N_2, HCN, H_2S, PH_3, we compute the synthetic transit spectra for planets with different levels of insolation. We focus on identifying the spectral features for H_2S, PH_3, and HCN. We find spectral features of PH_3 at 4.0 $\sim$ 4.8 μm, H_2S at 2.5 $\sim$ 2.8 μm and 3.5 $\sim$ 4.1 μm, HCN at 12 $\sim$ 16 μm. We then simulate the noise of JWST transit observations and compute the errorbar of the synthetic spectra. We find PH_3 can be detected for planets with $T_{\rm eq} < 500$ K in a single transit, using the NIRCam instrument with LW grism mode and F444W filter. We find H_2S can be detected for planets with $T_{\rm eq} > 1500$ K in a single transit, using the NIRCam instrument with LW grism mode and F322W2 filter. For our simulated Sun-like star located at 50 pc, the noise is limited by the systematic noise level instead of the random noise. The

spectral amplitude can be diminished by the clouds and hazes. In this case, H_2S may still be detected in the emission spectra, but PH_3 is difficult to detect since its absorption feature is smaller than the estimated JWST noise in the emission spectra.

CHAPTER 6

CONCLUSIONS AND REMAINING QUESTIONS

In this dissertation, we modeled the disequilibrium chemistry of giant planetary atmospheres, including Jupiter, Saturn, and Jupiter-size extrasolar giant planets. Our primary contributions are as follows.

- We improved the chemical constraints on the deep water abundance of Jupiter. CO abundance as observed in the troposphere of Jupiter depends on the efficiency of vertical mixing as well as the deep water abundance at a few hundred bars level, for a given chemical model. In principle, the deep water abundance is dependent on the CO abundance, the eddy diffusion coefficient, and the chemical model. In Chapter 3, we revisited the eddy diffusion coefficient and the chemical models. We proposed a new formulation for the vertical eddy diffusion coefficient ($K_{\rm eddy}$) in the convective envelope of Jupiter based on the experimental results of turbulent rotating convection. The new formulation indicates two regimes, one is in the non-rotating limit near the equatorial region, and a rotating limit at higher latitudes. With experimentally determined coefficients, our new formulation has a much smaller uncertainty compared with that in the literature. We also considered two different chemical models, one is compiled specifically for modeling planetary atmospheres but not validated against any experiments, while the other model was originally for combustion studies, but validated against various experiments. We recomputed the constraints on the deep water abundance by the measured CO abundance with the two different chemical models. One model predicts the enrichment of water is between 0.1 and 0.75, the other model pre-

dicts the enrichment of water between 3 and 11. The dramatic difference is due to the uncertainties on the kinetic data of C/H/O bearing chemical species.

- We developed an approach for break the degeneracy between the eddy diffusion coefficient and the deep water abundance. Although we have proposed a formulation for the eddy diffusion coefficient in Chapter 3, the formulation is based on extrapolation of experimental parameter space to the Jupiter's parameter space. Direct constraints on the deep eddy diffusion coefficient is not available. Through our detailed modeling on the atmospheric chemistry of Saturn, we found C_2H_6 as another disequilibrium species present in the troposphere of Saturn with a mixing ratio of 1 ppb. The abundance of C_2H_6 is only a function of the eddy diffusion coefficient, with no dependence on the water abundance. This provided a way to break the degeneracy between the water abundance and the eddy diffusion coefficient. A shallow Saturn entry probe has the potential to measure the abundance of CO and C_2H_6 at a few bars level, thus potentially has the capability to constrain the deep water abundance for Saturn. Similarly, if C_2H_6 can be measured on Jupiter, the constraints on water will bear less uncertain. However, the Juno spacecraft does not have the capability to measure deep C_2H_6 for Jupiter, and it remains to be investigated whether ground based observations will be able to measure the deep C_2H_6 for Jupiter.

- The latitudinal variation of the eddy diffusion coefficient implies the latitudinal variation of disequilibrium species. We compute the abundances of CO, PH_3, GeH_4, AsH_3 as a function of latitude for Jupiter. We find the abundances of CO and GeH_4 decrease towards higher latitudes, but the

abundances of PH_3 and AsH_3 remain constant across latitudes. Giles et al. [2017] measured the latitudinal profile of disequilibrium species GeH_4, AsH_3, and PH_3, and confirmed the variability. However, they found enhancements of PH_3 and AsH_3 abundances towards higher latitudes, and approximately constant GeH_4 abundances. Such difference from our predictions merit further investigations.

- For extrasolar giant planets, observations using the Hubble space telescope have detected molecules in their atmospheres, including several reported observations of water vapor. With the upcoming JWST observations, more molecules can be uncovered from the atmospheres of extrasolar giant planets. We focused on investigating the chemistry of sulfur and phosphorus in the atmospheres of extrasolar giant planets. By modeling the spectra of extrasolar giant planets with JWST, we evaluated the detectability of H_2S and PH_3 in the atmospheres of extrasolar giant planets. Using the abundance profiles computed for major C/N/O/S/P bearing species, we model the JWST primary and secondary transit spectra for systems with a Sun-like star at a distance of 50 pc and with different levels of insolation. We find PH_3 is detectable in the transmission spectra for planets with $T_{\rm eq} < 500$ K using the NIRCam instrument with LW grism mode and F444W filter, and the H_2S is detectible in the transmission and emission spectra for planets with $T_{\rm eq} >$1500 K using the NIRCam instrument with LW grism and F322W2 filter. Our results specially highlight the importance of including H2S for future abundances retrieval with JWST.

There are several remaining questions that merit further investigation.

- In this dissertation, we selected two updated kinetic networks for

C/N/O/H chemistry. However, these two kinetic networks differs in reaction rates for several key reactions, which leads to overall large uncertainties on the deep water abundance as constrained by the CO abundance. The reaction network proposed by Moses et al. [2011] is compiled by adding reactions that are potentially relevant to Jupiter's atmospheres, but the overall reaction network is not validated against any experiments. While the reaction network proposed by Venot et al. [2012] has been validated against various combustion experiments, the conditions of these experiments are oxygen-rich instead of hydrogen-rich. Reactions that are important in hydrogen-rich environment may not be important in oxygen-rich environment, and vice versa. Therefore, it is necessary to test the existing reaction networks against kinetic experiments in hydrogen-rich environment, and preferentially also under high pressure environment (a few hundred bars). Such experiments will be crucial for tightening the constraints on the deep water abundance for all giant planets.

- In this dissertation, we proposed a latitudinal variation of disequilibrium species in the troposphere of Jupiter. Such variation was later observed by Giles et al. [2017], however, the observed variations of AsH_3, GeH_4, and PH_3 are different from our prediction in Chapter 4. There are still no good models for the observed variations. The NH_3 distributions measured by the Juno microwave radiometer indicates higher eddy diffusion coefficient near the equator, which is consistent with our prediction in Chapter 3.

APPENDIX A

CHEMICAL PATHWAY FOR CO/CH_4 CONVERSION

Table A.1 Non-equilibrium parameter f_{noneq} for reactions on the CO/CH_4 chemical pathway.

reactions	f_{noneq}, for network A, t = 4×10^4 s	f_{noneq}, for network B, t = 4×10^6
$CO \rightarrow HCO$	5.1×10^{-4}	1.8×10^{-6}
$HCO \rightarrow H_2CO$	9.1×10^{-1}	3.2×10^{-3}
$H_2CO \rightarrow CH_3O$	4.3×10^{-1}	1.3×10^{-4}
$H_2CO \rightarrow CH_2OH$	2.5×10^{-1}	7.8×10^{-5}
$CH_3O \rightarrow CH_3OH$	7.6×10^{-1}	1.3×10^{-4}
$CH_2OH \rightarrow CH_3OH$	8.2×10^{-1}	1.9×10^{-4}
$CH_3OH \rightarrow CH_3$	2.1×10^{-1}	9.5×10^{-1}
$CH_3 \rightarrow CH_4$	4.1×10^{-8}	2.5×10^{-11}

In this appendix, we introduce our method of identifying the main chemical pathway for CO/CH_4 conversion. The main chemical pathway for CO/CH_4 conversion is automatically identified from the C/N/O/H reaction network by examining the conversion rate between different carbon bearing species using *Cantera*. As an example, consider the conversion between CH_3O and CH_3OH, a non-exhaustive list of relevant reactions are

$$CH_3O + HCO \leftrightarrow CH_3OH + CO, \tag{A.1a}$$

$$CH_3O + H_2CO \leftrightarrow CH_3OH + HCO, \tag{A.1b}$$

$$CH_3O + CH_3O \leftrightarrow CH_3OH + H_2CO, \tag{A.1c}$$

$$CH_3O + CH_2OH \leftrightarrow CH_3OH + H_2CO, \tag{A.1d}$$

$$CH_3O + H_2 \leftrightarrow CH_3OH + H, \tag{A.1e}$$

..... (A.1f)

The total conversion rate from CH_3O to CH_3OH, the inverse conversion rate, and the net conversion rate are computed by summing all the rates of each in-

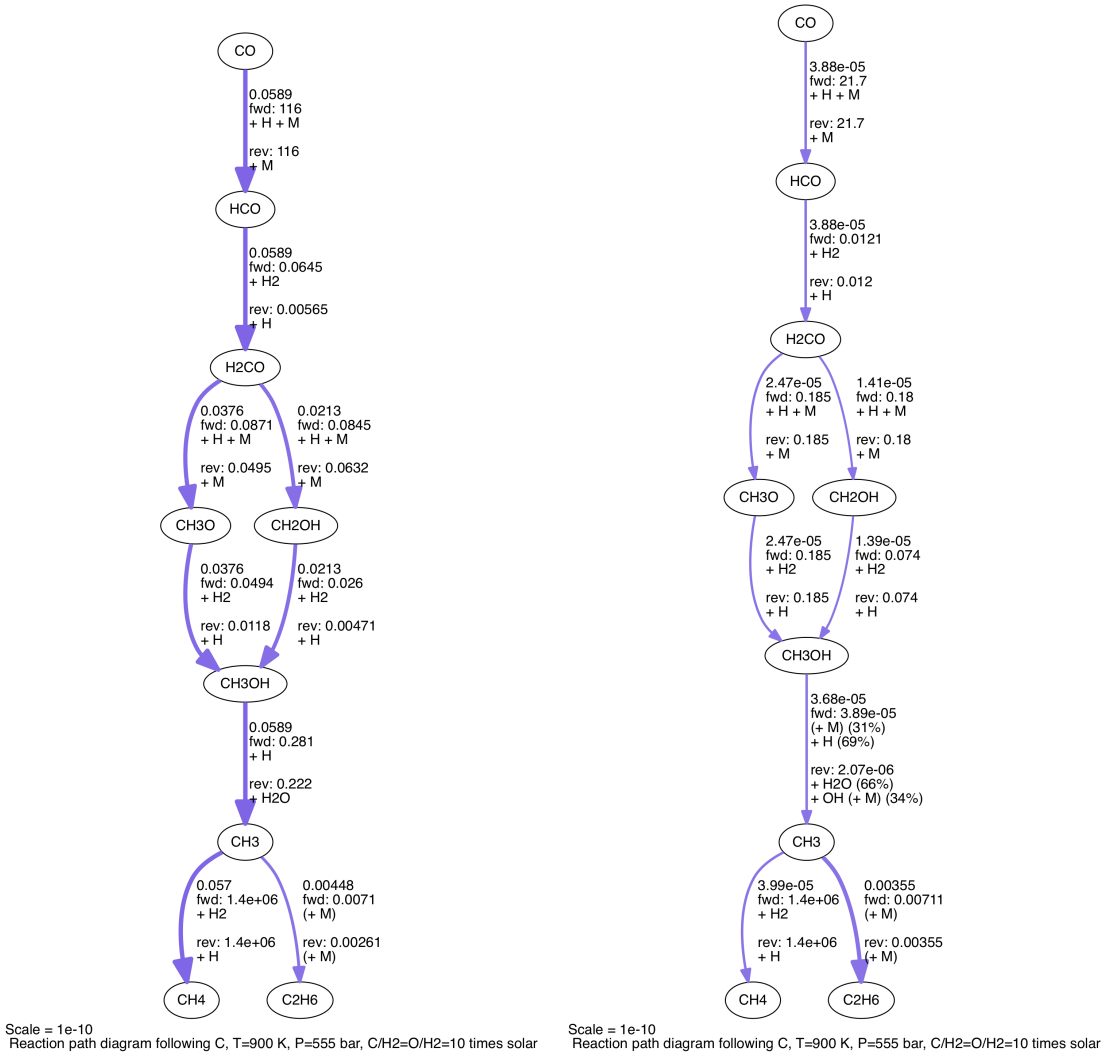

Figure A.1 Reaction path diagram for carbon bearing species generated by *Cantera*. The left figure is generated using the C/N/O/H reaction network A, and the right figure is generated using the network B. The composition and temperature-pressure condition resemble the CO quench level of Saturn ($\sim$ 900 K, 550 bars). The arrows show the flow directions of element carbon, and the labels show the net flux (in the unit of mole cm^{-3} s^{-1}) of element carbon as well as the forward flux and backward flux. The reactions responsible for the forward and backward flux are also labeled. All the carbon bearing species are considered, but only fluxes above a threshold are shown in the diagram.

dividual reactions. All pairs of carbon bearing species are considered in the computation by *Cantera*. Then the conversion rates are displayed with a diagram generated using a method called *ReactionPathDiagram* in *Cantera*. The conversions with rates higher than a threshold are summarized in the diagram. Specifically, we start our simulation from a mixture of Saturn composition gas under the condition of Saturn's CO quench level ($\sim$ 900 K, 500 bars), with CO abundance slightly higher than the equilibrium abundance. The system automatically evolves to the chemical equilibrium state, and some fraction of CO is converted to CH_4. This conversion process can be viewed as a flow of carbon element from CO to CH_4 (and other species) across the reaction network. The flow channel with the fastest rate is the main chemical pathway connecting CO and CH_4. In Fig. A.1, we show two reaction path diagrams, one using the network A and the other using the network B. The net flux of element carbon from one species to another species are labeled in the diagrams. By following the path with the highest net flux from CO to CH_4, we find the main chemical pathway for CO/CH_4 conversion as

$$CO + H + M \leftrightarrow HCO + M, \tag{A.2a}$$

$$HCO + H_2 \leftrightarrow H_2CO + H, \tag{A.2b}$$

$$H_2CO + H + M \leftrightarrow CH_3O + M, \tag{A.2c}$$

$$CH_3O + H_2 \leftrightarrow CH_3OH + H, \tag{A.2d}$$

$$H_2CO + H + M \leftrightarrow CH_2OH + M, \tag{A.2e}$$

$$CH_2OH + H_2 \leftrightarrow CH_3OH + H, \tag{A.2f}$$

$$CH_3OH + H \leftrightarrow CH_3 + H_2O, \tag{A.2g}$$

$$CH_3OH + M \leftrightarrow CH_3 + OH + M, \tag{A.2h}$$

$$CH_3 + H_2 \leftrightarrow CH_4 + H, \tag{A.2i}$$

$$CO + 3H_2 \leftrightarrow CH_4 + H_2O. \tag{A.2, net}$$

The conversion from H_2CO to CH_3OH follows two branches. The two networks agree with each other on the main chemical pathway.

Among the chemical pathway, some steps are slower than other steps, which serves as the bottleneck of the pathway. The slowest steps among the main pathway are usually called the rate determining steps. Fast steps can reach chemical equilibrium very quickly, but the slow steps are far from equilibrium. The degree of non-equilibrium can be defined in the following way. For reactions from species A to species B, we define the forward rate as r_f and the backward rate as r_b. The non-equilibrium parameter can be defined as

$$f_{\text{noneq}} = (r_f - r_b)/r_f, \tag{A.3}$$

f_{noneq} is close to zero for nearly equilibrium and between zero and one for non equilibrium. In table A.1, we show the computed value of f_{noneq} for all the steps on the pathway. For the simulations using the network A, there are several steps that are far from equilibrium. Only the first step and the last step are close to equilibrium. This indicates that the steps HCO $\rightarrow$ H_2CO and H_2CO $\rightarrow$ CH_3OH have similar rate and both bottleneck the overall chemical pathway. Using a quench-level model, we find using a single rate determining step will introduce an error about 30$\sim$50$\%$ in the prediction. For the simulations using the network B, the step from CH_3OH to CH_3 is the only step far from equilibrium, therefore, it is the rate determining step. Since the network B is similar to the network in Moses et al. [2011], our findings of the rate determining step is therefore the same as the one identified by Moses et al. [2011] and Visscher and Moses [2011]. The different choice of rate determining step is easy to understand. Since the network A adopted a larger reaction constant for the reaction H + CH_3OH $\leftrightarrow$ CH_3 + H_2O, the conversion from CH_3OH to CH_3 is no not a bottleneck, and the overall rate increases.

APPENDIX B

CHEMICAL PATHWAY FOR PH_3/H_3PO_4 CONVERSION

Table B.1 Non-equilibrium parameter $f_{\rm noneq}$ for reactions on the PH_3/H_3PO_4 chemical pathway.

reactions	$f_{\rm noneq}$, t = 1×10^8 s
$PH_3 \rightarrow PH_2$	4.7×10^{-8}
$PH_2 \rightarrow H_2POH$	1.5×10^{-2}
$H_2POH \rightarrow HPOH$	1.1×10^{-5}
$HPOH \rightarrow HPO$	3.6×10^{-5}
$HPO \rightarrow PO$	8.3×10^{-2}
$PO \rightarrow HOPO$	2.7×10^{-4}
$HOPO \rightarrow PO_2$	1.1×10^{-7}
$PO_2 \rightarrow HOPO_2$	9.3×10^{-1}
$HOPO_2 \rightarrow H_3PO_4$	1.1×10^{-8}

The chemical pathway for PH_3 destruction is automatically identified by examining the conversion rate between all species in the reaction network. The method is detailed in the Appendix A using the CO/CH_4 conversion as an example. We start our simulation from a mixture with the Saturn-like composition: He/H = 0.27, O/H = 20 times solar, and P/H = 8 times solar. The temperature and pressure are held constant as the mixture chemically evolves to an equilibrium state. In Fig. B.1, we show the reaction path diagram for phosphorus bearing species generated using *Cantera*. PH_3 is converted to H_3PO_4 bypassing a list of species: PH_2, H_2POH, HPOH, HPO, PO, HOPO, PO_2, and $HOPO_2$. In table B.1, we present the computed values of $f_{\rm noneq}$ at one instant during the chemical evolution. The only step that is far from equilibrium is the step $PO_2 \rightarrow HOPO_2$. Therefore, the rate determining reaction for PH_3/H_3PO_4 conversion near the PH_3 quench level of Saturn is $PO_2 + H_2O \leftrightarrow HOPO_2 + H$. The rate determining step could be different if the temperature and pressure conditions were very different from 800 K and 370 bars.

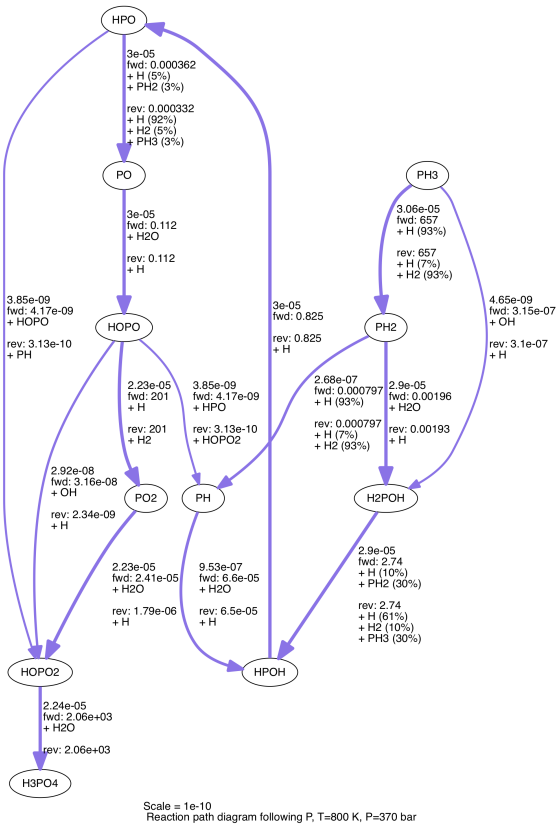

Figure B.1 Reaction path diagram for phosphorus bearing species generated by *Cantera*. The input reaction network here is the H/P/O network described in Chapter 2. The arrows in the diagram show the flow directions of element phosphorus. The labels show the net element flux (in the unit of mole cm^{-3} s^{-1}) as well as the forward flux and the backward flux. The reactions responsible for the forward and backward flux are also labeled. All species in the network are considered, but only species that have net flux above a threshold are shown in this figure.

APPENDIX C

CHEMICAL PATHWAY FOR SIH_4 DESTRUCTION

Table C.1 Non-equilibrium parameter $f_{\rm noneq}$ for reactions on the SiH_4 destruction chemical pathway.

reactions	$f_{\rm noneq}$, t = 2×10^5 s
$SiH_4 \rightarrow SiH_2$	2.3×10^{-4}
$SiH_2 \rightarrow H_2SiOH$	1.0
$HSiOH \rightarrow SiO$	9.0×10^{-4}
$SiO \rightarrow Si(OH)_2$	3.3×10^{-10}
$Si(OH)_2 \rightarrow HOSiO$	1.0
$Si(OH)_2 \rightarrow HSiO(OH)$	2.9×10^{-5}
$HSiO(OH) \rightarrow HOSiO$	1.0
$HOSiO \rightarrow SiO_2(c)$	1.8×10^{-3}

Silane (SiH_4) is oxidized into various species in the atmosphere of Jupiter and Saturn. The major products are $MgSiO_3$ condensates. The main chemical pathway is identified following the approach detailed in the Appendix A using CO/CH_4 conversion as an example. We start our simulation from a mixture with a Saturn like composition: He/H = 0.27, O/H = 10 times solar, and Si/H = 10 times solar. The temperature and pressure are held constant as the mixture evolves into chemical equilibrium state. The reaction path diagram is shown in Fig. C.1. The main destruction pathway of SiH_4 is identified from the diagram: $SiH_4 \rightarrow SiH_2 \rightarrow HSiOH \rightarrow SiO \rightarrow Si(OH)_2 \rightarrow (HOSiOOH) \rightarrow HOSiO \rightarrow SiO_2$. SiO_2 will react with $Mg(OH)_2$ to form $MgSiO_3$ under the conditions of Jupiter and Saturn. In table C.1, we present the computed values of $f_{\rm noneq}$ at an instant of the chemical evolution. There are three steps that are far from equilibrium. The first step is the conversion from SiH_2 to HSiOH, and the other two are both at the step from $Si(OH)_2$ to HOSiO. There is no unique rate-determining step for SiH_4 destruction.

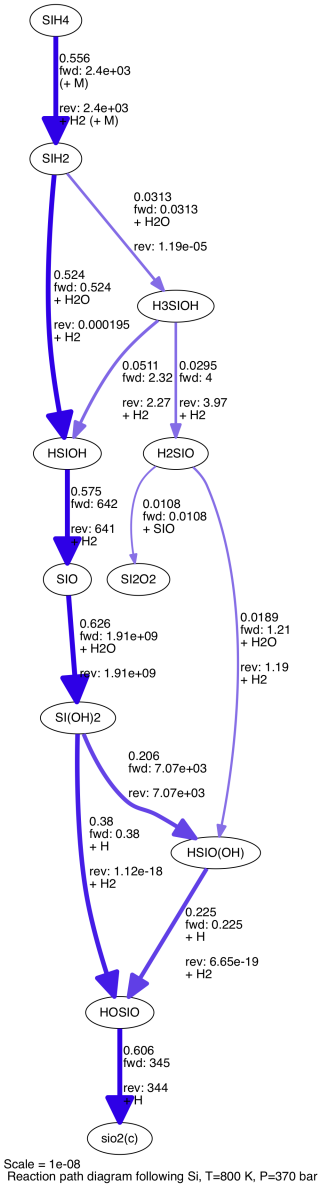

Figure C.1 Chemical pathway for silicon bearing species generated by *Cantera*. The input reaction network here is the H/Si/O network described in chapter 2. The arrows show the flow directions of element silicon. The labels show the net flux (mole cm^{-3} s^{-1}) of element silicon as well the forward flux and the backward flux. Also labeled are the reactions responsible for the forward and backward flux. All species in the network are considered, but only species that have net flux above a threshold are shown in the diagram.

BIBLIOGRAPHY

R. J. Adrian, R. T. D. S. Ferreira, and T. Boberg. Turbulent thermal convection in wide horizontal fluid layers. *Experiments in Fluids*, 4:121–141, 1986. doi: 10.1007/BF00280263.

M. Agúndez, V. Parmentier, O. Venot, F. Hersant, and F. Selsis. Pseudo 2D chemical model of hot-Jupiter atmospheres: application to HD 209458b and HD 189733b. A&A, 564:A73, April 2014. doi: 10.1051/0004-6361/201322895.

M. Ali-Dib, O. Mousis, J.-M. Petit, and J. I. Lunine. Carbon-rich Planet Formation in a Solar Composition Disk. ApJ, 785:125, April 2014. doi: 10.1088/0004-637X/785/2/125.

Jorg M Anderlohr, Antonio Pires da Cruz, Roda Bounaceur, and Frédérique Battin-Leclerc. Thermal and kinetic impact of co, co2, and h2o on the post-oxidation of ic-engine exhaust gases. *Combustion Science and Technology*, 182 (1):39–59, 2010.

M. Asplund, N. Grevesse, A. J. Sauval, and P. Scott. The Chemical Composition of the Sun. ARA&A, 47:481–522, September 2009. doi: 10.1146/annurev.astro.46.060407.145222.

D. H. Atkinson, T. R. Spilker, J. I. Lunine, A. A. Simon-Miller, S. K. Atreya, A. Colaprete, A. Coustenis, K. R. Reh, and L. J. Spilker. Science from a Saturn Entry Probe Mission. *AGU Fall Meeting Abstracts*, page C1960, December 2012.

F. Bagenal, T. E. Dowling, and W. B. McKinnon. *Jupiter : the planet, satellites and magnetosphere*. 2004.

Frédérique Battin-Leclerc, Roda Bounaceur, N Belmekki, and PA Glaude. Experimental and modeling study of the oxidation of xylenes. *International Journal of Chemical Kinetics*, 38(4):284–302, 2006.

R. Beer. Detection of carbon monoxide in Jupiter. ApJ, 200:L167–L169, September 1975. doi: 10.1086/181923.

C. Beichman, B. Benneke, H. Knutson, R. Smith, P.-O. Lagage, C. Dressing, D. Latham, J. Lunine, S. Birkmann, P. Ferruit, G. Giardino, E. Kempton, S. Carey, J. Krick, P. D. Deroo, A. Mandell, M. E. Ressler, A. Shporer, M. Swain, G. Vasisht, G. Ricker, J. Bouwman, I. Crossfield, T. Greene, S. Howell, J. Christiansen, D. Ciardi, M. Clampin, M. Greenhouse, A. Sozzetti, P. Goudfrooij, D. Hines, T. Keyes, J. Lee, P. McCullough, M. Robberto, J. Stansberry, J. Valenti, M. Rieke, G. Rieke, J. Fortney, J. Bean, L. Kreidberg, D. Ehrenreich, D. Deming, L. Albert, R. Doyon, and D. Sing. Observations of Transiting Exoplanets with the James Webb Space Telescope (JWST). PASP, 126:1134–1173, December 2014. doi: 10.1086/679566.

B. Bézard, P. Drossart, E. Lellouch, G. Tarrago, and J. P. Maillard. Detection of arsine in Saturn. ApJ, 346:509–513, November 1989. doi: 10.1086/168032.

B. Bézard, E. Lellouch, D. Strobel, J.-P. Maillard, and P. Drossart. Carbon Monoxide on Jupiter: Evidence for Both Internal and External Sources. Icarus, 159: 95–111, September 2002. doi: 10.1006/icar.2002.6917.

G. L. Bjoraker, H. P. Larson, and V. G. Kunde. The gas composition of Jupiter derived from 5 micron airborne spectroscopic observations. Icarus, 66:579–609, June 1986. doi: 10.1016/0019-1035(86)90093-X.

Space Studies Board, National Research Council, et al. *Vision and voyages for planetary science in the decade 2013-2022*. National Academies Press, 2012.

BM Boubnov and GS Golitsyn. Experimental study of convective structures in rotating fluids. *Journal of Fluid Mechanics*, 167:503–531, 1986.

BM Boubnov and GS Golitsyn. Temperature and velocity field regimes of convective motions in a rotating plane fluid layer. *Journal of Fluid Mechanics*, 219: 215–239, 1990.

Roda Bounaceur, Pierre-Alexandre Glaude, René Fournet, Frédérique Battin-Leclerc, S Jay, and A Cruz. Kinetic modelling of a surrogate diesel fuel applied to 3d auto-ignition in hcci engines. *International journal of vehicle design*, 44(1-2):124–142, 2007.

Roda Bounaceur, Oliver Herbinet, Rene Fournet, Pierre-Alexandre Glaude, Frederique Battin-Leclerc, Antonio Pires da Cruz, Mohammed Yahyaoui, Karine Truffin, and Gladys Moreac. Modeling the laminar flame speed of natural gas and gasoline surrogates. Technical report, SAE Technical Paper, 2010.

F. H. Briggs and P. D. Sackett. Radio observations of Saturn as a probe of its atmosphere and cloud structure. Icarus, 80:77–103, July 1989. doi: 10.1016/0019-1035(89)90162-0.

Alexander Burcat and Branko Ruscic. *Third millenium ideal gas and condensed phase thermochemical database for combustion with updates from active thermochemical tables*. Argonne National Laboratory Argonne, IL, 2005.

A. S. Burrows. Spectra as windows into exoplanet atmospheres. *Proceedings*

of the National Academy of Science, 111:12601–12609, September 2014. doi: 10.1073/pnas.1304208111.

T. Cavalié, F. Billebaud, M. Dobrijevic, T. Fouchet, E. Lellouch, T. Encrenaz, J. Brillet, G. H. Moriarty-Schieven, J. G. A. Wouterloot, and P. Hartogh. First observation of CO at 345 GHz in the atmosphere of Saturn with the JCMT: New constraints on its origin. Icarus, 203:531–540, October 2009. doi: 10.1016/j.icarus.2009.05.024.

T. Cavalié, P. Hartogh, F. Billebaud, M. Dobrijevic, T. Fouchet, E. Lellouch, T. Encrenaz, J. Brillet, and G. H. Moriarty-Schieven. A cometary origin for CO in the stratosphere of Saturn? A&A, 510:A88, February 2010. doi: 10.1051/0004-6361/200912909.

T. Cavalié, R. Moreno, E. Lellouch, P. Hartogh, O. Venot, G. S. Orton, C. Jarchow, T. Encrenaz, F. Selsis, F. Hersant, and L. N. Fletcher. The first submillimeter observation of CO in the stratosphere of Uranus. A&A, 562:A33, February 2014. doi: 10.1051/0004-6361/201322297.

D. Charbonneau, T. M. Brown, R. W. Noyes, and R. L. Gilliland. Detection of an Extrasolar Planet Atmosphere. ApJ, 568:377–384, March 2002. doi: 10.1086/338770.

MW Chase. Nistjanaf thermochemical tables (journal of physical and chemical reference data monograph no. 9), 1998.

MW Chase, CA Davies, JR Downey, DJ Frurip, RA McDonald, and AN Syverud. Janaf thermochemical tables-2. *Journal of Physical and Chemical Reference Data*, 14:927–1856, 1985.

M. J. Coates and G. N. Ivey. On convective turbulence and the influence of rotation. *Dynamics of Atmospheres and Oceans*, 25:217–232, May 1997. doi: 10.1016/S0377-0265(96)00479-4.

E Coda Zabetta and M Hupa. A detailed kinetic mechanism with methanol for simulating biomass combustion and n-pollutants. *Combustion and Flame*, 152 (1-2):14–27, 2008.

B. J. Conrath and D. Gautier. Saturn Helium Abundance: A Reanalysis of Voyager Measurements. Icarus, 144:124–134, March 2000. doi: 10.1006/icar.1999.6265.

N. Crouzet, P. R. McCullough, D. Deming, and N. Madhusudhan. Water Vapor in the Spectrum of the Extrasolar Planet HD 189733b. II. The Eclipse. ApJ, 795:166, November 2014. doi: 10.1088/0004-637X/795/2/166.

A. Cui and R. L. Street. Large-eddy simulation of turbulent rotating convective flow development. *Journal of Fluid Mechanics*, 447:53–84, November 2001. doi: 10.1017/S0022112001006073.

T. de Graauw, H. Feuchtgruber, B. Bezard, P. Drossart, T. Encrenaz, D. A. Beintema, M. Griffin, A. Heras, M. Kessler, K. Leech, E. Lellouch, P. Morris, P. R. Roelfsema, M. Roos-Serote, A. Salama, B. Vandenbussche, E. A. Valentijn, G. R. Davis, and D. A. Naylor. First results of ISO-SWS observations of Saturn: detection of CO_2_, CH_3_C_2_H, C_4_H_2_ and tropospheric H_2_O. A&A, 321:L13–L16, May 1997.

I. de Pater and S. T. Massie. Models of the millimeter-centimeter spectra of the giant planets. Icarus, 62:143–171, April 1985. doi: 10.1016/0019-1035(85)90177-0.

Anthony M. Dean and Joseph W. Bozzelli. *Gas-Phase Combustion Chemistry*. Springer New York, New York, NY, 2000. ISBN 978-1-4612-1310-9. URL http://dx.doi.org/10.1007/978-1-4612-1310-9_2.

James W Deardorff. Numerical investigation of neutral and unstable planetary boundary layers. *Journal of the Atmospheric Sciences*, 29(1):91–115, 1972.

D. Deming, A. Wilkins, P. McCullough, A. Burrows, J. J. Fortney, E. Agol, I. Dobbs-Dixon, N. Madhusudhan, N. Crouzet, J.-M. Desert, R. L. Gilliland, K. Haynes, H. A. Knutson, M. Line, Z. Magic, A. M. Mandell, S. Ranjan, D. Charbonneau, M. Clampin, S. Seager, and A. P. Showman. Infrared Transmission Spectroscopy of the Exoplanets HD 209458b and XO-1b Using the Wide Field Camera-3 on the Hubble Space Telescope. ApJ, 774:95, September 2013. doi: 10.1088/0004-637X/774/2/95.

A Dollet and S de Persis. Pressure-dependent rate coefficients of chemical reactions involving si 2 h 4 isomerization from qrrk calculations. *Journal of Analytical and Applied Pyrolysis*, 80(2):460–470, 2007.

T. Encrenaz, T. de Graauw, S. Schaeidt, E. Lellouch, H. Feuchtgruber, D. A. Beintema, B. Bezard, P. Drossart, M. Griffin, A. Heras, M. Kessler, K. Leech, P. Morris, P. R. Roelfsema, M. Roos-Serote, A. Salama, B. Vandenbussche, E. A. Valentijn, G. R. Davis, and D. A. Naylor. First results of ISO-SWS observations of Jupiter. A&A, 315:L397–L400, November 1996.

T. M. Evans, D. K. Sing, H. R. Wakeford, N. Nikolov, G. E. Ballester, B. Drummond, T. Kataria, N. P. Gibson, D. S. Amundsen, and J. Spake. Detection of H_2O and Evidence for TiO/VO in an Ultra-hot Exoplanet Atmosphere. ApJ, 822:L4, May 2016. doi: 10.3847/2041-8205/822/1/L4.

B. Fegley and R. G. Prinn. Chemical constraints on the water and total oxygen abundances in the deep atmosphere of Jupiter. ApJ, 324:621–625, January 1988. doi: 10.1086/165922.

B. Fegley, Jr. and K. Lodders. Chemical models of the deep atmospheres of Jupiter and Saturn. Icarus, 110:117–154, July 1994. doi: 10.1006/icar.1994.1111.

B. Fegley, Jr. and R. G. Prinn. Equilibrium and nonequilibrium chemistry of Saturn's atmosphere - Implications for the observability of PH3, N2, CO, and GeH4. ApJ, 299:1067–1078, December 1985. doi: 10.1086/163775.

H. J. S. Fernando, R.-R. Chen, and D. L. Boyer. Effects of rotation on convective turbulence. *Journal of Fluid Mechanics*, 228:513–547, July 1991.

HJS Fernando and DC Smith Iv. Vortex structures in geophysical convection. *European Journal of Mechanics-B/Fluids*, 20(4):437–470, 2001.

U. Fink, H. P. Larson, and R. R. Treffers. Germane in the atmosphere of Jupiter. Icarus, 34:344–354, May 1978. doi: 10.1016/0019-1035(78)90172-0.

F. M. Flasar and P. J. Gierasch. Turbulent convection within rapidly rotating superadiabatic fluids with horizontal temperature gradients. *Geophysical and Astrophysical Fluid Dynamics*, 10:175–212, 1978. doi: 10.1080/03091927808242636.

F. M. Flasar, R. K. Achterberg, B. J. Conrath, J. C. Pearl, G. L. Bjoraker, D. E. Jennings, P. N. Romani, A. A. Simon-Miller, V. G. Kunde, C. A. Nixon, B. Bézard, G. S. Orton, L. J. Spilker, J. R. Spencer, P. G. J. Irwin, N. A. Teanby, T. C. Owen, J. Brasunas, M. E. Segura, R. C. Carlson, A. Mamoutkine, P. J. Gierasch, P. J. Schinder, M. R. Showalter, C. Ferrari, A. Barucci, R. Courtin, A. Coustenis, T. Fouchet, D. Gautier, E. Lellouch, A. Marten, R. Prangé, D. F. Strobel, S. B.

Calcutt, P. L. Read, F. W. Taylor, N. Bowles, R. E. Samuelson, M. M. Abbas, F. Raulin, P. Ade, S. Edgington, S. Pilorz, B. Wallis, and E. H. Wishnow. Temperatures, Winds, and Composition in the Saturnian System. *Science*, 307: 1247–1251, February 2005. doi: 10.1126/science.1105806.

FM Flasar and PETER J Gierasch. Eddy diffusivities within jupiter. In *Planetary Atmospheres*, pages 85–87, 1977.

L. N. Fletcher, G. S. Orton, N. A. Teanby, and P. G. J. Irwin. Phosphine on Jupiter and Saturn from Cassini/CIRS. Icarus, 202:543–564, August 2009a. doi: 10.1016/j.icarus.2009.03.023.

L. N. Fletcher, G. S. Orton, N. A. Teanby, P. G. J. Irwin, and G. L. Bjoraker. Methane and its isotopologues on Saturn from Cassini/CIRS observations. Icarus, 199:351–367, February 2009b. doi: 10.1016/j.icarus.2008.09.019.

L. N. Fletcher, K. H. Baines, T. W. Momary, A. P. Showman, P. G. J. Irwin, G. S. Orton, M. Roos-Serote, and C. Merlet. Saturn's tropospheric composition and clouds from Cassini/VIMS 4.6-5.1 μm nightside spectroscopy. Icarus, 214: 510–533, August 2011. doi: 10.1016/j.icarus.2011.06.006.

L. N. Fletcher, B. Swinyard, C. Salji, E. Polehampton, T. Fulton, S. Sidher, E. Lellouch, R. Moreno, G. Orton, T. Cavalié, R. Courtin, M. Rengel, H. Sagawa, G. R. Davis, P. Hartogh, D. Naylor, H. Walker, and T. Lim. Sub-millimetre spectroscopy of Saturn's trace gases from Herschel/SPIRE. A&A, 539:A44, March 2012. doi: 10.1051/0004-6361/201118415.

M. French, A. Becker, W. Lorenzen, N. Nettelmann, M. Bethkenhagen, J. Wicht, and R. Redmer. Ab Initio Simulations for Material Properties along the Jupiter Adiabat. ApJS, 202:5, September 2012. doi: 10.1088/0067-0049/202/1/5.

N. P. Gibson, F. Pont, and S. Aigrain. A new look at NICMOS transmission spectroscopy of HD 189733, GJ-436 and XO-1: no conclusive evidence for molecular features. MNRAS, 411:2199–2213, March 2011. doi: 10.1111/j.1365-2966.2010.17837.x.

R. S. Giles, L. N. Fletcher, and P. G. J. Irwin. Latitudinal variability in Jupiter's tropospheric disequilibrium species: GeH_4, AsH_3 and PH_3. Icarus, 289:254–269, June 2017. doi: 10.1016/j.icarus.2016.10.023.

G. R. Gladstone, M. Allen, and Y. L. Yung. Hydrocarbon Photochemistry in the Upper Atmosphere of Jupiter. Icarus, 119:1–52, January 1996. doi: 10.1006/icar.1996.0001.

David G. Goodwin, Harry K. Moffat, and Raymond L. Speth. Cantera: An object-oriented software toolkit for chemical kinetics, thermodynamics, and transport processes. `http://www.cantera.org`, 2015. Version 2.2.0.

Sanford Gordon and Bonnie J McBride. Computer program for calculation of chemical equilibrium compositions and applications: I analysis. *NASA RP-1311*, 1994.

D. Grassi, A. Adriani, M. L. Moriconi, N. I. Ignatiev, E. D'Aversa, F. Colosimo, A. Negrão, L. Brower, B. M. Dinelli, A. Coradini, and G. Piccioni. Jupiter's hot spots: Quantitative assessment of the retrieval capabilities of future IR spectro-imagers. Planet. Space Sci., 58:1265–1278, August 2010. doi: 10.1016/j.pss.2010.05.003.

T. P. Greene, M. R. Line, C. Montero, J. J. Fortney, J. Lustig-Yaeger, and K. Luther. Characterizing Transiting Exoplanet Atmospheres with JWST. ApJ, 817:17, January 2016. doi: 10.3847/0004-637X/817/1/17.

T. Guillot and R. Hueso. The composition of Jupiter: sign of a (relatively) late formation in a chemically evolved protosolar disc. MNRAS, 367:L47–L51, March 2006. doi: 10.1111/j.1745-3933.2006.00137.x.

Lev Veniaminovich Gurvich and I Veyts. *Thermodynamic Properties of Individual Substances: Elements and Compounds*, volume 2. CRC press, 1990.

CRC Handbook. Crc handbook of chemistry and physics 2012-2013, 2012.

R. Hanel, B. Conrath, L. Herath, V. Kunde, and J. Pirraglia. Albedo, internal heat, and energy balance of Jupiter - Preliminary results of the Voyager infrared investigation. J. Geophys. Res., 86:8705–8712, September 1981. doi: 10.1029/JA086iA10p08705.

R. A. Hanel, B. J. Conrath, V. G. Kunde, J. C. Pearl, and J. A. Pirraglia. Albedo, internal heat flux, and energy balance of Saturn. Icarus, 53:262–285, February 1983. doi: 10.1016/0019-1035(83)90147-1.

C. J. Hansen, J. C. Schwartz, and N. B. Cowan. Features in the broad-band eclipse spectra of exoplanets: signal or noise? MNRAS, 444:3632–3640, November 2014. doi: 10.1093/mnras/stu1699.

S. B. Hartley and J. C. McCoubrey. Enthalpy of Formation of Phosphorus Oxide. Nature, 198:476, May 1963. doi: 10.1038/198476a0.

Ravit Helled and Jonathan Lunine. Measuring jupiter's water abundance by juno: the link between interior and formation models. *Monthly Notices of the Royal Astronomical Society*, 441(3):2273–2279, 2014.

Yoshiaki Hidaka, Takashi Oki, Hiroyuki Kawano, and Tetsuo Higashihara. Thermal decomposition of methanol in shock waves. *The Journal of Physical Chemistry*, 93(20):7134–7139, 1989. doi: 10.1021/j100357a022.

Renyu Hu and Sara Seager. Photochemistry in terrestrial exoplanet atmospheres. iii. photochemistry and thermochemistry in thick atmospheres on super earths and mini neptunes. *The Astrophysical Journal*, 784(1):63–87, 2014.

W. B. Hubbard, J. J. Fortney, J. I. Lunine, A. Burrows, D. Sudarsky, and P. Pinto. Theory of Extrasolar Giant Planet Transits. ApJ, 560:413–419, October 2001. doi: 10.1086/322490.

C. M. Huitson, D. K. Sing, F. Pont, J. J. Fortney, A. S. Burrows, P. A. Wilson, G. E. Ballester, N. Nikolov, N. P. Gibson, D. Deming, S. Aigrain, T. M. Evans, G. W. Henry, A. Lecavelier des Etangs, A. P. Showman, A. Vidal-Madjar, and K. Zahnle. An HST optical-to-near-IR transmission spectrum of the hot Jupiter WASP-19b: detection of atmospheric water and likely absence of TiO. MNRAS, 434:3252–3274, October 2013. doi: 10.1093/mnras/stt1243.

P. G. J. Irwin, A. L. Weir, S. E. Smith, F. W. Taylor, A. L. Lambert, S. B. Calcutt, P. J. Cameron-Smith, R. W. Carlson, K. Baines, G. S. Orton, P. Drossart, T. Encrenaz, and M. Roos-Serote. Cloud structure and atmospheric composition of Jupiter retrieved from Galileo near-infrared mapping spectrometer real-time spectra. J. Geophys. Res., 103:23001–23022, September 1998. doi: 10.1029/98JE00948.

P. G. J. Irwin, P. Parrish, T. Fouchet, S. B. Calcutt, F. W. Taylor, A. A. Simon-Miller, and C. A. Nixon. Retrievals of jovian tropospheric phosphine from Cassini/CIRS. Icarus, 172:37–49, November 2004. doi: 10.1016/j.icarus.2003.09.027.

M. A. Janssen, M. D. Hofstadter, S. Gulkis, A. P. Ingersoll, M. Allison, S. J. Bolton, S. M. Levin, and L. W. Kamp. Microwave remote sensing of Jupiter's atmo-

sphere from an orbiting spacecraft. Icarus, 173:447–453, February 2005. doi: 10.1016/j.icarus.2004.08.012.

Ahren W Jasper, Stephen J Klippenstein, Lawrence B Harding, and Branko Ruscic. Kinetics of the reaction of methyl radical with hydroxyl radical and methanol decomposition. *The Journal of Physical Chemistry A*, 111(19):3932–3950, 2007.

A. G. Jensen, S. Redfield, M. Endl, W. D. Cochran, L. Koesterke, and T. S. Barman. A Survey of Alkali Line Absorption in Exoplanetary Atmospheres. ApJ, 743:203, December 2011. doi: 10.1088/0004-637X/743/2/203.

Helen Jones and John Marshall. Convection with rotation in a neutral ocean: A study of open-ocean deep convection. *Journal of Physical Oceanography*, 23(6): 1009–1039, 1993.

Lisa Kaltenegger and Wesley A Traub. Transits of earth-like planets. *The Astrophysical Journal*, 698(1):519, 2009.

S. Kendrew, S. Scheithauer, P. Bouchet, J. Amiaux, R. Azzollini, J. Bouwman, C. H. Chen, D. Dubreuil, S. Fischer, A. Glasse, T. P. Greene, P.-O. Lagage, F. Lahuis, S. Ronayette, D. Wright, and G. S. Wright. The Mid-Infrared Instrument for the James Webb Space Telescope, IV: The Low-Resolution Spectrometer. PASP, 127:623–632, July 2015. doi: 10.1086/682255.

William E Koerner and Farrington Daniels. The heat of formation of nitric oxide and phosphorus trioxide. *The Journal of Chemical Physics*, 20(1):113–115, 1952.

R. k. Kopparapu, J. F. Kasting, and K. J. Zahnle. A Photochemical Model for the Carbon-rich Planet WASP-12b. ApJ, 745:77, January 2012. doi: 10.1088/0004-637X/745/1/77.

L. Kreidberg, J. L. Bean, J.-M. Désert, B. Benneke, D. Deming, K. B. Stevenson, S. Seager, Z. Berta-Thompson, A. Seifahrt, and D. Homeier. Clouds in the atmosphere of the super-Earth exoplanet GJ1214b. Nature, 505:69–72, January 2014a. doi: 10.1038/nature12888.

L. Kreidberg, J. L. Bean, J.-M. Désert, M. R. Line, J. J. Fortney, N. Madhusudhan, K. B. Stevenson, A. P. Showman, D. Charbonneau, P. R. McCullough, S. Seager, A. Burrows, G. W. Henry, M. Williamson, T. Kataria, and D. Homeier. A Precise Water Abundance Measurement for the Hot Jupiter WASP-43b. ApJ, 793:L27, October 2014b. doi: 10.1088/2041-8205/793/2/L27.

L. Kreidberg, M. R. Line, J. L. Bean, K. B. Stevenson, J.-M. Désert, N. Madhusudhan, J. J. Fortney, J. K. Barstow, G. W. Henry, M. H. Williamson, and A. P. Showman. A Detection of Water in the Transmission Spectrum of the Hot Jupiter WASP-12b and Implications for Its Atmospheric Composition. ApJ, 814:66, November 2015. doi: 10.1088/0004-637X/814/1/66.

V. Kunde, R. Hanel, W. Maguire, D. Gautier, J. P. Baluteau, A. Marten, A. Chedin, N. Husson, and N. Scott. The tropospheric gas composition of Jupiter's north equatorial belt /NH3, PH3, CH3D, GeH4, H2O/ and the Jovian D/H isotopic ratio. ApJ, 263:443–467, December 1982. doi: 10.1086/160516.

H. P. Larson, U. Fink, and R. C. Treffers. Evidence for CO in Jupiter's atmosphere from airborne spectroscopic observations at 5 microns. ApJ, 219:1084–1092, February 1978. doi: 10.1086/155873.

H. P. Larson, U. Fink, H. A. Smith, and D. S. Davis. The middle-infrared spectrum of Saturn - Evidence for phosphine and upper limits to other trace atmospheric constituents. ApJ, 240:327–337, August 1980. doi: 10.1086/158236.

J. Leconte and G. Chabrier. A new vision of giant planet interiors: Impact of double diffusive convection. A&A, 540:A20, April 2012. doi: 10.1051/0004-6361/201117595.

E. Lellouch, G. Paubert, R. Moreno, M. C. Festou, B. Bézard, D. Bockelée-Morvan, P. Colom, J. Crovisier, T. Encrenaz, D. Gautier, A. Marten, D. Despois, D. F. Strobel, and A. Sievers. Chemical and thermal response of Jupiter's atmosphere following the impact of comet Shoemaker-Levy 9. Nature, 373: 592–595, February 1995. doi: 10.1038/373592a0.

MA Levy and HJS Fernando. Turbulent thermal convection in a rotating stratified fluid. *Journal of Fluid Mechanics*, 467:19–40, 2002.

Juan Li, Zhenwei Zhao, Andrei Kazakov, Marcos Chaos, Frederick L Dryer, and James J Scire. A comprehensive kinetic mechanism for co, ch2o, and ch3oh combustion. *International Journal of Chemical Kinetics*, 39(3):109–136, 2007.

G. F. Lindal, D. N. Sweetnam, and V. R. Eshleman. The atmosphere of Saturn - an analysis of the Voyager radio occultation measurements. AJ, 90:1136–1146, June 1985. doi: 10.1086/113820.

M. R. Line, H. Knutson, A. S. Wolf, and Y. L. Yung. A Systematic Retrieval Analysis of Secondary Eclipse Spectra. II. A Uniform Analysis of Nine Planets and their C to O Ratios. ApJ, 783:70, March 2014. doi: 10.1088/0004-637X/783/2/70.

M. R. Line, K. B. Stevenson, J. Bean, J.-M. Desert, J. J. Fortney, L. Kreidberg, N. Madhusudhan, A. P. Showman, and H. Diamond-Lowe. No Thermal Inversion and a Solar Water Abundance for the Hot Jupiter HD 209458b

from HST/WFC3 Spectroscopy. AJ, 152:203, December 2016. doi: 10.3847/0004-6256/152/6/203.

K. Lodders and B. Fegley. Atmospheric Chemistry in Giant Planets, Brown Dwarfs, and Low-Mass Dwarf Stars. I. Carbon, Nitrogen, and Oxygen. Icarus, 155:393–424, February 2002. doi: 10.1006/icar.2001.6740.

P. R. Mahaffy, H. B. Niemann, A. Alpert, S. K. Atreya, J. Demick, T. M. Donahue, D. N. Harpold, and T. C. Owen. Noble gas abundance and isotope ratios in the atmosphere of Jupiter from the Galileo Probe Mass Spectrometer. J. Geophys. Res., 105:15061–15072, June 2000. doi: 10.1029/1999JE001224.

A. M. Mandell, K. Haynes, E. Sinukoff, N. Madhusudhan, A. Burrows, and D. Deming. Exoplanet Transit Spectroscopy Using WFC3: WASP-12 b, WASP-17 b, and WASP-19 b. ApJ, 779:128, December 2013. doi: 10.1088/0004-637X/779/2/128.

T. Maxworthy and S. Narimousa. Unsteady, Turbulent Convection into a Homogeneous, Rotating Fluid,with Oceanographic Applications. *Journal of Physical Oceanography*, 24:865–887, May 1994. doi: 10.1175/1520-0485(1994)024⟨0865:UTCIAH⟩2.0.CO;2.

B. J. McBride, S. Gordon, and M. A. Reno. Coefficients for calculating thermodynamic and transport properties of individual species. Technical report, October 1993.

Bonnie J McBride and Sanford Gordon. Computer program for calculation of chemical equilibrium compositions and applications: Users manual and program description. *NASA RP-1311*, 1996.

P. R. McCullough, N. Crouzet, D. Deming, and N. Madhusudhan. Water Vapor in the Spectrum of the Extrasolar Planet HD 189733b. I. The Transit. ApJ, 791: 55, August 2014. doi: 10.1088/0004-637X/791/1/55.

Wayne K Metcalfe, Sinéad M Burke, Syed S Ahmed, and Henry J Curran. A hierarchical and comparative kinetic modeling study of c1- c2 hydrocarbon and oxygenated fuels. *International Journal of Chemical Kinetics*, 45(10):638–675, 2013.

Y. Miguel and L. Kaltenegger. Exploring Atmospheres of Hot Mini-Neptunes and Extrasolar Giant Planets Orbiting Different Stars with Application to HD 97658b, WASP-12b, CoRoT-2b, XO-1b, and HD 189733b. ApJ, 780:166, January 2014. doi: 10.1088/0004-637X/780/2/166.

TA Miller, MS Wooldridge, and JW Bozzelli. Computational modeling of the sih 3+ o 2 reaction and silane combustion. *Combustion and flame*, 137(1):73–92, 2004.

Nelson H Morgon. Enthalpies of formation of phosphorus and oxygen compounds determined by the correlation consistent composite approach. *International Journal of Quantum Chemistry*, 112(19):3256–3260, 2012.

J. I. Moses, M. Allen, and G. R. Gladstone. Nitrogen and oxygen photochemistry following SL9. Geophys. Res. Lett., 22:1601–1604, 1995a. doi: 10.1029/95GL01199.

J. I. Moses, M. Allen, and G. R. Gladstone. Post-SL9 sulfur photochemistry on Jupiter. Geophys. Res. Lett., 22:1597–1600, 1995b. doi: 10.1029/95GL01200.

J. I. Moses, B. Bézard, E. Lellouch, G. R. Gladstone, H. Feuchtgruber, and M. Allen. Photochemistry of Saturn's Atmosphere. I. Hydrocarbon Chem-

istry and Comparisons with ISO Observations. Icarus, 143:244–298, February 2000a. doi: 10.1006/icar.1999.6270.

J. I. Moses, E. Lellouch, B. Bézard, G. R. Gladstone, H. Feuchtgruber, and M. Allen. Photochemistry of Saturn's Atmosphere. II. Effects of an Influx of External Oxygen. Icarus, 145:166–202, May 2000b. doi: 10.1006/icar.1999.6320.

J. I. Moses, C. Visscher, T. C. Keane, and A. Sperier. On the abundance of non-cometary HCN on Jupiter. *Faraday Discussions*, 147:103–136, 2010. doi: 10.1039/c003954c.

J. I. Moses, C. Visscher, J. J. Fortney, A. P. Showman, N. K. Lewis, C. A. Griffith, S. J. Klippenstein, M. Shabram, A. J. Friedson, M. S. Marley, and R. S. Freedman. Disequilibrium Carbon, Oxygen, and Nitrogen Chemistry in the Atmospheres of HD 189733b and HD 209458b. ApJ, 737:15, August 2011. doi: 10.1088/0004-637X/737/1/15.

J. I. Moses, N. Madhusudhan, C. Visscher, and R. S. Freedman. Chemical Consequences of the C/O Ratio on Hot Jupiters: Examples from WASP-12b, CoRoT-2b, XO-1b, and HD 189733b. ApJ, 763:25, January 2013. doi: 10.1088/0004-637X/763/1/25.

Julianne I. Moses. Chemical kinetics on extrasolar planets. *Philosophical Transactions of the Royal Society of London A: Mathematical, Physical and Engineering Sciences*, 372(2014), 2014. ISSN 1364-503X. doi: 10.1098/rsta.2013.0073. URL `http://rsta.royalsocietypublishing.org/content/372/2014/20130073`.

O. Mousis, U. Marboeuf, J. I. Lunine, Y. Alibert, L. N. Fletcher, G. S. Orton,

F. Pauzat, and Y. Ellinger. Determination of the Minimum Masses of Heavy Elements in the Envelopes of Jupiter and Saturn. ApJ, 696:1348–1354, May 2009. doi: 10.1088/0004-637X/696/2/1348.

O. Mousis, J. I. Lunine, N. Madhusudhan, and T. V. Johnson. Nebular Water Depletion as the Cause of Jupiter's Low Oxygen Abundance. ApJ, 751:L7, May 2012. doi: 10.1088/2041-8205/751/1/L7.

O. Mousis, L. N. Fletcher, J.-P. Lebreton, P. Wurz, T. Cavalié, A. Coustenis, R. Courtin, D. Gautier, R. Helled, P. G. J. Irwin, A. D. Morse, N. Nettelmann, B. Marty, P. Rousselot, O. Venot, D. H. Atkinson, J. H. Waite, K. R. Reh, A. A. Simon, S. Atreya, N. André, M. Blanc, I. A. Daglis, G. Fischer, W. D. Geppert, T. Guillot, M. M. Hedman, R. Hueso, E. Lellouch, J. I. Lunine, C. D. Murray, J. O'Donoghue, M. Rengel, A. Sánchez-Lavega, F.-X. Schmider, A. Spiga, T. Spilker, J.-M. Petit, M. S. Tiscareno, M. Ali-Dib, K. Altwegg, S. J. Bolton, A. Bouquet, C. Briois, T. Fouchet, S. Guerlet, T. Kostiuk, D. Lebleu, R. Moreno, G. S. Orton, and J. Poncy. Scientific rationale for Saturn's in situ exploration. Planet. Space Sci., 104:29–47, December 2014. doi: 10.1016/j.pss.2014.09.014.

O. Mousis, D.H. Atkinson, T. Spilker, E. Venkatapathy, J. Poncy, R. Frampton, A. Coustenis, K. Reh, J.-P. Lebreton, L.N. Fletcher, R. Hueso, M.J. Amato, A. Colaprete, F. Ferri, D. Stam, P. Wurz, S. Atreya, S. Aslam, D.J. Banfield, S. Calcutt, G. Fischer, A. Holland, C. Keller, E. Kessler, M. Leese, P. Levacher, A. Morse, O. Muoz, J.-B. Renard, S. Sheridan, F.-X. Schmider, F. Snik, J.H. Waite, M. Bird, T. Cavali, M. Deleuil, J. Fortney, D. Gautier, T. Guillot, J.I. Lunine, B. Marty, C. Nixon, G.S. Orton, and A. Snchez-Lavega. The hera saturn entry probe mission. *Planetary and Space Science*, pages –, 2015. ISSN 0032-0633. doi: http://dx.doi.org/10.1016/j.pss.2015.06.

020. URL http://www.sciencedirect.com/science/article/pii/S0032063315001981. in press.

DW Muenow, OM Uy, and JL Margrave. Mass spectrometric studies of the vaporization of phosphorus oxides. *Journal of Inorganic and Nuclear Chemistry*, 32(11):3459–3467, 1970.

H. B. Niemann, S. K. Atreya, G. R. Carignan, T. M. Donahue, J. A. Haberman, D. N. Harpold, R. E. Hartle, D. M. Hunten, W. T. Kasprzak, P. R. Mahaffy, T. C. Owen, and S. H. Way. The composition of the Jovian atmosphere as determined by the Galileo probe mass spectrometer. J. Geophys. Res., 103: 22831–22846, September 1998. doi: 10.1029/98JE01050.

N. Nikolov, D. K. Sing, F. Pont, A. S. Burrows, J. J. Fortney, G. E. Ballester, T. M. Evans, C. M. Huitson, H. R. Wakeford, P. A. Wilson, S. Aigrain, D. Deming, N. P. Gibson, G. W. Henry, H. Knutson, A. Lecavelier des Etangs, A. P. Showman, A. Vidal-Madjar, and K. Zahnle. Hubble Space Telescope hot Jupiter transmission spectral survey: a detection of Na and strong optical absorption in HAT-P-1b. MNRAS, 437:46–66, January 2014. doi: 10.1093/mnras/stt1859.

K. S. Noll and H. P. Larson. The spectrum of Saturn from 1990 to 2230/cm - Abundances of AsH3, CH3D, CO, GeH4, NH3, and PH3. Icarus, 89:168–189, January 1991. doi: 10.1016/0019-1035(91)90096-C.

K. S. Noll, R. F. Knacke, T. R. Geballe, and A. T. Tokunaga. Detection of carbon monoxide in Saturn. ApJ, 309:L91–L94, October 1986. doi: 10.1086/184768.

K. S. Noll, R. F. Knacke, T. R. Geballe, and A. T. Tokunaga. Evidence for germane in Saturn. Icarus, 75:409–422, September 1988. doi: 10.1016/0019-1035(88)90154-6.

K. S. Noll, T. R. Geballe, and R. F. Knacke. Arsine in Saturn and Jupiter. ApJ, 338:L71–L74, March 1989. doi: 10.1086/185404.

K. S. Noll, H. P. Larson, and T. R. Geballe. The abundance of AsH3 in Jupiter. Icarus, 83:494–499, February 1990. doi: 10.1016/0019-1035(90)90080-S.

V. Parmentier and T. Guillot. A non-grey analytical model for irradiated atmospheres. I. Derivation. A&A, 562:A133, February 2014. doi: 10.1051/0004-6361/201322342.

V. Parmentier, A. P. Showman, and Y. Lian. 3D mixing in hot Jupiters atmospheres. I. Application to the day/night cold trap in HD 209458b. A&A, 558: A91, October 2013. doi: 10.1051/0004-6361/201321132.

V. Parmentier, T. Guillot, J. J. Fortney, and M. S. Marley. A non-grey analytical model for irradiated atmospheres. II. Analytical vs. numerical solutions. A&A, 574:A35, February 2015. doi: 10.1051/0004-6361/201323127.

F. Pont, H. Knutson, R. L. Gilliland, C. Moutou, and D. Charbonneau. Detection of atmospheric haze on an extrasolar planet: the 0.55-1.05 μm transmission spectrum of HD 189733b with the HubbleSpaceTelescope. MNRAS, 385:109–118, March 2008. doi: 10.1111/j.1365-2966.2008.12852.x.

M. J. Prather, J. A. Logan, and M. B. McElroy. Carbon monoxide in Jupiter's upper atmosphere - an extraplanetary source. ApJ, 223:1072–1081, August 1978. doi: 10.1086/156340.

R. G. Prinn and S. S. Barshay. Carbon monoxide on Jupiter and implications for atmospheric convection. *Science*, 198:1031–1034, December 1977. doi: 10.1126/science.198.4321.1031.

R. G. Prinn, H. P. Larson, J. J. Caldwell, and D. Gautier. *Composition and chemistry of Saturn's atmosphere*, pages 88–149. 1984.

S. Redfield, M. Endl, W. D. Cochran, and L. Koesterke. Sodium Absorption from the Exoplanetary Atmosphere of HD 189733b Detected in the Optical Transmission Spectrum. ApJ, 673:L87, January 2008. doi: 10.1086/527475.

S. T. Ridgway, L. Wallace, and G. R. Smith. The 800-1200 inverse centimeter absorption spectrum of Jupiter. ApJ, 207:1002–1006, August 1976. doi: 10.1086/154570.

Edward R Ritter. Therm: A computer code for estimating thermodynamic properties for species important to combustion and reaction modeling. *Journal of chemical information and computer sciences*, 31(3):400–408, 1991.

Laurence S Rothman, Iouli E Gordon, Yury Babikov, Alain Barbe, D Chris Benner, Peter F Bernath, Manfred Birk, Luca Bizzocchi, Vincent Boudon, Linda R Brown, et al. The hitran2012 molecular spectroscopic database. *Journal of Quantitative Spectroscopy and Radiative Transfer*, 130:4–50, 2013.

LS Rothman, IE Gordon, RJ Barber, H Dothe, RR Gamache, A Goldman, VI Perevalov, SA Tashkun, and J Tennyson. Hitemp, the high-temperature molecular spectroscopic database. *Journal of Quantitative Spectroscopy and Radiative Transfer*, 111(15):2139–2150, 2010.

S. Seager and D. D. Sasselov. Theoretical Transmission Spectra during Extrasolar Giant Planet Transits. ApJ, 537:916–921, July 2000. doi: 10.1086/309088.

A. Seiff, D. B. Kirk, T. C. D. Knight, R. E. Young, J. D. Mihalov, L. A. Young, F. S. Milos, G. Schubert, R. C. Blanchard, and D. Atkinson. Thermal structure of Jupiter's atmosphere near the edge of a 5-μm hot spot in the north

equatorial belt. J. Geophys. Res., 103:22857–22890, September 1998. doi: 10.1029/98JE01766.

A. P. Showman, Y. Kaspi, and G. R. Flierl. Scaling laws for convection and jet speeds in the giant planets. Icarus, 211:1258–1273, February 2011. doi: 10.1016/j.icarus.2010.11.004.

D. K. Sing, C. M. Huitson, M. Lopez-Morales, F. Pont, J.-M. Désert, D. Ehrenreich, P. A. Wilson, G. E. Ballester, J. J. Fortney, A. Lecavelier des Etangs, and A. Vidal-Madjar. GTC OSIRIS transiting exoplanet atmospheric survey: detection of sodium in XO-2b from differential long-slit spectroscopy. MNRAS, 426:1663–1670, October 2012. doi: 10.1111/j.1365-2966.2012.21938.x.

D. K. Sing, H. R. Wakeford, A. P. Showman, N. Nikolov, J. J. Fortney, A. S. Burrows, G. E. Ballester, D. Deming, S. Aigrain, J.-M. Désert, N. P. Gibson, G. W. Henry, H. Knutson, A. Lecavelier des Etangs, F. Pont, A. Vidal-Madjar, M. W. Williamson, and P. A. Wilson. HST hot-Jupiter transmission spectral survey: detection of potassium in WASP-31b along with a cloud deck and Rayleigh scattering. MNRAS, 446:2428–2443, January 2015. doi: 10.1093/mnras/stu2279.

M. D. Smith. Estimation of a Length Scale to Use with the Quench Level Approximation for Obtaining Chemical Abundances. Icarus, 132:176–184, March 1998. doi: 10.1006/icar.1997.5886.

S Smoes and J Drowart. Atomization energies of phosphorus oxides. In *Faraday Symposia of the Chemical Society*, volume 8, pages 139–148. Royal Society of Chemistry, 1973.

D. J. Stevenson. Turbulent thermal convection in the presence of rotation and a

magnetic field - A heuristic theory. *Geophysical and Astrophysical Fluid Dynamics*, 12:139–169, 1979. doi: 10.1080/03091927908242681.

D. J. Stevenson and J. I. Lunine. Rapid formation of Jupiter by diffuse redistribution of water vapor in the solar nebula. Icarus, 75:146–155, July 1988. doi: 10.1016/0019-1035(88)90133-9.

P. H. Stone. The meteorology of the Jovian atmosphere. In *Jupiter*, pages 586–618, 1976.

D. F. Strobel. The Galilean satellites as a source of CO in the Jovian upper atmosphere. Icarus, 37:256–263, January 1979. doi: 10.1016/0019-1035(79)90130-1.

C.J. Sung, C.K. Law, and J.-Y. Chen. An augmented reduced mechanism for methane oxidation with comprehensive global parametric validation. *Symposium (International) on Combustion*, 27(1):295 – 304, 1998. ISSN 0082-0784. doi: http://dx.doi.org/10.1016/S0082-0784(98)80416-5. Twenty-Seventh Sysposium (International) on Combustion Volume One.

Max Tirtowidjojo and Richard Pollard. Equilibrium gas phase species for mocvd of alxga 1- x as. *Journal of Crystal Growth*, 77(1):200–209, 1986.

WA Traub and K Jucks. Atmospheres in the solar system: Comparative aeronomy, ed. *M. Mendillo, A. Nagy, & JH Waite (Geophysical Monograph 130*, 2002.

Wesley A Traub and Mark T Stier. Theoretical atmospheric transmission in the mid-and far-infrared at four altitudes. *Applied Optics*, 15(2):364–377, 1976.

Richard R Treffers, Harold P Larson, Uwe Fink, and Thomas N Gautier. Upper limits to trace constituents in jupiter's atmosphere from an analysis of its 5-μm spectrum. *Icarus*, 34(2):331–343, 1978.

Allen Twarowski. The influence of phosphorus oxides and acids on the rate of h+ oh recombination. *Combustion and flame*, 94(1):91–107, 1993.

Allen Twarowski. Reduction of a phosphorus oxide and acid reaction set. *Combustion and flame*, 102(1):41–54, 1995.

Allen Twarowski. The temperature dependence of h+ oh recombination in phosphorus oxide containing post-combustion gases. *Combustion and flame*, 105(3): 407–413, 1996.

O. Venot, E. Hébrard, M. Agúndez, M. Dobrijevic, F. Selsis, F. Hersant, N. Iro, and R. Bounaceur. A chemical model for the atmosphere of hot Jupiters. A&A, 546:A43, October 2012. doi: 10.1051/0004-6361/201219310.

Olivia Venot. Photochimie des exoplanètes chaudes: modélisations et expériences. *PhD Thesis, status: published*, 2012.

C. Visscher and B. Fegley, Jr. Chemical Constraints on the Water and Total Oxygen Abundances in the Deep Atmosphere of Saturn. ApJ, 623:1221–1227, April 2005. doi: 10.1086/428493.

C. Visscher and J. I. Moses. Quenching of Carbon Monoxide and Methane in the Atmospheres of Cool Brown Dwarfs and Hot Jupiters. ApJ, 738:72, September 2011. doi: 10.1088/0004-637X/738/1/72.

C. Visscher, K. Lodders, and B. Fegley, Jr. Atmospheric Chemistry in Giant Planets, Brown Dwarfs, and Low-Mass Dwarf Stars. II. Sulfur and Phosphorus. ApJ, 648:1181–1195, September 2006. doi: 10.1086/506245.

C. Visscher, J. I. Moses, and S. A. Saslow. The deep water abundance on Jupiter: New constraints from thermochemical kinetics and diffusion modeling. Icarus, 209:602–615, October 2010. doi: 10.1016/j.icarus.2010.03.029.

H. R. Wakeford, D. K. Sing, D. Deming, N. P. Gibson, J. J. Fortney, A. S. Burrows, G. Ballester, N. Nikolov, S. Aigrain, G. Henry, H. Knutson, A. Lecavelier des Etangs, F. Pont, A. P. Showman, A. Vidal-Madjar, and K. Zahnle. HST hot Jupiter transmission spectral survey: detection of water in HAT-P-1b from WFC3 near-IR spatial scan observations. MNRAS, 435:3481–3493, November 2013. doi: 10.1093/mnras/stt1536.

H. R. Wakeford, D. K. Sing, T. Kataria, D. Deming, N. Nikolov, E. Lopez, P. Tremblin, D. Skalid Amundsen, N. K. Lewis, A. Mandell, J. J. Fortney, H. Knutson, B. Benneke, and T. M. Evans. HAT-P-26b: A Neptune-mass Exoplanet with Primordial Solar Heavy Element Abundance. In *American Astronomical Society Meeting Abstracts*, volume 229 of *American Astronomical Society Meeting Abstracts*, page 401.01, January 2017.

V. Wakelam, E. Herbst, J.-C. Loison, I. W. M. Smith, V. Chandrasekaran, B. Pavone, N. G. Adams, M.-C. Bacchus-Montabonel, A. Bergeat, K. Béroff, V. M. Bierbaum, M. Chabot, A. Dalgarno, E. F. van Dishoeck, A. Faure, W. D. Geppert, D. Gerlich, D. Galli, E. Hébrard, F. Hersant, K. M. Hickson, P. Honvault, S. J. Klippenstein, S. Le Picard, G. Nyman, P. Pernot, S. Schlemmer, F. Selsis, I. R. Sims, D. Talbi, J. Tennyson, J. Troe, R. Wester, and L. Wiesenfeld. A Kinetic Database for Astrochemistry (KIDA). ApJS, 199:21, March 2012. doi: 10.1088/0067-0049/199/1/21.

D. Wang, P. J. Gierasch, J. I. Lunine, and O. Mousis. New insights on Jupiter's deep water abundance from disequilibrium species. Icarus, 250:154–164, April 2015. doi: 10.1016/j.icarus.2014.11.026.

D. Wang, J. I. Lunine, and O. Mousis. Modeling the disequilibrium species for

Jupiter and Saturn: Implications for Juno and Saturn entry probe. Icarus, 276: 21–38, September 2016. doi: 10.1016/j.icarus.2016.04.027.

Haowei Wang, Steven J Warner, Matthew A Oehlschlaeger, Roda Bounaceur, Joffrey Biet, Pierre-Alexandre Glaude, and Frédérique Battin-Leclerc. An experimental and kinetic modeling study of the autoignition of α-methylnaphthalene/air and α-methylnaphthalene/n-decane/air mixtures at elevated pressures. *Combustion and Flame*, 157(10):1976–1988, 2010.

P. A. Wilson, D. K. Sing, N. Nikolov, A. Lecavelier des Etangs, F. Pont, J. J. Fortney, G. E. Ballester, M. López-Morales, J.-M. Désert, and A. Vidal-Madjar. GTC OSIRIS transiting exoplanet atmospheric survey: detection of potassium in HAT-P-1b from narrow-band spectrophotometry. MNRAS, 450:192–200, June 2015. doi: 10.1093/mnras/stv642.

M. H. Wong, P. R. Mahaffy, S. K. Atreya, H. B. Niemann, and T. C. Owen. Updated Galileo probe mass spectrometer measurements of carbon, oxygen, nitrogen, and sulfur on Jupiter. Icarus, 171:153–170, September 2004. doi: 10.1016/j.icarus.2004.04.010.

Y. L. Yung, W. A. Drew, J. P. Pinto, and R. R. Friedl. Estimation of the reaction rate for the formation of CH3O from H + H2CO - Implications for chemistry in the solar system. Icarus, 73:516–526, March 1988. doi: 10.1016/0019-1035(88)90061-9.

Michael R Zachariah and Wing Tsang. Theoretical calculation of thermochemistry, energetics, and kinetics of high-temperature sixhyoz reactions. *The Journal of Physical Chemistry*, 99(15):5308–5318, 1995.

K. Zahnle, M. S. Marley, R. S. Freedman, K. Lodders, and J. J. Fortney. Atmo-

spheric Sulfur Photochemistry on Hot Jupiters. ApJ, 701:L20–L24, August 2009. doi: 10.1088/0004-637X/701/1/L20.

Kevin J Zahnle and Mark S Marley. Methane, carbon monoxide, and ammonia in brown dwarfs and self-luminous giant planets. *The Astrophysical Journal*, 797(1):41–59, 2014.